Seasonal variability of Atlantic Water recirculation in Fram Strait from observations

Zerlina Hofmann
1010110

First supervisor: Prof. Dr. Peter Brandt
Second supervisor: Dr. Wilken-Jon von Appen

A thesis presented for the degree of Master of Science in
Climate Physics: Meteorology and Physical Oceanography

Faculty of Mathematics and Natural Sciences
Christian-Albrechts-Universität zu Kiel, Germany

February 24, 2020

Abstract

This account of the first direct long-term observations of the Atlantic Water recirculation in Fram Strait gives new insight to both the recirculation's location and variability. While Fram Strait is largely influenced by the inflow of warm, saline water from the Atlantic Ocean and the outflow of cold, fresh water and sea ice from the Arctic Ocean, part of the Atlantic Water inflow recirculates, i.e. turns westward in Fram Strait already. This affects both the amount of heat that is transported to the Arctic Ocean, as well as the properties of water that ultimately contributes to deep water formation in the Nordic Seas, an important aspect of the overturning circulation of the world's oceans.

We investigate the Atlantic Water recirculation with regard to its location and variability by analysing observations from an array of five moorings. The moorings were placed at an equal distance of 40' of latitude between 78°10'N and 80°50'N along the prime meridian, and were in the water from August 2016 to July 2018, where they measured temperature, salinity, and velocity in the upper 800 m of the water column.

We can confirm the existence of two recirculation branches with distinct properties north (in the vicinity of 80°10'N) and south (in the vicinity of 78°50'N) of the Molloy Hole, and observe no recirculation at the northernmost mooring (80°50'N).

The southern recirculation branch is present throughout the year, as indicated by strong westward velocities, and relatively high temperatures and salinities (that is, higher than further north and south). It displays stronger velocities during the first half of the year with a maximum in May and a strong additional northward component in March to May. At times, it affects the mooring locations further south and north, indicating some meandering or broadening/narrowing of the flow.

The northern recirculation branch is much stronger in winter and nearly absent in summer, as indicated by a strong temperature and salinity maximum in December to February, and a minimum in June to August. While southward velocities suggest the corresponding mooring to be located in the Arctic Ocean outflow, the variability of the velocities is high, and eddy kinetic energy is maximal in November, and January/February. This highlights the importance of eddies for the northern recirculation branch. It may affect the mooring location further south by blocking southward transport of Polar Water at the prime meridian during its presence, and instead promoting the southward transport of Atlantic Water.

New insights on the two recirculation branches carrying Atlantic Water constrain the dynamics that take place in Fram Strait. This knowledge can improve conceptual as well as numerical models of how the role of Fram Strait as a connection between the Nordic Seas and the Arctic Ocean, and its part in the overturning circulation will evolve in the future.

Zusammenfassung

Dieser Bericht der ersten direkten Langzeit-Messungen der Rezirkulation atlantischen Wassers in der Framstraße gibt neue Einblicke bezüglich der Lage und Variabilität der Rezirkulation. Die Framstraße ist vornehmlich durch den Zustrom warmen, salzigen Wassers aus dem Atlantischen Ozean und den Ausstrom kalten, süßen Wassers vom Arktischen Ozean beeinflusst. Bereits in der Framstraße rezirkuliert jedoch ein Teil des Atlantischen Wassers, das heißt er biegt Richtung Westen in die zentrale Framstraße ab. Das hat Einfluss sowohl auf den Umfang der Wärme, die in Richtung des Arktischen Ozeans transportiert wird, als auch auf die Eigenschaften des Wassers, das letztlich zur Tiefenwasserformation der Nordmeere beiträgt und zu einem Teil der Umwälzzirkulation der Weltmeere wird.
Wir untersuchen die Rezirkulation Atlantischen Wassers bezüglich seiner Lage und Variabilität, indem wir Beobachtungen von einer Verankerungsreihe analysieren. Die Verankerungsreihe besteht aus fünf Verankerungen, die in gleicher Entfernung von 40' Breite zwischen 78°10'N und 80°50'N entlang des Nullmeridian platziert wurden. Sie waren von August 2016 bis Juli 2018 im Wasser und maßen Temperatur, Salzgehalt und Strömungsgeschwindigkeit in den oberen 800 m der Wassersäule.
Wir können bestätigen, dass zwei Rezirkulationspfade mit ausgeprägten Eigenschaften nördlich (in der Nähe von 80°10'N) und südlich (in der Nähe von 78°50'N) des Molloytiefs existieren. An der nördlichsten Verankerung (80°50'N) beobachten wir keine Rezirkulation.
Der südliche Rezirkulationspfad ist das ganze Jahr vorhanden, gekennzeichnet durch starke westwärtige Geschwindigkeiten und hohe Temperatur und Salzgehalt (im Vergleich zu weiter nördlich oder südlich). Die westwärtigen Geschwindigkeiten sind stärker während der ersten Hälfte des Jahres, mit einem Maximum im Mai und zusätzlich einer starken nordwärtigen Strömungskomponente im März bis Mai. Bisweilen beeinflusst der südliche Rezirkulationspfad die Verankerungen weiter südlich oder nördlich, was auf Mäandern oder eine Ausdehnung/Verengung der Strömung hindeuten könnte.
Der nördliche Rezirkulationspfad ist deutlich stärker im Winter und ist beinahe abwesend im Sommer, worauf ein klares Temperatur- und Salzgehaltsmaximum im Dezember bis Februar und ein Minimum im Juni bis August hindeutet. Die südwärtigen Geschwindigkeiten an der zugehörigen Verankerung deuten zwar darauf hin, dass die Verankerung sich im Ausstrom des Arktischen Ozeans befindet, aber die Variabilität der Geschwindigkeiten ist hoch, und die kinetische Energie von Ozeanwirbeln ist maximal im November und Januar/Februar. Das hebt die Bedeutung von diesen Ozeanwirbeln für den nördlichen Rezirkulationspfad hervor. Er beeinflusst möglicherweise die Gegend weiter südlich, indem er den südwärtigen Transport von Polarem Wasser blockiert und stattdessen den südwärtigen Transport von Atlantischem Wasser fördert.

Neuen Erkenntnisse zu den beiden Rezirkulationspfaden, die Atlantisches Wasser transportieren, engen unser Verständnis zur Dynamik in der Framstraße weiter ein. Dieses Wissen kann einen Beitrag zur Verbesserung von konzeptuellen sowie numerischen Modellen leisten, im Bezug darauf wie sich die Framstraße als Verbindung zwischen den Nordmeeren und dem Arktischen Ozean, sowie als Anteil an der Umwälzzirkulation, in Zukunft entwickeln wird.

Contents

List of Figures

List of Tables

Chapter 1

Introduction

The Arctic Ocean is mostly surrounded by landmass, though exchange of water and sea ice is possible through a few pathways, namely the Fram Strait, the Barents Sea Opening, the Bering Strait, and various small channels in the Canadian Arctic Archipelago. The Fram Strait is the only deep connection (∼2500 m) between the Arctic Ocean and the Nordic Seas. Warm, saline water from the Atlantic Ocean enters via the West Spitsbergen Current (WSC) on the eastern side of the strait, while cold, fresher water and sea ice (as well as modified, previously warm and saline water) from the Arctic Ocean exits via the East Greenland Current (EGC) on the western side. The circulation in the Fram Strait is strongly defined by these boundary currents importing and exporting water to and from the Arctic Ocean. Part of the Atlantic Water (AW), however, recirculates (i.e. turns westward) in the Fram Strait before ever reaching the Arctic Ocean. This westward flow component, the recirculation of AW in Fram Strait, will be the focus of this thesis. In the following, we will introduce the general setting of the Nordics Seas and Fram Strait in particular (Chapter 1.1), summarise the research status on the AW recirculation (Chapter 1.2), highlight its importance on a larger scale (Chapter 1.3), and formulate the research questions that will be answered in this thesis (Chapter 1.4).

1.1 Fram Strait and the surrounding seas

The so-called Arctic Mediterranean includes both the Nordic Seas and the Arctic Ocean and their adjacent shelf areas, with the two being connected via Fram Strait and the Barents Sea (Figure 1.1). The Fram Strait is the ocean passage between Greenland and the Svalbard archipelago, located roughly at 76–82°N and centred on the prime meridian. The Barents Sea is a marginal sea of the Arctic Ocean, located off the northern coasts of Scandinavia and Russia, and fairly shallow (∼230 m). The Nordic Seas comprise the Greenland Sea, the Norwegian Sea, and the Iceland Sea (Figure 1.1) and are bounded to the south by the Greenland-Scotland-Ridge, which spans from Greenland over Iceland and the Faroe Islands to Shetland (Scotland). On average, it is only 500 m deep, with some parts reaching a depth of 850 m. The Fram Strait is thus of particular importance in its role as the deep connection between the Arctic Ocean and the Nordic Seas.

The deep part of the strait horizontally spans about 300 km, bordered by the broad continental shelves of Greenland (∼300 km) and Svalbard (∼50 km). The topography in the centre of the strait is thus characterised by continental slopes in the east

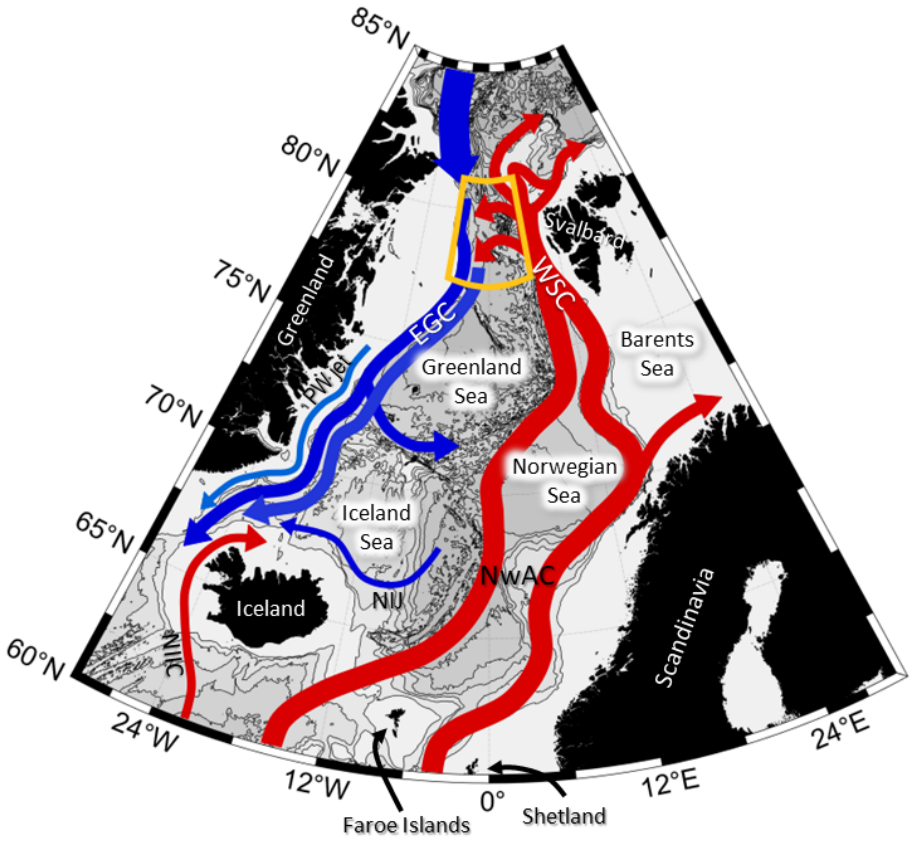

Figure 1.1: Schematic circulation of the Nordic Seas with inflow from the Atlantic Ocean in red and outflow from the Arctic Ocean in blue. Different shadings of blue indicate different amounts of mixing between warm, saline AW and cold, fresh PW. The yellow box marks the study area. Abbreviations are as follows: NwAC = Norwegian Atlantic Current, WSC = West Spitsbergen Current, EGC = East Greenland Current, NIIC = North Iceland Irminger Current, NIJ = North Icelandic Jet.

and west, as well as some complex topography in between. The latter largely takes shape as the Knipovich Ridge, the northernmost section of the Mid-Atlantic Ridge that connects with the Gakkel Ridge in the Arctic Ocean (Figure 1.2).
The so-called Yermak Plateau is a plateau of about 700 m depth that is located northwest of Svalbard. The average water depth in the deep part of the strait is about 2500 m, though the deepest part is a bathymetric feature called the Molloy Hole, more than twice as deep (5555 m, Figure 1.2). Two fracture zones enclose this area, the Spitsbergen Fracture Zone in the north and the Molloy Fracture Zone in the south. Parallel to the Molloy Fracture Zone further south, the Hovgaard Ridge and the East Greenland Ridge enclose the Boreas Abyssal Plain, a wider plain of about 2500 m depth. Between 71 to 75°N the Mohns Ridge and Knipovich Ridge split the Nordic Seas into the Greenland Abyssal Plain and the Lofoten Basin (Hansen and Østerhus, 2000).
In the next subchapters, an introduction is given on the warm, saline inflow to, and the cold, fresh outflow from the Arctic Ocean and its path through the Nordic Seas (Chapters 1.1.1 and 1.1.2, respectively). Water masses that are transported to or formed in the Nordic Seas and the Arctic Ocean are explained in detail in Chapter 1.1.3.

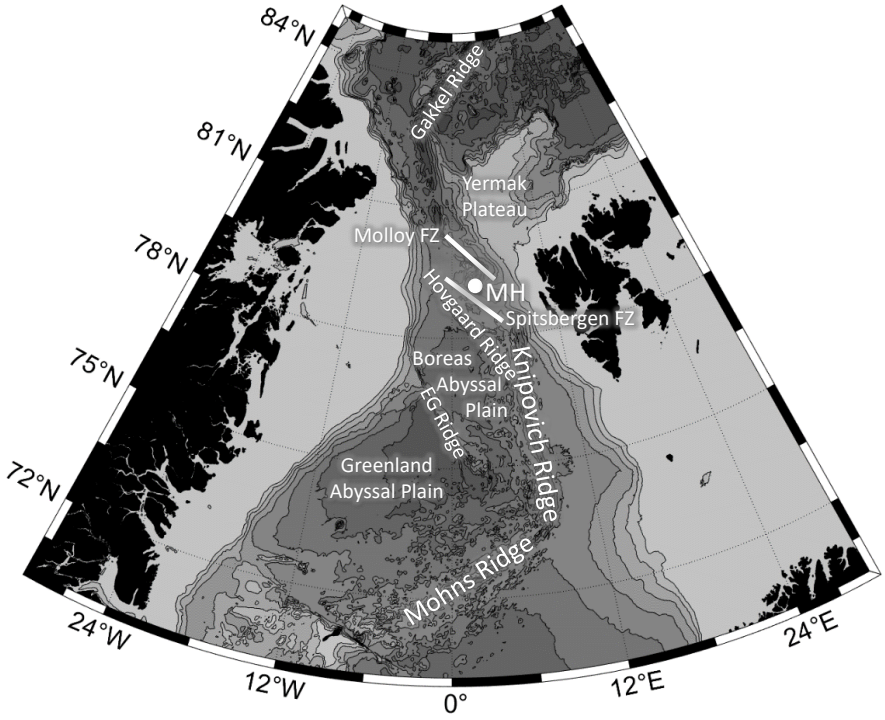

Figure 1.2: Map of Fram Strait with bathymetry from Schaffer et al. (2019) and bathymetrical feature names from the IHO-IOC GEBCO Gazetteer of Undersea Feature Names (https://www.gebco.net). The white lines mark fracture zones, the white dot the Molloy Hole. Abbreviations are as follows: MH = Molloy Hole, FZ = Fracture Zone, EG = East Greenland.

1.1.1 Inflow

Warm, saline AW enters the Nordic Seas between Greenland and Scotland, originating from two source regions. One is the area, where the North Atlantic Current enters the eastern Atlantic, feeding the inflow branches between Greenland and Iceland (the North Icelandic Irminger Current, NIIC), and between Iceland and the Faroe Islands (Hansen and Østerhus, 2000). The other is located south of the Greenland-Scotland inflow region just off the European shelf, feeding a current passing through the Faroe-Shetland Channel (Hansen and Østerhus, 2000). The inflow between Iceland and the Faroe Islands is the western branch, the inflow through the Faroe-Shetland Channel the eastern branch of the Norwegian Atlantic Current (NwAC, Figure 1.1). Both are topographically steered through the Nordic Seas along the Mohns and Knipovich Ridge, and the Norwegian shelf edge, respectively. The eastern branch bifurcates north of Norway, with part of the current continuing into the Barents Sea (Orvik and Niiler, 2002). Both branches of the NwAC ultimately converge in the region west of central Spitsbergen as the WSC, with the shortest distance between the two branches being at 77°N due to bottom topography (Walczowski et al., 2005). In the northern Fram Strait the flow splits again (Figure 1.1). It partly turns westward and recirculates, joining the EGC on its southward path, as described in much more detail in Chapter 1.2. The remainder of the flow splits into one branch following the coastline, cutting across the Yermak Plateau, and the other following the shelf break of the plateau (Perkin and Lewis, 1984; Quadfasel

et al., 1987; Walczowski et al., 2005). The two branches have been termed the Svalbard Branch and the Yermak Branch, respectively (Manley et al., 1992). The Yermak Branch splits up once more, partly progressing along the continental slope of the Yermak Plateau and partly crossing the Yermak Plateau through the Yermak Pass (Gascard et al., 1995), the latter having been named the Yermak Pass Branch (Koenig et al., 2017b). Model studies suggest the Yermak Pass Branch to have a strong seasonality and to be the dominant route for AW to enter the Arctic Ocean (Koenig et al., 2017a; Crews et al., 2019). While the Svalbard branch appears to be relatively stable throughout the year, in the model study by Crews et al. (2019), the WSC's increased flow during the winter is divided between the recirculation and the Yermak Pass Branch. Owing to their origin from different branches of the NwAC, the Svalbard and Yermak branches have different signatures and different advection timescales from the splitting of the NwAC to the point, where they enter the Arctic Ocean, resulting in different cooling rates of the AW (Beszczynska-Möller et al., 2012). Substantial heat is lost from the Yermak Branch due to strong tidal currents over the Yermak Plateau that lead to increased turbulent mixing (Padman et al., 1992; Fer et al., 2015).

The most obvious characteristics of the WSC are its relatively high temperature and salinity, reflecting its origin far to the south (Hanzlick, 1983). Average northward transport values at 78.5°–79°N range from about 5–12 Sv (Aagaard et al., 1973; Hanzlick, 1983; Fahrbach et al., 2001; Schauer et al., 2004; Walczowski et al., 2005; Beszczynska-Möller et al., 2012). Generally, direct current measurements yield much higher transports than hydrographic measurements and model studies (Walczowski et al., 2005). This is because the WSC has a strong barotropic component, and as a direct consequence, it strongly interacts with bottom topography (Hanzlick, 1983; Gascard et al., 1995). The WSC is barotropically and baroclinically unstable at least sometimes (Teigen et al., 2010, 2011). von Appen et al. (2016) found that the WSC is much more baroclinically unstable and likely to generate eddies during winter than during summer, while barotropic instability plays some role during winter in regions, where the topography supports it. The barotropic nature and the unsteadiness of the WSC, as well as the variable bottom topography in Fram Strait explain why the WSC has such a strong tendency to branch and form eddies along topographic fracture zones (Gascard et al., 1995).

An increase of the year-round mean AW temperature advected from the North Atlantic has been observed from 1997 to 2010 at the zonal array in Fram Strait (Beszczynska-Möller et al., 2012). This has been ongoing at a less steep rate since 2010 (W.-J. von Appen, pers. comm., 2019). In addition von Appen et al. (2015) found that the deep (>1000 m) water masses north and south of Fram Strait are warming, which will likely cause exchange processes at depth within the strait to change. Walczowski et al. (2017) also observed a clear increase in summer AW temperature in the whole layer from the surface down to 1000 m.

1.1.2 Outflow

The Arctic Ocean outflow in Fram Strait north of 80°N has been observed and modelled as a broad barotropic flow between the northeast Greenland shelf and 0° and may at least partly be topographically steered (Richter et al., 2018). Further south the EGC follows the Greenland continental shelf break (Figure 1.1), contains

stronger velocities (Aagaard and Coachman, 1968a; de Steur et al., 2014), and has a stronger baroclinic component (Aagaard and Coachman, 1968b; Gascard et al., 1995; Richter et al., 2018). Foldvik et al. (1988) found about half of the EGC transport at 79°N to be barotropic though, and de Steur et al. (2014) found the EGC to be even more barotropic at 78°50'N compared to 79°N. The study by de Steur et al. (2014) may, however, have been influenced by a warm anomaly present at the time it was conducted. Both de Steur et al. (2014) and Richter et al. (2018) argue that the recirculating AW affects the EGC in its strength and structure. Yearly averaged southward transport values at 78°50'N range from about 4–15 Sv, and at 79°N from about 2–10 Sv (de Steur et al., 2014), though previous yearly averages from the same mooring array at 79°N are larger, between 11–13 Sv (Fahrbach et al., 2001; Schauer et al., 2004), likely due to different data handling methods. In 1994–95 at 75°N a southward transport of 21 Sv was found — part of this transport must be waters that recirculate within the Greenland Sea Gyre, as well as waters that will exit the Greenland Sea further south (Woodgate et al., 1999).
Håvik et al. (2017) found that the EGC has three distinct branches: the shelf break EGC flowing along the shelf break all the way from the Arctic Ocean outflow to the Denmark Strait, a jet carrying PW on the continental shelf south of 74°N, and the outer EGC over the mid- to deep continental slope fed by the recirculation (Figure 1.1). Both the outer EGC and the shelf break EGC flow towards the south side-by-side at least as far south as the Jan Mayen Fracture Zone (Håvik et al., 2017). Here the denser waters are likely deflected towards the east and circulate around the Greenland Sea Gyre (Figure 1.1), potentially penetrating towards the centre and interacting with the Greenland Sea waters (Rudels et al., 1999). The surface outflow of the EGC combined with the overflow across the Greenland-Scotland Ridge comprises the total outflow from the Arctic Mediterranean through the Greenland-Scotland gap (Hansen and Østerhus, 2000). The Iceland Sea may also be a potential contributor to the overflow via the North Icelandic Jet (NIJ, Figure 1.1), which flows along the northern continental slope of Iceland (Våge et al., 2013).

1.1.3 Water masses

Here, water masses are introduced in the context of their origin/formation, quantitative definitions of the water masses relevant to the data analysis in this thesis can be found in Table 2.1.
Water of Atlantic origin entering the Norwegian Sea between Iceland and Scotland, which is carried north by the NwAC, is termed Atlantic Water (AW), a surface water mass associated with a temperature and salinity maximum. Part of the AW enters the Barents Sea, where it loses a lot of heat to the atmosphere and gains salinity in the form of brine as ice forms, so that the water mass rapidly changes its characteristics (Jones, 2001). The remaining AW continues on its northward path with the WSC in Fram Strait, where it continuously loses heat, while freshwater is added, reducing its salinity (Piechura et al., 2001), or it recirculates and has been termed Return Atlantic Water (Mauritzen, 1996), or Recirculating Atlantic Water (Rudels et al., 2002). The amount of heat carried towards the Arctic Ocean that is vertically mixed from the WSC core towards the ice is enough to maintain essentially ice-free conditions west and north of Svalbard to 80°–82°N (Aagaard et al., 1987; Onarheim et al., 2014).

When the AW enters the Arctic Ocean, it is further modified by heat loss at the surface and by mixing with colder waters from the north. Nonetheless, it can still be identified by its relatively high temperature, which decreases both to the east and to the north (Perkin and Lewis, 1984). As one moves into the basin, the rate of reduction of the temperature decreases (Perkin and Lewis, 1984).
Inflow through the Bering Strait is comparatively small, but has been increasing in 2001–2014 from ∼0.7 Sv to ∼1.2 Sv (Woodgate, 2018). The water of Pacific origin that reaches the Arctic Ocean is at times stored in the Beaufort Gyre and eventually drained through the passages of the Canadian Arctic Archipelago for the most part (Falck et al., 2005). Thus, the main water mass in the Arctic Ocean with which the AW can interact, either directly or through the melting and freezing of sea ice, is the fresh Polar Water (PW) added by river runoff, net precipitation, and ice melt — it dilutes the AW and produces low density surface water, which is counteracted by cooling and freezing (Rudels and Quadfasel, 1991). At this point, the AW has been strongly modified and is traditionally referred to as Arctic Intermediate Water, though AIW is defined such that it also includes most of the intermediate water in the Greenland and Iceland Seas as well. For more clarity, the AIW that exclusively stems from the Arctic Ocean has been termed Arctic Atlantic Water (AAW) (Mauritzen, 1996), though sometimes it is also referred to as Modified Atlantic Water (e.g. Rudels and Quadfasel, 1991). In general, the Arctic Ocean can be characterised by a mixed layer consisting of PW at the surface and a cold halocline separating this surface layer from the warm layer of AW (Rudels, 1986). Below resides upper Polar Deep Water (characterised by a negative potential temperature-salinity relationship), which extends to an average depth of the Lomonosov Ridge (∼1700 m, the mid-ocean ridge running from northern Greenland to the Siberian shelf, separating the Arctic Ocean into the Eurasian and Amerasian Basins). Even further down in the water column, deep waters extends to a depth of about 2500 m, and beneath lies bottom water (Jones, 2001). The deep water masses of the Arctic Ocean can mainly be separated by the major basins into Canadian Basin Deep Water and Eurasian Basin Deep Water (Rudels, 1986).
The Arctic Ocean outflow with the EGC contains three major water masses: the cold and fresh PW at the surface with a strong halocline, the AW (depending on the latitude and the EGC branch more recirculated AW or AAW) with a temperature maximum and increasing salinity down to/around this maximum (below salinity is fairly constant), and cold, saline deep water furthest down (Aagaard and Coachman, 1968a). The intermediate and deep waters present in the Nordic Seas originate from the Arctic Ocean, and are mixed with deep waters from the Greenland Sea (i.e. Greenland Sea Deep Water, produced by open ocean deep convection) and the Norwegian Sea (i.e. Norwegian Sea Deep Water, a mixture of Arctic Ocean deep waters and GSDW), as well as intermediate waters from the Iceland Sea (Rudels and Quadfasel, 1991). Early studies mainly considered these deep water masses to contribute to the water that ultimately spills over the Greenland-Scotland-Ridge, either through the Denmark Strait as Denmark Strait Overflow Water or between Iceland, the Faroe Islands, and Shetland as Iceland Scotland Overflow Water (Swift et al., 1980; Rudels and Quadfasel, 1991). However, Mauritzen (1996) found that an alternative circulation scheme might be more likely, in which AW gradually becomes more dense (most prominently in the Norwegian Sea) and is transported by the boundary currents surrounding the Nordic Seas. More recently, the two main

sources of DSOW were found to be the EGC (both the shelf break and outer EGC branches) and the NIJ (Harden et al., 2016). The recirculated AW is thought to travel relatively unperturbed with the EGC along the continental slope of Greenland towards the Denmark Strait, exiting as the deepest water mass of the EGC above sill depth (Mauritzen, 1996; Rudels et al., 2002; Håvik et al., 2017).

1.2 Recirculation in Fram Strait

First hints of a recirculation in Fram Strait were noted by Aagaard and Coachman (1968b), using observational data from 1958 and 1962, which showed a westward movement of warm water from the WSC north of 75°N. Perkin and Lewis (1984) found the indication of strong time-varying currents in the central Fram Strait during CTD measurements in 1981 that suggested some form of mixing between the WSC and the EGC. Since 1997 a mooring array has been deployed from the eastern Greenland shelf break to the western shelf break off Spitsbergen, with its eastern part located at 78°50'N and its western part at 79°N (Fahrbach et al., 2001). In 2002 the western part was moved to 78°50'N in order to line up with the rest of the array (de Steur et al., 2014), and since 2016 the eastern part has been moved to 79°N (von Appen, 2018). In the following, this mooring array will be referred to as 'zonal array'.
Measurements at the latitude of the zonal array also indicate mostly westward flow in the central Fram Strait (Schauer et al., 2004; Beszczynska-Möller et al., 2012). Other observations that have been used for a better understanding of the recirculation include in particular the Marginal Ice Zone Experiment (Johannessen, 1987; Johannessen et al., 1987; Quadfasel et al., 1987; Gascard et al., 1988), and many CTD measurements (e.g. Manley, 1995; Marnela et al., 2013; Richter et al., 2018), yet long-term measurements in the central Fram Strait remain scarce, particularly during winter time. In the north, the ice cover further complicates observations.
In- and outflow through Fram Strait via the boundary currents has been simulated with different model setups (Schlichtholz and Houssais, 1999a,b; Maslowski et al., 2004; Losch et al., 2005; Aksenov et al., 2010; Fieg et al., 2010; Ilicak et al., 2016), and whether the resulting transports compare well to observations largely depends on whether the recirculation of AW in Fram Strait is well represented. More recently, several modelling setups have been utilised to evaluate the recirculation more closely (Kawasaki and Hasumi, 2016; Hattermann et al., 2016; Wekerle et al., 2017; Richter et al., 2018), but the results are still inconclusive about location and strength of individual pathways, the northern limit of the recirculation, and the strength of the boundary currents. One of the main issues is the resolution necessary to resolve eddies that play a large role in Fram Strait (Rudels, 1987; Gascard et al., 1988, 1995; Rudels et al., 2005). The horizontal scale of eddies is governed by the local internal Rossby radius of deformation (Fieg et al., 2010), which is about 2–6 km in the WSC (von Appen et al., 2016) and about 6 km in the EGC (Zhao et al., 2014). Only recent modelling efforts in the Fram Strait can be considered eddy-resolving (Kawasaki and Hasumi, 2016; Hattermann et al., 2016; Wekerle et al., 2017; Richter et al., 2018).
Since the first measurements by Aagaard and Coachman (1968b), a lot of publications (as detailed below) have touched on the subject of AW recirculation in the Fram Strait, but a consensus on location, properties, and strength of this flow does

not yet exist.

1.2.1 Location

In terms of location of the recirculation there have been observations of AW and/or westward motion in the central Fram Strait between 75°N (Bourke et al., 1987) and as far north as 82°N (Gascard et al., 1995). Most of the recirculation appears to occur between 78°N and 80°N, in particular along the Spitsbergen Fracture Zone and south of the Molloy Hole (Quadfasel et al., 1987; Gascard et al., 1988, 1995; Rudels et al., 2005; Richter et al., 2018), as well as along the Molloy Fracture Zone and north of the Molloy Hole (Bourke et al., 1988; Quadfasel et al., 1987; Richter et al., 2018). High-resolution simulations of AW circulation in Fram Strait reveal a similar picture: westward flow occurs both along the Spitsbergen Fracture Zone and along the Molloy Fracture Zone (Schlichtholz and Houssais, 1999a,b; Kawasaki and Hasumi, 2016; Hattermann et al., 2016; Wekerle et al., 2017) and appears to be topographically steered along the Knipovich Ridge (Aksenov et al., 2010; Kawasaki and Hasumi, 2016; Wekerle et al., 2017). The two recirculation branches may even originate from the two different branches of the NwAC (Figure 1.3). Wekerle et al. (2017) additionally found westward flow between 80°30'N and 81°30'N in their model, similar to observations from Gascard et al. (1995).

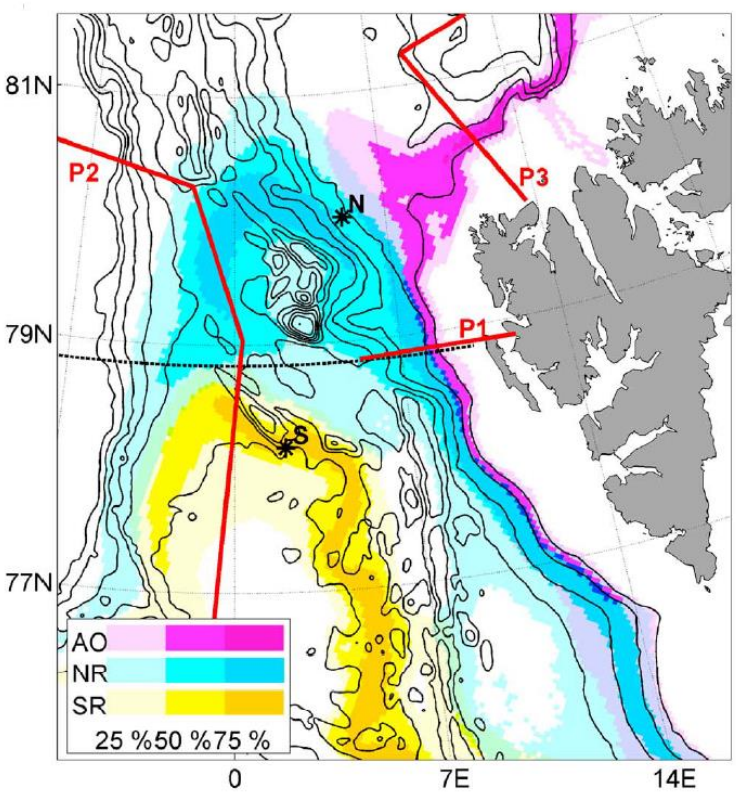

Figure 1.3: Map of the relative trajectory density distribution of floats of the southern recirculation (SR, yellow), northern recirculation (NR, blue), and Arctic Ocean inflow (AO, pink) pathway groups, being defined by the sections P1–P3 and shown as the percentage of all floats within each group. Figure from Hattermann et al. (2016).

The northern boundary of the recirculation remains unclear — Richter et al. (2018)

speculated, whether they observed the northern rim of the recirculation in their synoptic observations as they did not observe any AW at 80°48'N, though their model suggested the northern rim to lie further north. Generally, models with lower resolutions have produced a recirculation that takes place further south than observed (Fieg et al., 2010), though Wekerle et al. (2017) compared two models of different resolution and the low-resolution model only simulated recirculation too far north (between 80°N and 81°30'N). If the recirculation is simulated too far south or north, the boundary current transports in Fram Strait will not be represented correctly, and the central Fram Strait is left with a temperature bias. The process of AW subducting below the PW in the western part of the strait will then also be misrepresented, potentially leading to AW properties along the Greenland continental margin.
Related to the northern extent of the recirculation it is interesting to consider, how large of a contributor the Yermak branch of the WSC is to the recirculating AW. This, again, is far from clear: Aagaard et al. (1987) found that the Yermak Branch does not re-appear on the southeastern flank of the Yermak Plateau, suggesting it is mainly delivered to the Arctic Ocean, while Manley (1995) speculated that most, if not all of the Yermak Branch could be defined as recirculating. More recently, Crews et al. (2019) found that the properties of the WSC are associated with conditions that either promote flow onto the Yermak Plateau (a warmer, faster WSC), or flow deflecting from the continental slope, i.e. recirculation (a colder, slower WSC).
The recirculation, or at least part of it, has also frequently been described as the Return Atlantic Current (RAC), a current that lies along the front between the PW of the EGC and the AW present towards the east (Paquette et al., 1985). It occupies depths roughly between 50 and 400 m (Paquette et al., 1985; Bourke et al., 1987, 1988), is characterised by a subsurface temperature and salinity maximum (Paquette et al., 1985; Quadfasel et al., 1987), and is essentially all AW that has cooled with little or no dilution (Bourke et al., 1987, 1988). It is described as a multi-path current (Gascard et al., 1995) or broken into differing filaments (Paquette et al., 1985), though the wording may suggest the RAC to be a constant stream or current. Hence, the term RAC is used less often in publications that are more recent.

1.2.2 Properties

There has been clear evidence of eddies in the central Fram Strait (Rudels, 1987; Gascard et al., 1995; Rudels et al., 2005; von Appen et al., 2018), which are likely generated along the continental slope off Spitsbergen in the WSC (Gascard et al., 1988, 1995). Instead of a continuous stream, the recirculation may solely exist as westward propagating WSC eddies (Gascard et al., 1988; Rudels et al., 2005), though these may be advected by a background flow (Johannessen et al., 1987). Model studies support the fact that there seems to be an abundance of mesoscale eddies and filaments in the flow within Fram Strait (Hattermann et al., 2016; Kawasaki and Hasumi, 2016). Besides in the WSC, Wekerle et al. (2017) found high values of eddy kinetic energy (EKE) between the northern rim of the Boreas Abyssal Plain and the Molloy Hole, and along the EGC and in the western part of the Boreas Abyssal Plain.
The eddies have been observed to mainly be composed of warm and salty AW (Gascard et al., 1995), but even if the recirculation only takes a short additional

northward excursion, the water loses a considerable amount of heat (Schauer et al., 2004). Simulations suggest that both warm-core anticyclonic eddies and cold-core cyclonic eddies are present in Fram Strait (Wekerle et al., 2017), which are then advected all the way to the EGC (Hattermann et al., 2016). When they reach western Fram Strait, they are potentially subject to mixing with the AAW carried by the EGC (Gascard et al., 1995; Rudels et al., 2005). How much heat the recirculated AW may add to the EGC has been documented by de Steur et al. (2014), when they looked at temperature measurements from the zonal array in Fram Strait, before and after the western part was moved from 79°N to 78°50'N. Temperatures at almost all mooring longitudes in the western part of the Fram Strait were higher at 78°50'N than at 79°. The westward velocity of the eddies was reported as about 0.05 m s^{-1} (Gascard et al., 1988, 1995), while velocities of up to 0.13 m s^{-1} were measured in the RAC (Bourke et al., 1988). The structure of the recirculation in an inverse model study was suggested to be mostly baroclinic south of the Molloy Hole and along the EGC, and mostly barotropic north of the Molloy Hole (Schlichtholz and Houssais, 1999a).

1.2.3 Transport

Transport estimates of the recirculation can be difficult to compare, as they include direct measurements of transports across the Fram Strait, inferred transports from measuring in the boundary currents, measurements that cover only part of the recirculation, or include the transport of other water masses than AW. Early estimates based on geostrophic velocities computed from CTD sections taken in 1980, 1983, and 1988 during summer suggest that about 1 Sv of the northward flow of AW in the WSC recirculates, adding more than one third to the flow in the upper layers of the EGC (Rudels, 1987; Gascard et al., 1995). Bourke et al. (1988) also analysed summer CTD sections (from 1985), but differentiated between recirculation south of 79°N, deduced from a reduction of the WSC of 0.8 Sv, and recirculation between 79°N and 81°N, where a net westward flow of 0.4 Sv was measured. The zonal array in Fram Strait has given some insights into year-round direct current measurements. Fahrbach et al. (2001) estimated a westward recirculation from the two central moorings at 78°50'N and 79°N of 2.6 Sv. Schauer et al. (2004) observed a southward transport of about 0.5 Sv west of the Yermak Plateau branch of the WSC that had a remarkably similar temperature compared to the northward flow, suggesting it took only a short excursion north and recirculated quickly. After the western part of the mooring array was moved to line up with the eastern part, de Steur et al. (2014) found that the recirculation adds about 2.7 Sv to the EGC between 78°50'N and 79°N. Summer meridional sections (from about 78°N to 80°N) have shown geostrophic transports between 0.4 and 2.3 Sv, with no difference between the northern and southern part of the section in two years and opposing transports in one year (Marnela et al., 2013). Implied transports from zonal sections indicated AW recirculation of about 2 Sv in three out of four years and almost no recirculation in the fourth year north of 79°N (Marnela et al., 2013).
In an inverse model study Schlichtholz and Houssais (1999a) found that the recirculation rate, implied from the decrease in WSC transport from south to north and the increase in EGC transport from north to south, amounts to 1.8 Sv on average between 77°36'N and 78°54'N, and 0.5 Sv between 78°54'N and 79°54'N. Further

north the decrease in WSC and increase in EGC were not consistent. Other estimates from simulations are 5.2 Sv, of which 2.7 Sv consist of water warmer than 2°C (Kawasaki and Hasumi, 2016), and 2.4 Sv (Wekerle et al., 2017).

1.2.4 Recirculation percentage

Previous studies mostly agree on the fraction of AW that recirculates, which is considered to be half of the AW entering the Fram Strait (Rudels, 1987; Marnela et al., 2013; de Steur et al., 2014). Manley (1995) estimated that about 20% is recirculated with the RAC, while the Yermak branch is the main contributor to the recirculation further north, which would constitute about half of the AW being recirculated north of 79°N.
Modelling studies find similar values of about half of the AW entering Fram Strait recirculating (Kawasaki and Hasumi, 2016; Wekerle et al., 2017). Schlichtholz and Houssais (1999a) found that about 75% of the WSC inflow recirculates. Hattermann et al. (2016) differentiate between 60% recirculation in late winter/spring and 30% recirculation during summer (when the total AW inflow to Fram Strait is also weaker).

1.2.5 Variability

Particularly the different reports of location and transport of the recirculation in different years suggest some interannual variability, while the importance of eddy activity for the recirculation suggests significant mesoscale variability. Since most measurements in central Fram Strait were conducted during summer, and many are only synoptic, information about seasonal variability can only be deduced from observations of the boundary currents or models. de Steur et al. (2014) found that after the western part of the zonal array in Fram Strait was moved from 79°N to 78°50'N, the southward velocity displayed a clear seasonality, implying that the recirculation contributes the seasonal signal. von Appen et al. (2016) also used observations from the zonal array and found a strong seasonality of EKE in the WSC and the central Fram Strait, with the EKE maximum in the WSC observed during winter, and the EKE maximum in the central Fram Strait observed a little later in April. They suggest that the recirculation likely advects eddies across the Fram Strait during winter, while during summer the amplitudes of EKE are generally much weaker (von Appen et al., 2016). Modelling studies also find the highest values of EKE in the WSC and export of water westwards to be the strongest during winter (Hattermann et al., 2016; Wekerle et al., 2017). Wekerle et al. (2017) did not find all recirculation branches to be present during summer, when the circulation around the Molloy Hole was absent.

1.3 Large scale impact of the recirculation

Subsequently, the large scale impact of the recirculation is described. The recirculation has important implications for the heat transport towards the Arctic Ocean, as it ultimately determines, how much of the warm, saline inflow through Fram Strait actually reaches the Arctic Ocean (Chapter 1.3.1). Recirculating AW hence affects sea ice cover in the Arctic Ocean as well as in Fram Strait, and can even reach the

Greenland shelf and affect the Greenland ice sheet (Chapter 1.3.2). The part of the recirculating AW that joins the EGC on its southward path has an impact on deep water formation (Chapter 1.3.3) and the meridional overturning circulation of the World Ocean (Chapter 1.3.4).

1.3.1 Heat transport towards the Arctic Ocean

While the tropics receive an excess in shortwave radiation, the high latitudes actually lose heat to space and thus some heat needs to be transported poleward in the atmosphere and the ocean for an equilibrium to establish. The largest transport towards the Arctic Ocean occurs in the atmosphere and less than 10% of the heat transport required to balance the heat loss to space is provided by the oceanic heat transport towards the Arctic Ocean (Rudels, 2016). The dominant source for this heat transport is the inflow of AW combined with the export of PW and ice through Fram Strait (Schauer et al., 2004). Both the WSC in Fram Strait and the Barents Sea inflow carry a significant amount of heat, but the Barents Sea inflow loses most of its heat directly to the atmosphere in the southwestern Barents Sea (Smedsrud et al., 2010). The AW in the WSC is able to preserve its warm core, as the upper part of the AW becomes transformed into a fresher surface layer by melting sea ice and mixing with water of Arctic origin (Beszczynska-Möller et al., 2012). The heat carried by the WSC that reaches the Arctic Ocean is then lost mostly within the deep ocean (Rudels, 2016). This is of particular interest, if one considers that the AW transported towards the Arctic Ocean may be increasing in temperature, and perhaps also in volume (Beszczynska-Möller et al., 2012). Recirculating AW in Fram Strait significantly impacts the redistribution of oceanic heat between the Nordic Seas and the Arctic Ocean (Hattermann et al., 2016), ultimately determining how much of the heat carried by the WSC reaches the Arctic Ocean and how much joins the EGC on its southward path.

1.3.2 Sea ice and glacial melt

Diminishing sea ice plays a leading role in Arctic temperature amplification due to the surface albedo feedback (Screen and Simmonds, 2010) — sea ice has a much higher surface albedo than open water, meaning a decrease in sea ice extent causes further surface warming. Sea ice extent in the Arctic from satellite data displays downward linear trends for all months, but with the largest trend for September, when the melt season ends (Serreze and Stroeve, 2015). It is becoming increasingly clear that if greenhouse gas concentrations in the atmosphere continue to rise, the Arctic Ocean will eventually become seasonally ice-free, though it is not quite clear yet as to when this will happen exactly (Stroeve et al., 2012; Notz and Stroeve, 2016). In particular, the decline in sea ice concentration north of Svalbard is associated with the warming of AW entering the Arctic Ocean in this region (Onarheim et al., 2014). Sea ice in the Nansen Basin (which is closest to the Fram Strait of all the basins in the Arctic Ocean) is affected through oceanic heat transport, as the AW is initially in direct contact with the ice and then melts it, with the upper part of the AW being transformed into less dense surface water (Rudels, 2016). The eastern Eurasian Basin may be in transition to similar conditions, as declining sea ice extent and weakening of stratification in the layers over the AW drive enhanced upward heat

fluxes (Polyakov et al., 2017).
Oceanic heat transport can also play a role in glacial melt of the Greenland glaciers. AW that recirculates in Fram Strait is able to cross the Greenland shelf break and enter the trough system (Schaffer et al., 2017), where the bathymetry provides a direct pathway between the shelf break and the marine terminating glaciers of Northeast-Greenland, this being a likely driver of ice sheet retreat and changing glacier dynamics (Schaffer et al., 2020).

1.3.3 Intermediate/deep water formation

The deep waters of the Arctic Ocean, mixed with deep waters from the Norwegian and the Greenland Seas, and intermediate waters from the Iceland Sea, contribute to the overflow across the Greenland-Scotland-Ridge and propagate a saline signal to the deep World Ocean (Rudels and Quadfasel, 1991).
There are two distinct mechanisms for creating deep water in the Arctic Mediterranean, one of which is the open ocean deep convection in the Greenland Sea, where water from surface to near-surface layers sinks to large depths (∼1000 m) due to heat loss to the atmosphere, as the ice cover is only thin or intermittent (Rudels and Quadfasel, 1991; Brakstad et al., 2019). In the Arctic Ocean, net precipitation and runoff from the continents play a role in creating a low salinity surface layer that can prevent deep convection, especially if it becomes cooled enough to form sea ice, isolating the water below from heat loss to the atmosphere (Rudels et al., 2005). Ice formation causes brine release into the water column, which increases the salinity of the shelf bottom water that then ultimately crosses the shelf break and sinks down the continental slope, corresponding to the second mechanism of deep water formation in the Arctic Mediterranean (Rudels and Quadfasel, 1991; Akimova et al., 2011). Both mechanisms require a specific setting in the surface layer related both to temperature and salinity (Hansen and Østerhus, 2000), meaning the properties of the water being advected into the Arctic Ocean and the Greenland Sea (and by association the water recirculating in Fram Strait) are quite relevant to deep water formation. Mauritzen (1996) proposed an additional third mechanism, where AW gradually becomes more dense and is transported by the boundary currents surrounding the Nordic Seas, ultimately also contributing to the overflow waters.
In general, the AW that flows into the Nordic Seas is considered the main source from which overflow waters are produced (Hansen and Østerhus, 2000). The amount of AW that either recirculates or continues on its way into the Arctic Ocean affects all three mechanisms of intermediate and deep water formation. The AW reaching the Arctic Ocean contributes to setting up the halocline, underlying the colder and fresher surface water. A stronger, more stable halocline insulates the ice cover, which in turn affects dense water formation on the shelves (Aagaard et al., 1981). The deep and intermediate waters exiting the Arctic Ocean are transported southward together with the recirculating AW in the EGC, interacting with waters from the Greenland and Iceland Seas (Rudels et al., 2002). In the Greenland Sea, the deep water is constrained by the topography and circulates internally (Aagaard et al., 1985). The (still comparatively warm) Arctic Ocean outflow may act to destabilise the middle and lower water column in the convective region, preconditioning it for deep convection (Aagaard et al., 1991). The intermediate water can cross topography and continue into the deep North Atlantic (Aagaard et al., 1985).

1.3.4 Meridional overturning circulation

How the Atlantic Meridional Overturning Circulation (AMOC) is responding to ongoing changes in the climate system is still up for debate. While many climate models predict a weakening in the future (Cheng et al., 2013), current observations cover only a brief period. The AMOC has been in a state of reduced overturning since 2008, but this may well be part of decadal variability (Smeed et al., 2018). Studies using proxy data have argued for (Rahmstorf et al., 2015; Caesar et al., 2018) a slowdown of the AMOC.
Only recently, Lozier et al. (2019) found that the Nordic Seas play a much more important role in AMOC variability than previously anticipated. As part of the AW recirculation, the subduction of AW below PW in Fram Strait is the northernmost extent of the boundary current loop that part of the AMOC takes in the Nordic Seas.

1.4 Research questions

The present data set of measurements in the upper 800 m of the central Fram Strait over the period of two years is used to describe the recirculation of AW in terms of location and variability. In regard to the available data, we will answer the following questions:

1. Where does the recirculation occur?
2. How variable is the recirculation in terms of location, strength, and properties?

The answers to these questions will not only add to our knowledge of the AW recirculation, but also to its dynamical understanding. In the following we will elaborate on the data and methods used (Chapter 2). We will analyse and discuss seasonal and interannual variability of the southernmost mooring (which we believe to be in the Greenland Sea domain, Chapter 3.2), and of the northernmost mooring (which is located in the Arctic Ocean outflow, Chapter 3.3). The focus of this thesis are the three moorings, with which we were able to observe the two branches of the recirculation, and we analyse and discuss seasonal and interannual, as well as mesoscale variability (Chapters 3.4, 3.5, 3.6). In Chapter 4 we summarise our findings and conclude with an outlook of what could be done in the future.

Chapter 2

Data and Methods

During a cruise with the research vessel Polarstern (campaign PS100) in July/August 2016 five equally spaced moorings with a distance of ∼75 km or 40' of latitude in between them, named R1-1 through R5-1, were deployed along the prime meridian in the Fram Strait (Figure 2.1). They measured temperature, salinity, oxygen, and velocity in the upper 750 m of the water column (Kanzow, 2017). All of those moorings were successfully recovered during a subsequent cruise (campaign PS114) in July/August 2018 (von Appen, 2018).

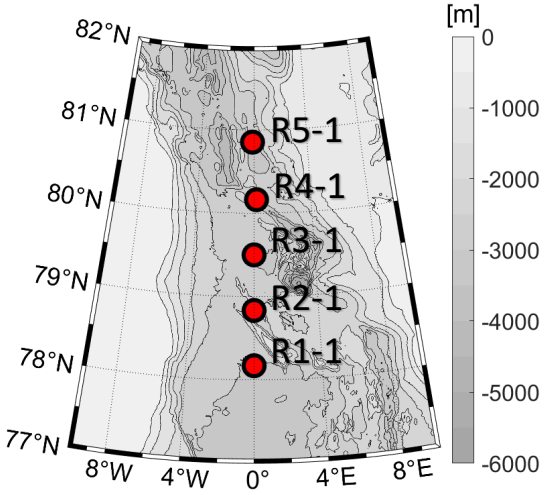

Figure 2.1: Map of central Fram Strait with mooring locations (red dots).

The instruments recovered from the moorings relevant to this work are SeaBird SBE37 CTDs with an oxygen sensor, measuring temperature, conductivity, pressure, and oxygen, SeaBird SBE56 temperature loggers, measuring temperature, RDI 150 kHz Acoustic Doppler Current Profilers (ADCPs), measuring velocity profiles, temperature, and pressure, and NORTEK Aquadopps for deep water, measuring point velocity, and temperature. The location of the instruments in the water column is marked in Figure 2.2. Mooring and instrument meta data can be found in the appendix in Table A.1 and Table A.2, respectively. All instruments were newly bought and thus had recent manufacturer calibrations.
The raw data and the processed data are available on Pangaea and can be found in this list of data sets: von Appen (2019a).

Salinity was calculated from conductivity ratio, temperature, and pressure, potential density from salinity, temperature, and pressure, with a reference pressure of 0. These calculations were done with the SeaWater library of EOS-80 (http://www.cmar.csiro.au/datacentre/ext_docs/seawater.htm). The data processing was performed similar to the processing of previously recovered moorings, as documented in von Appen (2017).

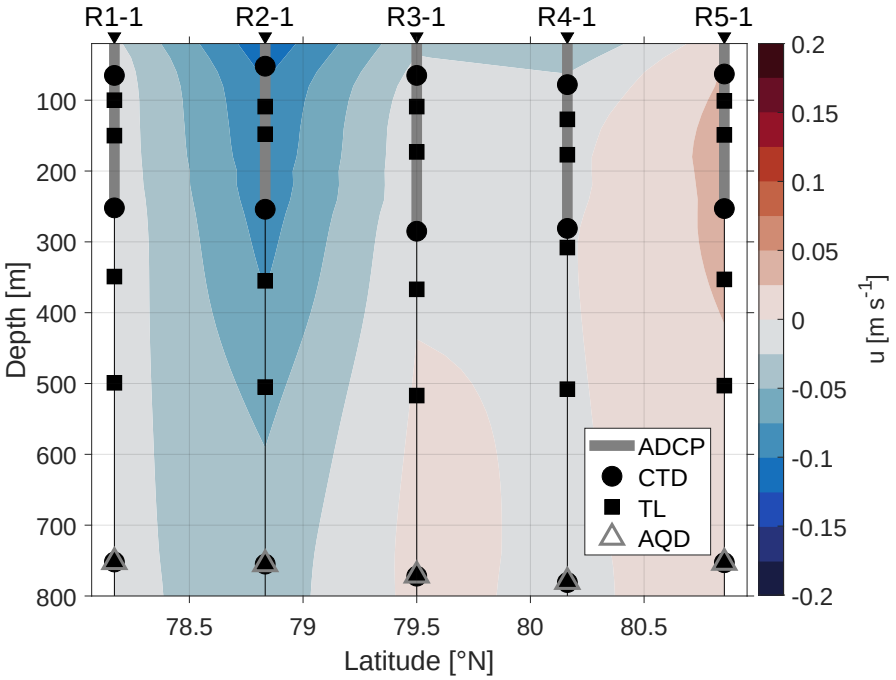

Figure 2.2: Gridded zonal velocity (m s^{-1}) section, averaged over the entire time period, with instrument locations in the water column. The grey bars mark the Acoustic Doppler Current Profilers (ADCPs), the black dots the CTDs (measuring conductivity, temperature, and pressure, i.e. depth), the black squares the temperature loggers (TLs), and the grey triangles the Aquadopps (AQDs).

2.1 Data gridding

As all instruments recorded at least every hour, a low-pass filter is applied at a period of 1 h to all the time series of instruments that recorded more often (i.e. the temperature loggers that recorded every 30 seconds, and the Aquadopps that recorded every 20 minutes). This is done by applying a 4th order Butterworth filter to the time series with linear interpolation through gaps before the filtering and removal of those gaps afterwards, if the gap duration significantly exceeded the lowpass filter period. Afterwards hourly values of the filtered time series are used so that all time series contain data points of the same frequency.
The data are interpolated with a minimum curvature gridding method with an added tension parameter (Smith and Wessel, 1990). The tension parameter is chosen to be 5 (with 0 = Laplacian interpolation, which gives a tent pole-like behaviour around data points, and ∞ = spline interpolation, which gives a smoother field, but the possibility of spurious peaks or valleys). This achieves a grid that is closest to the actual measurements, as evaluated by visual inspection. A search radius of $\pm$ 20 grid

points is applied, as this yields a smooth grid even in depths of low data coverage. The data are interpolated onto a grid with a temporal grid size of 1 h (i.e. the time step of the filtered measurements) and a vertical grid size of 20 m. The grid extends over a time period from 10 August 2016 to 19 July 2018 (as this is the period covered by all instruments; date of last mooring deployment to first mooring recovery) and over a depth from 40 m (20 m for velocity measurements) to 1100 m. This way no measurements are excluded. Technically the instruments furthest down in the water column only had a target depth of 750 to 780 m, but the moorings were at times subjected to strong motion and measurements acquired during those times are included in the interpolation. For analysis, the gridded data below 800 m is then removed. To achieve a coherent grid, the grid points at 20 m depth are added as NaNs for temperature, salinity, and potential density.

2.2 Handling of missing data

Except for a few single missing measurements, the CTDs only malfunctioned on three main occasions. At R3-1 the CTD at ∼265 m depth measured unexpected temperature values after 01 May 2017, likely because something was stuck in the CTD pump. This was corrected with an offset at first, but further evaluation led to the decision to disregard all temperature (and hence salinity) measurements after 01 May 2017 for this instrument. The CTD at ∼760 m depth at the same mooring recorded a peculiar rise and then offset in conductivity (and thus salinity) after 24 April 2017, which is consequently also disregarded. At R4-1 the CTD at ∼265 m depth stopped recording altogether after 31 July 2017 due to an empty battery, meaning there are no temperature, conductivity, or pressure measurements of this instrument available after this date.

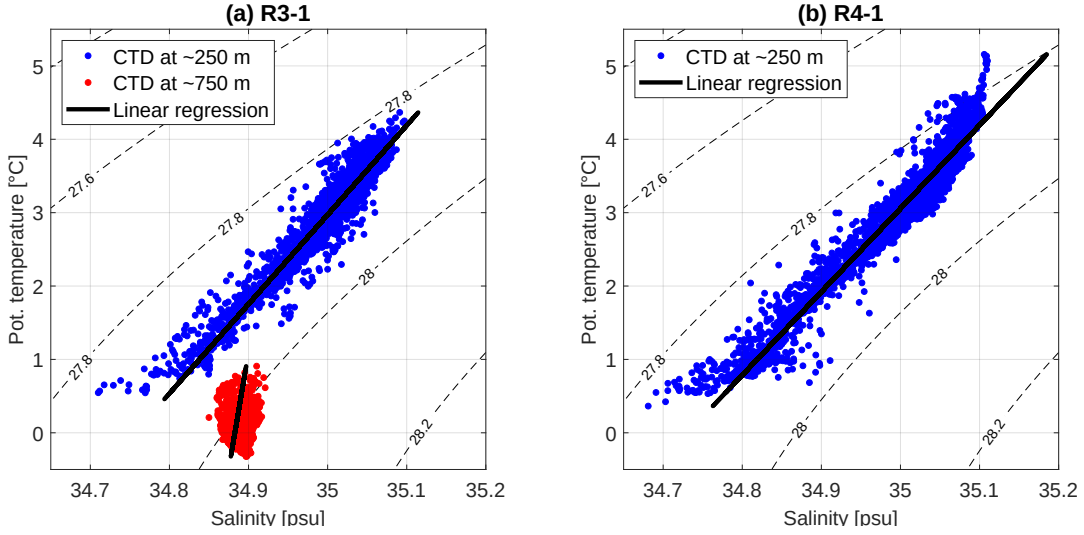

Figure 2.3: ΘS plot with linear regression of potential temperature (°C) and salinity (psu) of (a) the CTD measurements at ∼250 m (blue dots), and at ∼750 m (red dots) separately at R3-1, and of (b) the CTD measurements at ∼250 m (blue dots) at R4-1.

Missing temperature and pressure measurements are replaced with nearby ADCP measurements. The difference between temperature measurements of ADCP and CTD at R3-1 is on average 0.02°C with a standard deviation of 0.14°C, and at

R4-1 on average 0.03°C with a standard deviation of 0.61°C, which is deemed sufficient. Missing salinity measurements are calculated from temperature measurements, where the relationship between the two is determined by a linear regression with the data that is available at the instrument (Figures 2.3a,b). The residuals of the linear regression are randomly distributed (not shown) and this method is thus suitable in this context.
The ADCPs measured velocity profiles with 70 bins, of which approximately 8% are lost towards the surface, which translates roughly to the upper 20 m. At R2-1 and R3-1, three respectively four entire bins are removed, due to instruments or buoyancy floats at the corresponding depths, which have zero velocity relative to the ADCP and dominate the Doppler shift of the return signal for those bins instead of scatter from the water column. Other than that some data points are excluded randomly (1.84%, 7.75%, 7.13% 1.96%, and 1.01% at R1-1, R2-1, R3-1, R4-1, and R5-1, respectively).
The temperature loggers recorded without any issues and no data are excluded.

2.3 Calculations

Different variables are derived from the gridded data and are calculated as follows:

2.3.1 Potential temperature Θ

Potential temperature is calculated with the SeaWater library of EOS-80 from the gridded salinity, temperature, and pressure, with a reference pressure of 0. Using temperature instead of potential temperature results in a small error that is naturally largest at the deepest point of the grid (i.e. at 800 m, about 0.036°C).

2.3.2 Buoyancy frequency N^2

Buoyancy frequency squared is calculated from potential density ρ profiles with a centred difference for each vertical grid point j, with vertical grid spacing $\Delta z = 20$ m and $j = 1$ at 20 m. Gravity g is calculated from the latitude of each mooring.

$$N(j)^2 = -\frac{g}{\rho(j)} \cdot \frac{\rho(j-1) - \rho(j+1)}{2\Delta z}. \tag{2.1}$$

This means losing one value at the top and the bottom of the grid, so a NaN is added for each to achieve a coherent grid. The centred difference (evaluated over $2\Delta z$) also adds a small smoothing compared to forward or backward differences, which are evaluated over Δz. Gridded buoyancy frequency displays some negative values, but logarithmic probability density functions reveal them few and smaller in magnitude than the positive values. It is thus feasible to set all negative values to the smallest positive value calculated at each mooring to be able to apply a logarithmic scale.

2.3.3 Eddy kinetic energy (EKE)

Eddy kinetic energy is calculated from the deviation from the mean of zonal velocity u and meridional velocity v for each grid point as follows:

$$EKE = \frac{1}{2} \cdot (u'^2 + v'^2). \tag{2.2}$$

To evaluate mesoscale variability in particular, the velocity data are bandpass filtered between 2 and 30 days (as done in von Appen et al., 2016), and the filtered u, v are the u', v' that are applied in Equation 2.2. The short period limit avoids tides and inertial oscillations and the long period limit removes the seasonal cycle and interannual variations.

2.4 Seasonal cycle

The seasonal cycle of each variable is determined by first calculating monthly averages, i.e. averaging over all measurements from each of the 24 months of measurements (August 2016 to July 2018). This is done for each of the 5 moorings and each of the 40 depth levels individually. For the seasonal cycle of the full vertical length of the grid, the monthly averages are then averaged over the 40 depth levels. Lastly, since there are two years of measurements available, the seasonal cycle is extracted by averaging over two of the same months. This means, the months July and August are slightly biased towards the year 2017, as the measurements only start in the middle of August 2016 and end in the middle of July 2018.
The seasonal cycle of the standard deviation of potential temperature, salinity, and potential density is determined by averaging the data over depth first, as the standard deviation would otherwise mainly reflect the variability in the water column, which is mostly larger than the variability in time. Then we proceed by calculating monthly standard deviations, and then averaging over two of the same months.

2.5 Water mass definitions

Water mass definitions for PW, AW, and AAW follow Rudels et al. (2005), while DW is simply defined as all water higher in density than AW and AAW. This is similar to water mass definitions in publications regarding the recirculation (e.g. Marnela et al., 2013; Wekerle et al., 2017; Richter et al., 2018).

The seasonal cycle of parts of the water column that fall into a specific water mass definition is plotted by calculating the seasonal cycle only from measurements that fall into said definition, and only if the water mass makes up at least 10% of the measurements during a month, both in time and in the vertical. 10% can thus mean, the water mass occupied 10% of the upper 800 m (i.e. 80 m) all the time, or all of the upper 800 m during 10% of the time, or anything in between. This avoids averages being calculated from very little data. Nonetheless the averages are often biased towards one year, as the amount of measurements that fall into one definition in a month varies from one year to another (Figure 2.4). To calculate the seasonal cycle, the average of two of the same months is taken — if only one of the months surpasses the 10% mark, neither of the months is considered.

Table 2.1: Water mass definitions after Rudels et al. (2005). Boundaries of potential temperature θ in °C and potential density σ in kg m^{-3} are given. Potential density is referenced to the sea surface.

Water mass	**Acronym**	**Definition**	**Remarks**
Polar Water	PW	$\sigma \leq 27.7$	Termed Polar Surface Water (PSW) in Rudels et al. (2005), here both the definitions for PSW and warm PSW are included
Atlantic Water	AW	$27.7 < \sigma \leq 27.97$, $\theta > 2$	Here only the definition outside the WSC is included
Arctic Atlantic Water	AAW	$27.7 < \sigma \leq 27.97$, $0 < \theta \leq 2$	Here only the definition outside the Arctic Ocean is included
Deep Water	DW	$\sigma > 27.97$	Not defined in Rudels et al. (2005)

2.6 Velocity spells

Since the variability of the zonal and meridional velocities and hence EKE is so high at R4-1, we try to identify velocities associated with eddies. Meridional velocities are dominated by southward motion, so in this regard only zonal velocities are considered. By visual inspection of Hovmöller diagrams, times during which zonal velocity was either clearly westward or clearly eastward in most of the water column, and sustained over at least one day, are chosen. Only those associated with a subsurface EKE maximum (or a surface EKE maximum with high EKE below the surface as well) are, what we define as a westward/eastward 'spell'. This yields 48 westward spells and 55 eastward spells. Spells that exceed an average westward/eastward velocity of 0.05 m s^{-1} are used in the analysis. Since westward spells are generally stronger, this leaves 44 westward spells and 34 eastward spells.

2.7 Sea ice concentration

For mapping different sea ice concentrations, we use data from the Advanced Microwave Scanning Radiometer sensor AMSR-2 (University of Bremen, 2015) for the years 2013–18 (Spreen et al., 2008), as it was done by von Appen et al. (2016).

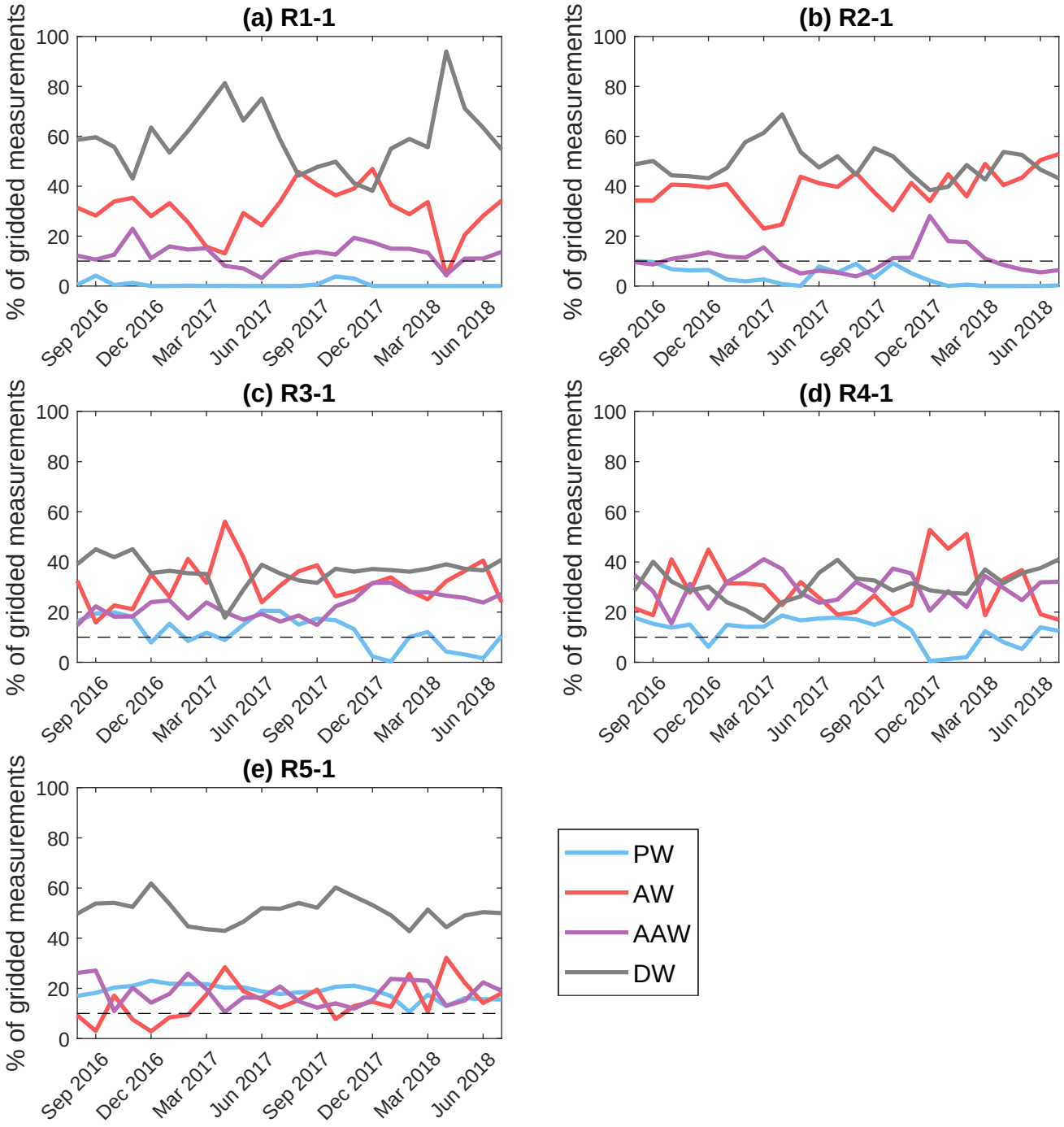

Figure 2.4: Percentage of gridded measurements that fits the PW (blue), AW (red), AAW (purple), DW (grey) definition in each month of the observation period at (a) R1-1, (b) R2-1, (c) R3-1, (d) R4-1, and (e) R5-1.

Chapter 3

Results and Discussion

3.1 General hydrography

On average over the full time series, a layer of water with relatively high potential temperature is located at the surface at R1-1 (78°10'N) and progressively further down in the water column, and weakening towards the north (Figure 3.1a). The maximum potential temperature is at R2-1 (78°50'N), roughly between 100 and 200 m. The layer of maximum salinity is located further down in the water column at approximately 200–400 m, but also thins towards the north (Figure 3.1b). This pattern in potential temperature and salinity leads to the AW layer being thickest at R2-1. Both at R1-1 and R2-1 it is as shallow as at least 40 m (above we have no measurements), and located below ∼180 m at R3-1 (79°30'N), R4-1 (80°10'N), and R5-1 (80°50'N). Above the AW layer the water is characterised by colder temperatures and the lowest salinity in the measurements, thus being of very low density (Figure 3.1c) and fitting into the PW definition. This is likely present due to partial or continuous ice cover. The AW layer is thinnest at R5-1, where we also find the lowest potential temperature and salinity close to the surface (Figures 3.1a,b).
The main features in the time-averaged velocity field are westward velocities at R2-1 with a maximum amplitude close to the surface and decreasing amplitude with depth (Figure 3.1e), and southward velocities at R4-1 with a minimum in the AW layer between 100 and 300 m (Figure 3.1f). The former represents a continuous branch of recirculation towards the west at R2-1, as also indicated by the potential temperature, salinity, and AW layer thickness maximum at this mooring. By contrast, the situation at R4-1 may be related to mesoscale eddies, which vary in velocity on much shorter timescales, and do not necessarily show up in a two year-average. This is further supported by a maximum in EKE at around 160 m at R4-1 (Figure 3.1d). EKE is also comparatively large at R1-1 close to the surface.
The main difference between the two years of measurements is that the AW layer is thinner and maximum potential temperature and salinity reaches more to R3-1 from the south in the first year (2016/17, not shown) compared to the second year (2017/18, not shown). The velocity field looks fairly similar in the two years, with stronger northward velocities at R2-1 and southward velocities at R3-1 in the first year (2016/17) compared to the second year (2017/18).

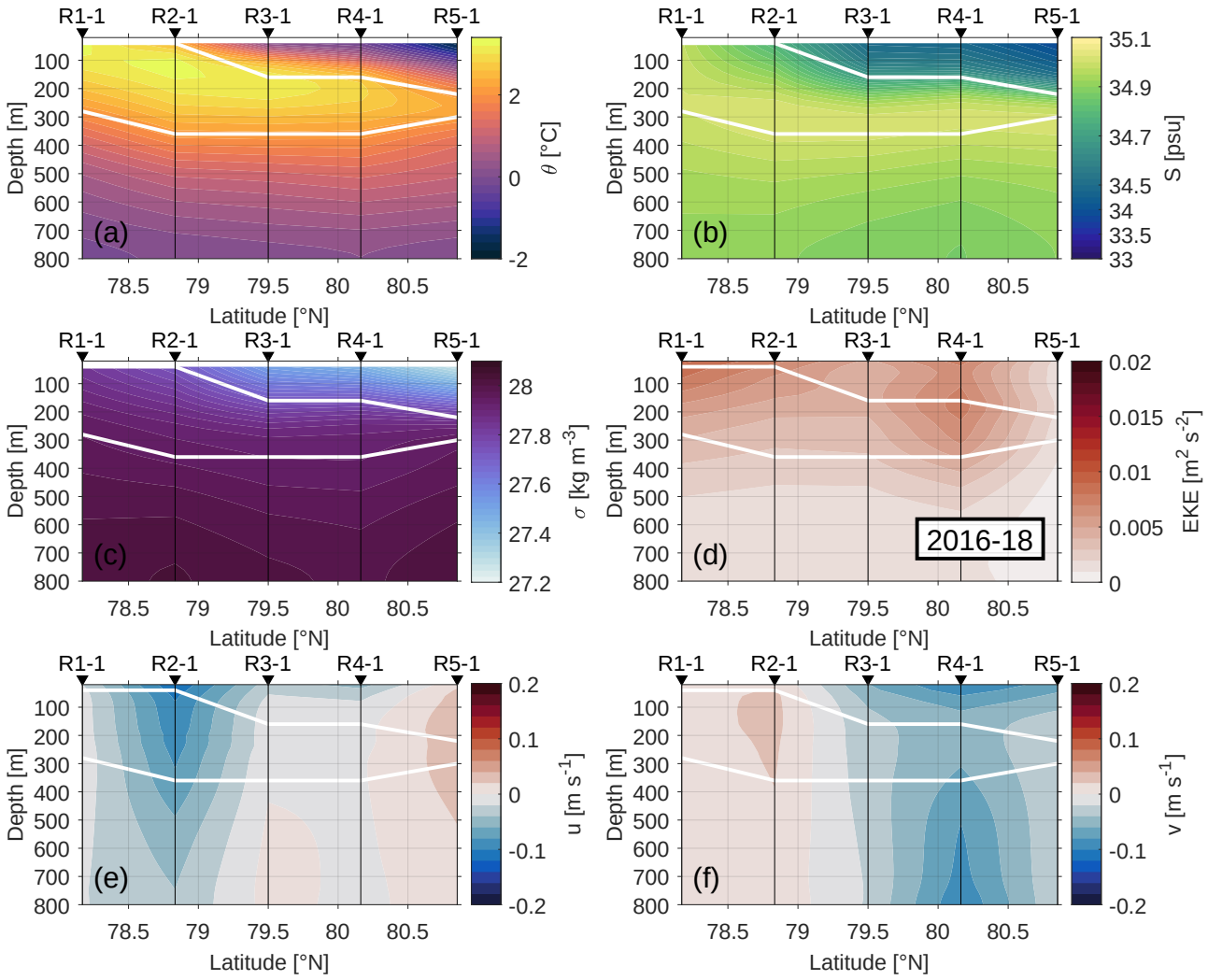

Figure 3.1: Gridded sections of (a) potential temperature (°C), (b) salinity (psu), (c) potential density (kg m^{-3}), (d) eddy kinetic energy (m^2 s^{-2}), (e) zonal velocity (m s^{-1}) and (f) meridional velocity (m s^{-1}), averaged over the entire time series. Note the nonlinear colour bar of salinity. The white lines mark the lower and upper boundary of the AW layer.

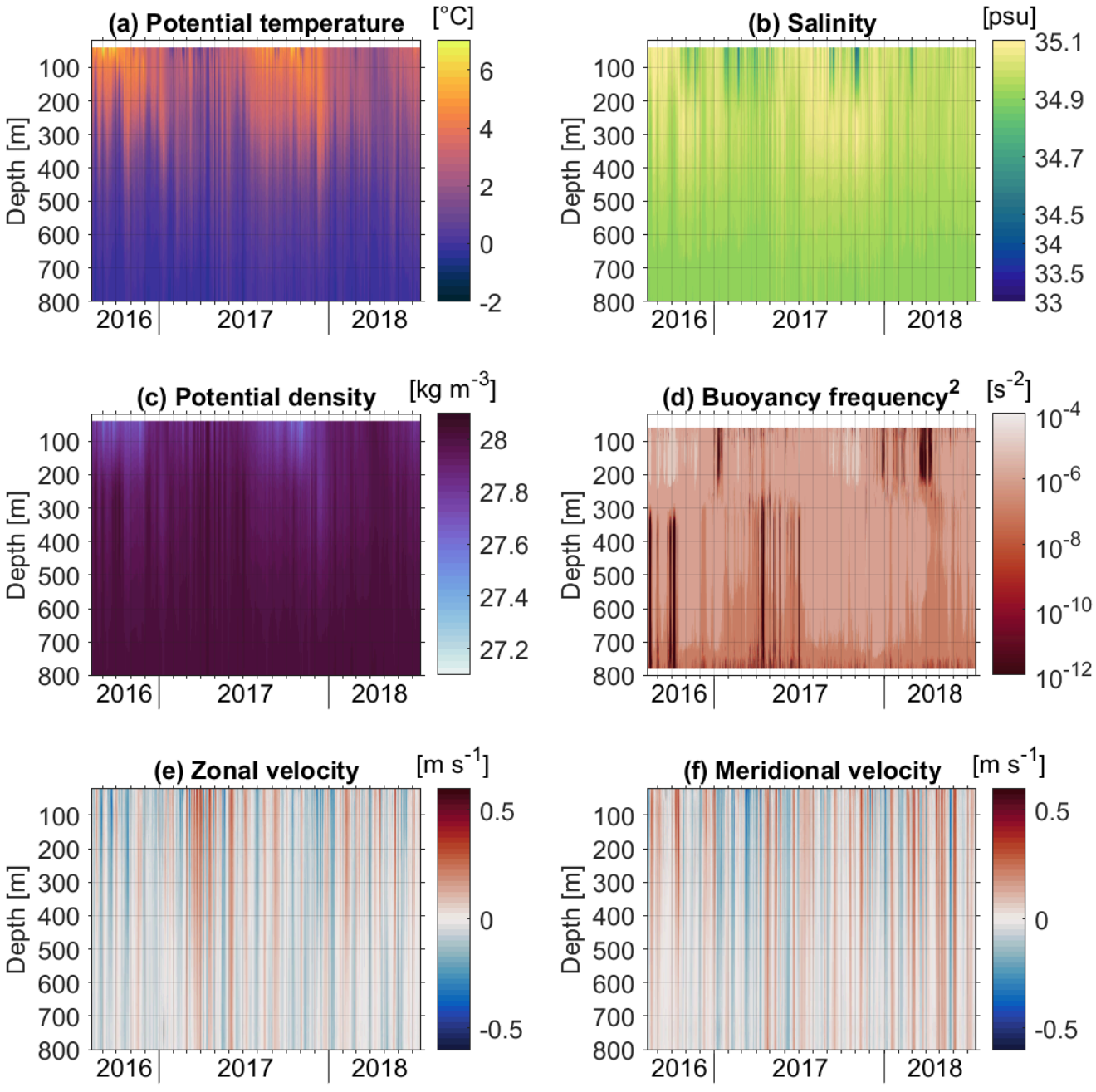

Figure 3.2: Gridded (a) potential temperature (°C), (b) salinity (psu), (c) potential density (kg m^{-3}), (d) buoyancy frequency squared (s^{-2}), (e) zonal velocity (m s^{-1}), and (f) meridional velocity (m s^{-1}) at R1-1 between August 2016 and July 2018. Note the nonlinear colour bar of salinity.

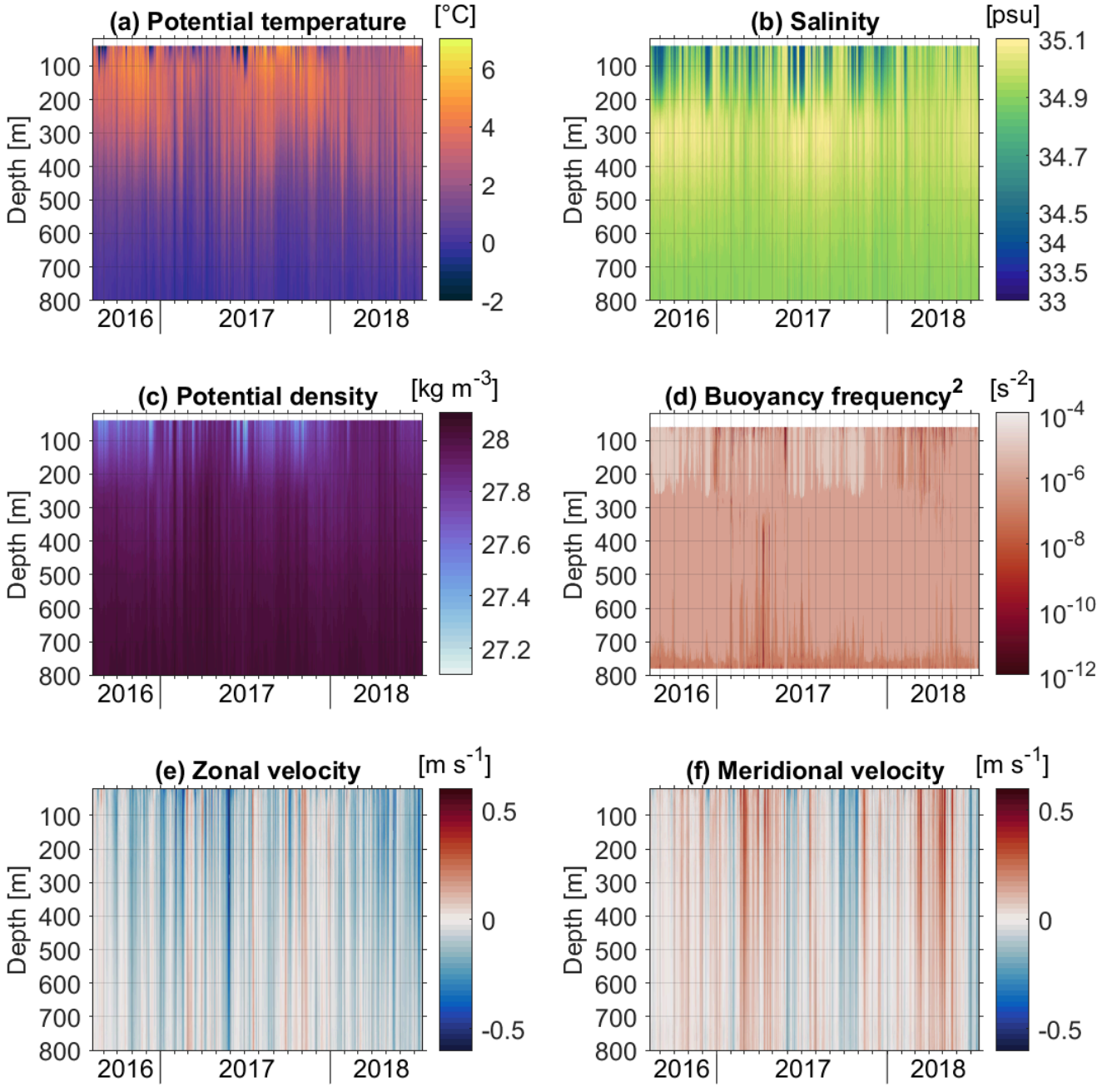

Figure 3.3: As in Figure 3.2, but at R2-1.

3.1.1 R1-1

R1-1 is the southernmost mooring at 78°10'N, close to the Hovgaard Ridge. At R1-1 potential temperature goes through a seasonal cycle with a maximum in late summer/autumn that seems to propagate down in the water column (Figure 3.2a). The water column appears to be influenced strongly from the surface by the atmosphere. The salinity maximum in ∼250–400 m depth is most apparent during summer and autumn with some short, fresher periods close to the surface in autumn/winter (Figure 3.2b). Potential density seems to reflect the pattern of potential temperature, but the short, fresher periods of salinity are also recognisable (Figure 3.2c). R1-1 displays the most noticeable negative values in buoyancy frequency (which are likely measurement or interpolation errors, but are still indicative of periods of very low stratification and have therefore been replaced by the smallest value measured at the mooring here). Low stratification is apparent early in the year in the upper water column and during spring/summer in the lower water column (Figure 3.2d). The water column is most stable during summer/autumn in the upper water column, when the surface waters are warmed by the atmosphere.
There are both westward and eastward zonal velocities of similar magnitude (Figures 3.2e,f), with more eastward motion and the highest magnitudes during spring/summer 2017. The meridional velocities are slightly stronger than the zonal velocities and both northward and southward of similar magnitude. They are more barotropic during the first half of the year, when the upper part of the water column is weakly stratified.

3.1.2 R2-1

R2-1 is located in between the Hovgaard Ridge and the Spitsbergen Fracture Zone, southwest of the Molloy Hole. It is on the same latitude as the zonal array of moorings in the Fram Strait, at 78°50'N. Similar to R1-1 there appears to be a seasonal cycle in potential temperature with a maximum in late summer/autumn that seems to propagate down in the water column with time (Figure 3.3a). There are some short, colder periods during the first year, which coincide with distinct short, fresher periods in salinity. There is much more variability in the upper water column in salinity compared to R1-1 with said distinct short, fresher periods, though they seem to almost stop in 2018 (Figure 3.3b). The salinity maximum lies between ∼250–450 m, slightly lower than at R1-1. Potential density reflects both the general pattern of potential temperature and the short, fresher periods of salinity (Figure 3.3c). The upper water column is most stable during summer/autumn (Figure 3.3d). Zonal velocities are mostly westward, with particularly strong velocities at the end of May 2017 of about -0.4 m s^{-1}, sustained over several days (Figure 3.3e). Meridional velocities are mostly northward during February to May and of equal strength as the westward component of the flow, but weaker and more variable in direction during the rest of the year (Figure 3.3f).

3.1.3 R3-1

R3-1 is located northeast of the Molloy Hole, centred in between the Spitsbergen and the Molloy Fracture Zone at 79°30'N, and sometimes ice-covered (Figure 3.4). At R3-1 the maximum potential temperature is mostly located between ∼80–280 m,

which is further down in the water column than at R1-1 or R2-1 (Figure 3.5a). It still seems to slightly propagate downwards starting in late summer/early autumn, quickly cooling from the surface downward. Above, the water is much colder, but there is a considerable amount of variability. The salinity maximum is located at the same depth as at R2-1, between ∼250–450 m, and is present throughout the year, though not as much in 2018 (Figure 3.5b). The upper water column is dominated by fresher waters that reach down to ∼250 m, with the exception of some more saline time periods, mostly during winter. Here, potential density is already strongly dominated by the salinity structure (Figure 3.5c). Due to the fresh surface layer, the water column is very stable throughout the year (Figure 3.5d). Even during times of reduced stratification, buoyancy frequency is much larger than at R1-1.

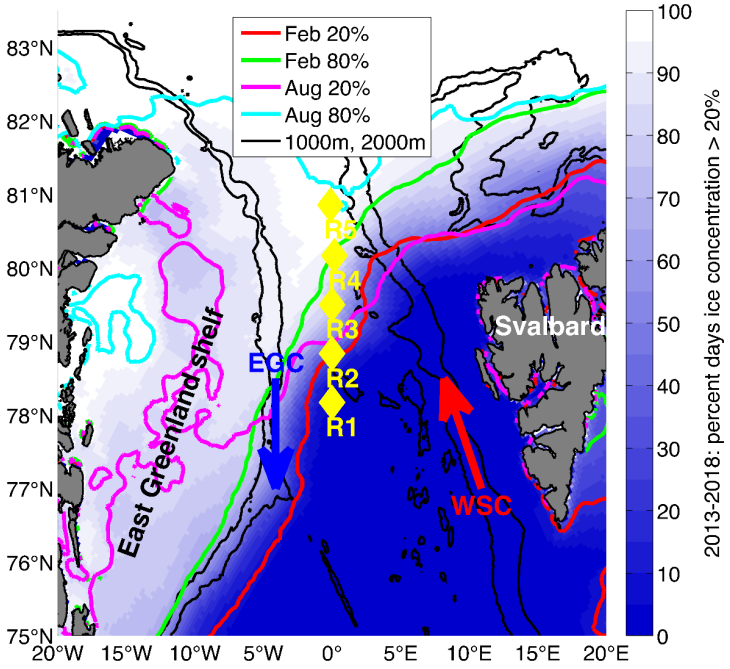

Figure 3.4: Map of Fram Strait with the mooring positions (yellow diamonds), schematic current direction of the WSC (red arrow), and the EGC (blue arrow), as well as contour lines of 20% sea ice concentration in February (orange) and August (pink), and of 80% sea ice concentration in February (green) and August (cyan). 2013–2018 average percent of days with ice concentration of more than 20% in the background.

There are both westward and eastward zonal velocities, sometimes of very small magnitude, also for rather longer periods (Figures 3.5e,f). Most notable are strong westward and partly eastward velocities in March/April 2017 with a magnitude of ∼0.4 m s^{-1}, and strong eastward velocities in March 2018 up to 0.45 m s^{-1}. The meridional velocities are generally of larger magnitude than the zonal velocities and rather southward, mostly during winter. There is, however, strong northward flow in April 2017 of more than 0.5 m s^{-1}.

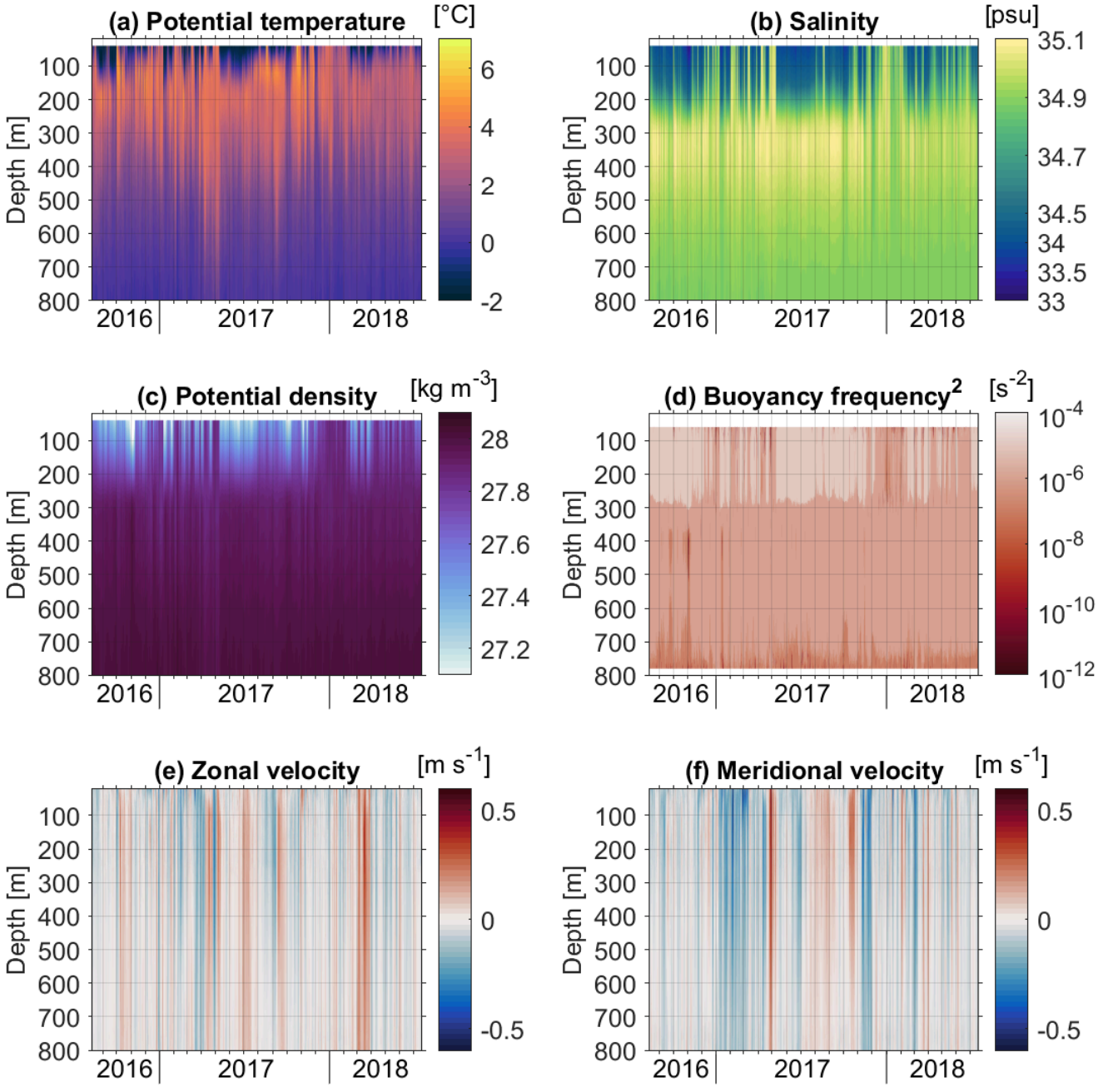

Figure 3.5: As in Figure 3.2, but at R3-1.

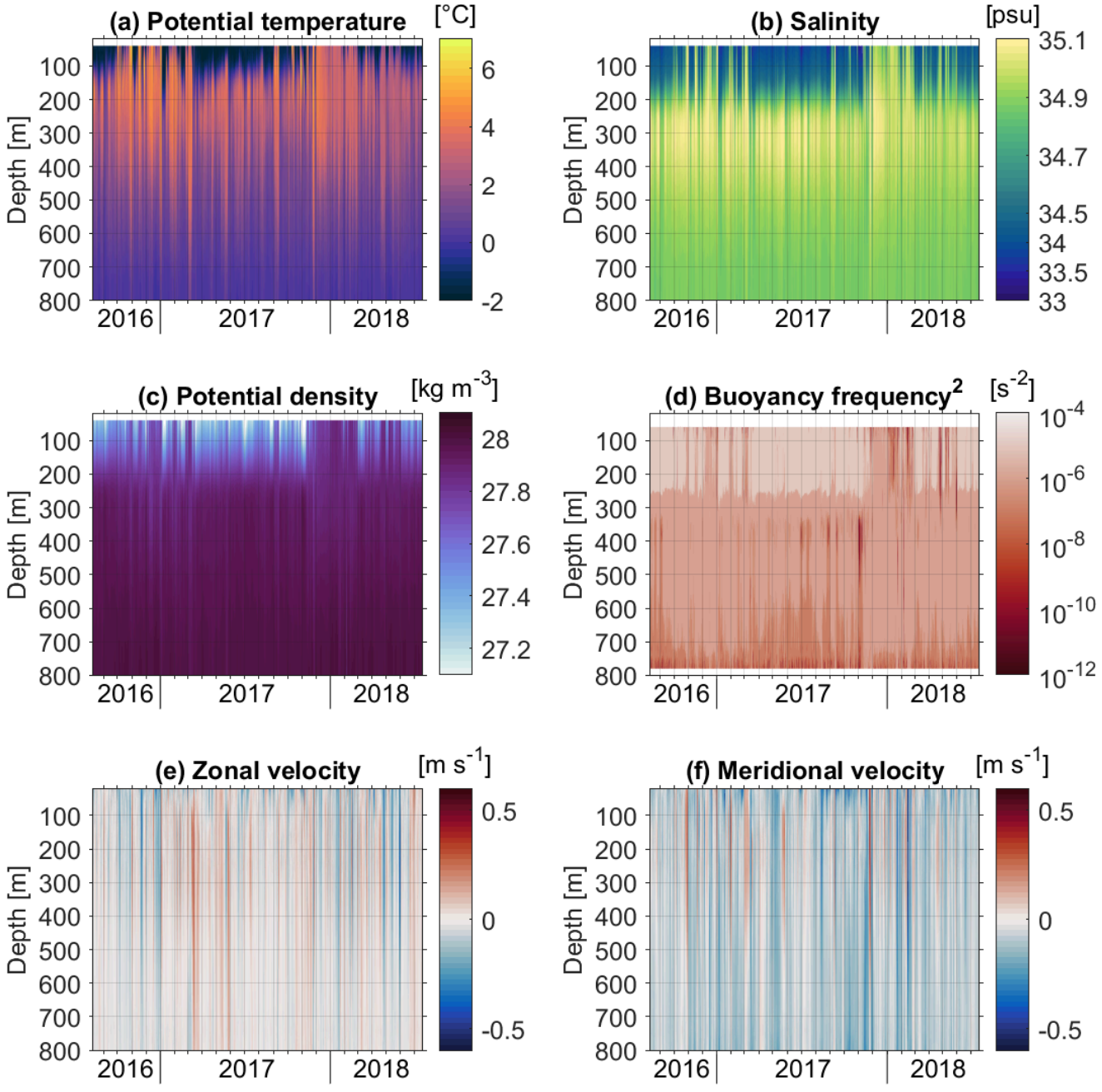

Figure 3.6: As in Figure 3.2, but at R4-1.

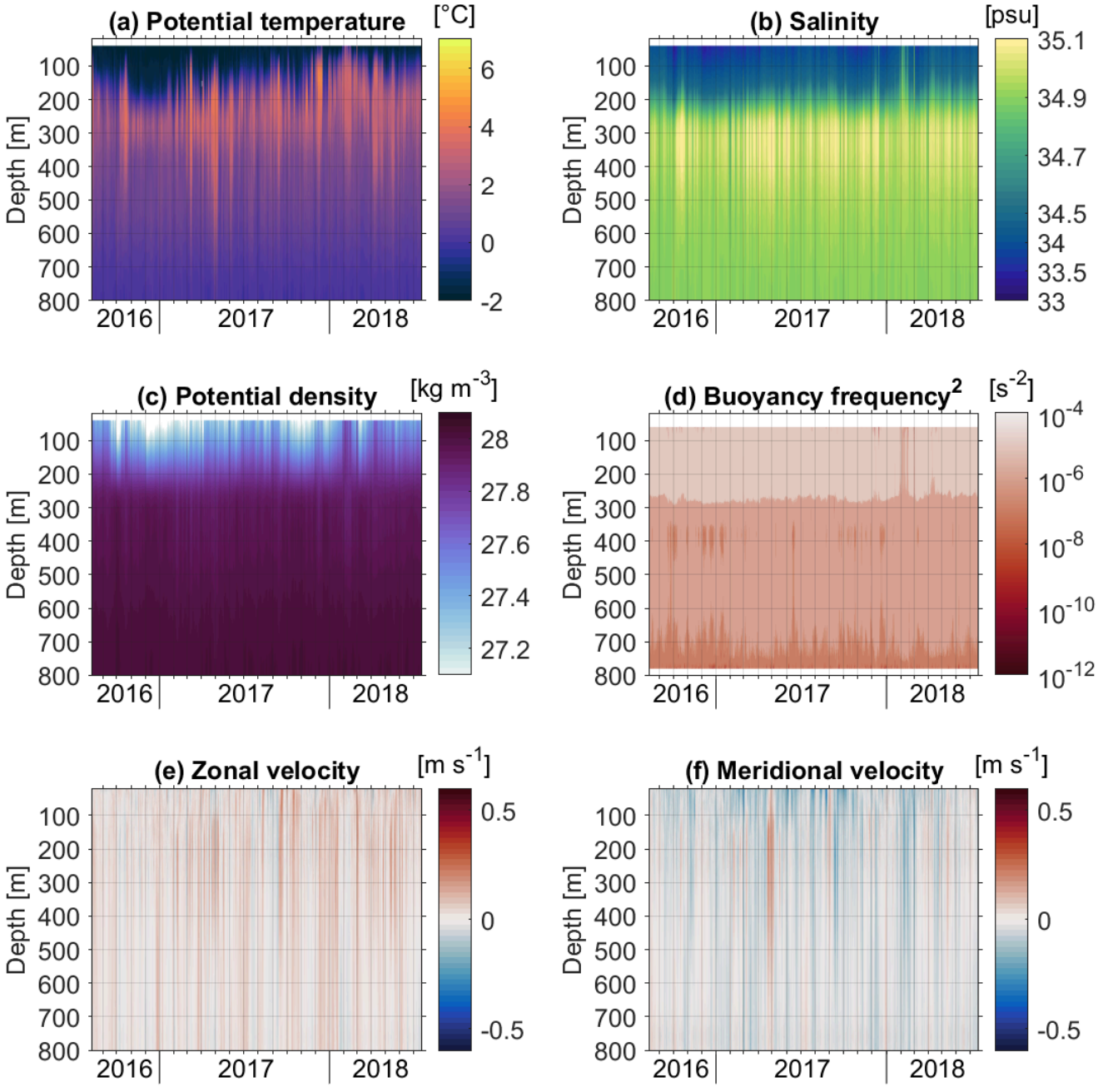

Figure 3.7: As in Figure 3.2, but at R5-1.

3.1.4 R4-1

R4-1 is located on the Molloy Fracture Zone at 80°10'N, and usually ice-covered (Figure 3.4). Here, measurements display the highest variability in potential temperature throughout the water column (Figure 3.6a). The highest temperatures are present during late autumn/winter, i.e. much later in the year than further south. During spring/summer/early autumn, the temperatures in the upper water column are clearly colder. The upper water column is generally fresher than at R3-1, but with distinct short, saline periods during winter. The salinity maximum resides between ∼250–450 m, as at R2-1 and R3-1, and is (as at R3-1) less pronounced during 2018 (Figure 3.6b). Potential density again mostly reflects salinity here, though salinity and potential temperature behave remarkably similar (Figure 3.6c). The water column is generally stable, with some smaller buoyancy frequency values during winter, when the fresh surface layer is diminished (Figure 3.6d).
The variability in zonal velocity is large, there are mostly very short periods of either westward or eastward flow that last a couple of days (Figure 3.6e). The highest velocities do not necessarily reach up to the surface, unlike at R1-1 and R2-1. Meridional velocities are mostly southward throughout the year and barotropic, but sometimes interrupted by northwards velocities that appear much less barotropic (Figure 3.6f).

3.1.5 R5-1

R5-1 is the northernmost mooring at 80.85°N, west of the Yermak Plateau, significantly closer to the Svalbard shelf than the Greenland shelf, and generally ice-covered (Figure 3.4). Potential temperature at R5-1 is always close to the freezing point in the upper water column (Figure 3.7a). This layer reaches deeper during the first winter and less so during the second one. The maximum potential temperature is located slightly further up in the water column compared to other moorings and much colder, ∼4∘C. Similar to temperature, very fresh water is situated in the surface layer above the salinity maximum at ∼250–250 m (Figure 3.7b). The maximum is less pronounced in winter. Accordingly a layer of low potential density (the well-established PW layer) lies above high density waters below, resulting in a very stable water column throughout the year, particularly in the upper water column (Figures 3.7c,d).
Zonal velocities are mostly eastward, meridional velocities mostly southward, both of small magnitude (compared to the other moorings) and with no obvious seasonality (Figures 3.7e,f).

3.1.6 Different mooring regimes

The picture that forms at this point is one of five moorings that fit into very different regimes. The second-northernmost and the second-southernmost mooring, R2-1 and R4-1, respectively, are indicative of AW recirculation branches with different properties. The middle mooring, R3-1, may be influenced by these recirculation branches at some times during the year. The southernmost mooring, R1-1, appears to be largely influenced by the Greenland Sea, while the northernmost mooring, R5-1, is situated in the Arctic Ocean outflow region. Accordingly, they display a different amount of variability on several timescales. The available two year time

series with hourly temporal resolution gives us the opportunity to evaluate seasonal variability at the five moorings, and, where relevant to the recirculation, mesoscale variability. In terms of interannual variability, it allows us little more than to assess the difference between the seasonal cycles of the two years. In the following, we will first briefly discuss the situation at the moorings affected mainly by the Greenland Sea and the Arctic Ocean outflow, then direct our focus on the recirculation, as this is the main topic of this thesis.

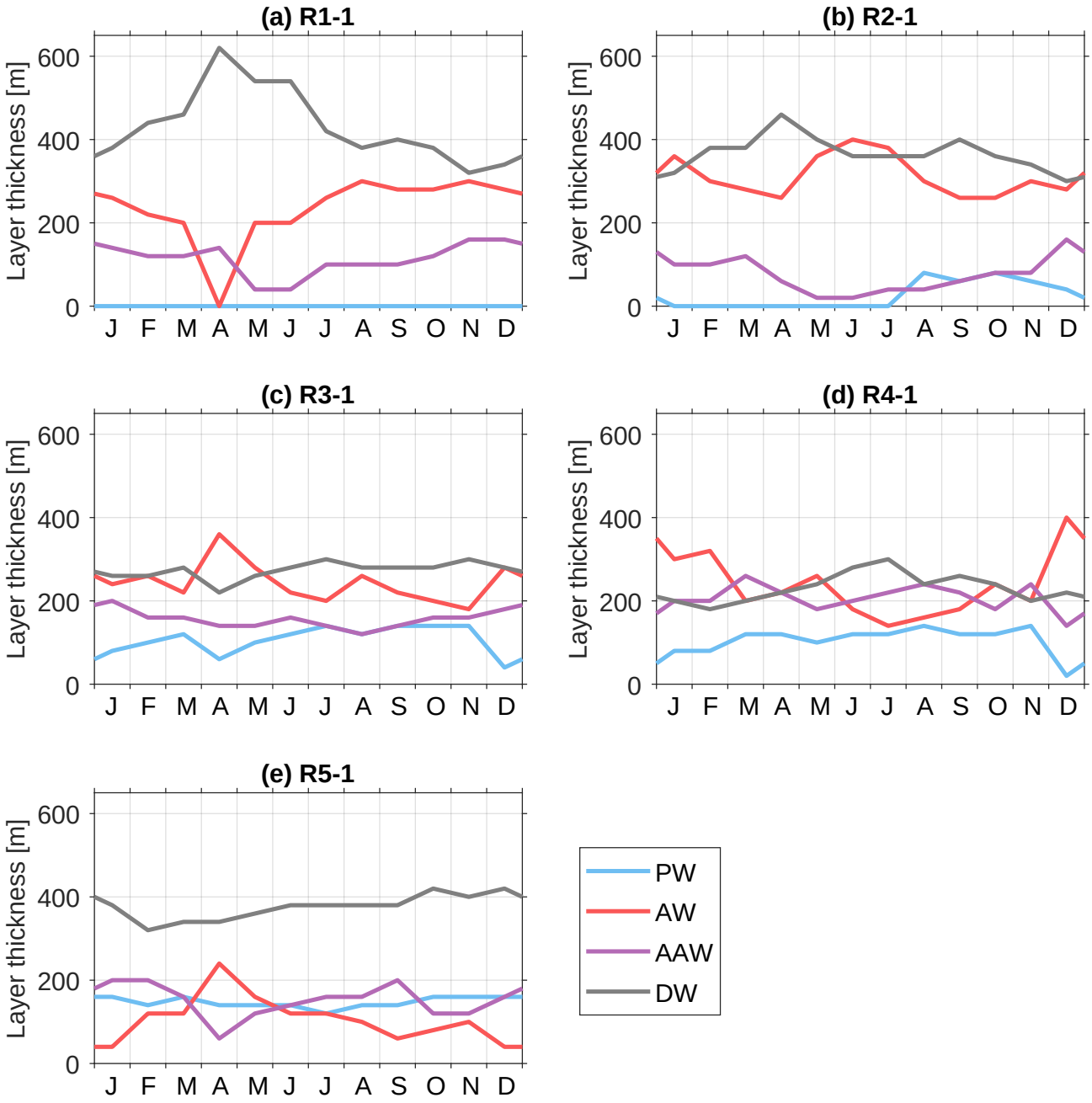

Figure 3.8: Seasonal cycle of water mass layer thickness (m) of PW (blue), AW (red), AAW (purple), and DW (grey) at (a) R1-1, (b) R2-1, (c) R3-1, (d) R4-1, and (e) R5-1.

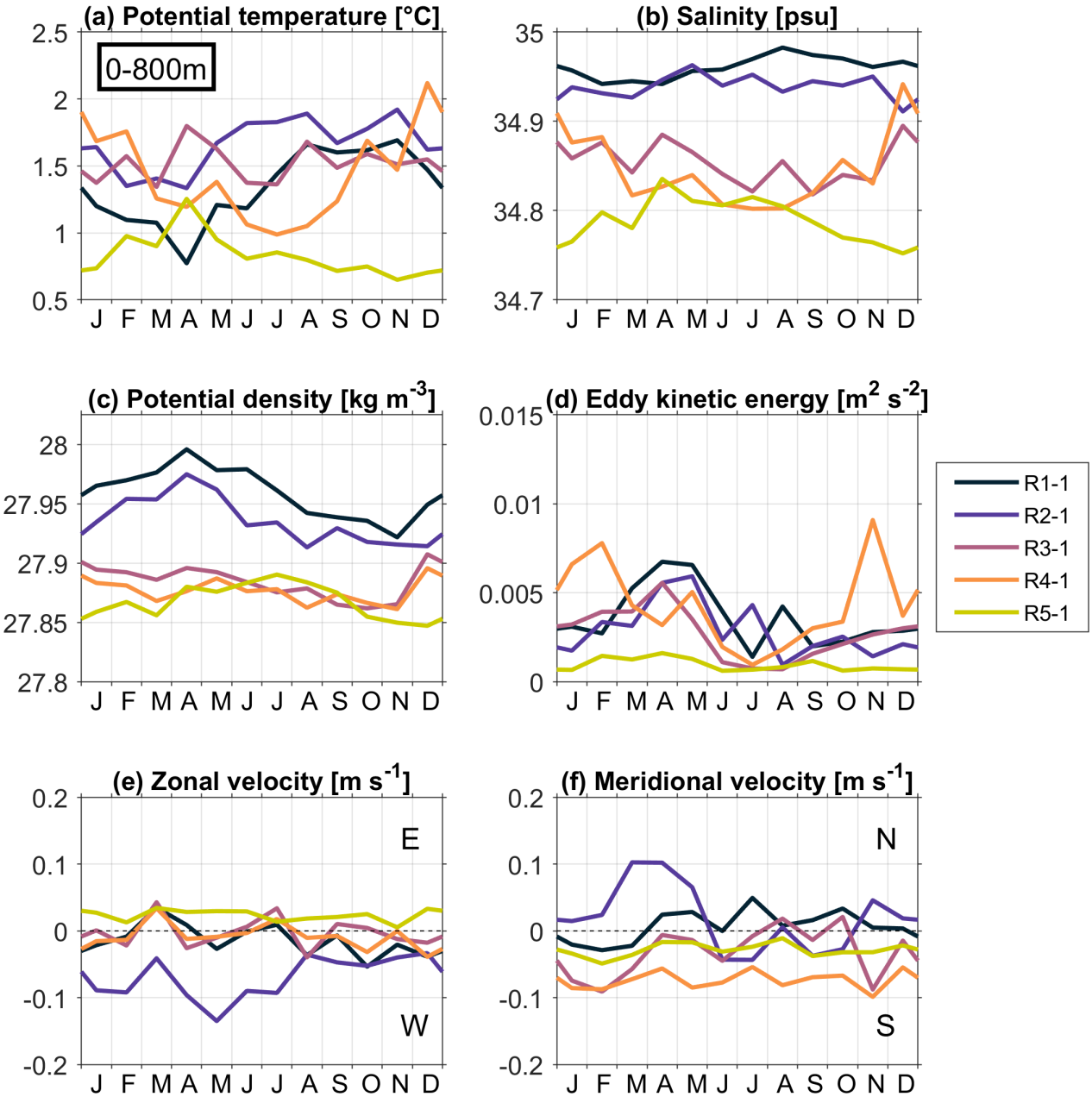

Figure 3.9: Seasonal cycle of (a) potential temperature (°C), (b) salinity (psu), (c) potential density (kg m^{-3}), (d) eddy kinetic energy (m^2 s^{-2}), (e) zonal velocity (m s^{-1}), and (f) meridional velocity (m s^{-1}) from all gridded measurements at R1-1 (dark blue), R2-1 (violet), R3-1 (dark pink), R4-1 (orange), and R5-1 (green). Note that there are no data available in the upper 40 m for potential temperature, salinity, and potential density, and in the upper 20 m for eddy kinetic energy, zonal and meridional velocity.

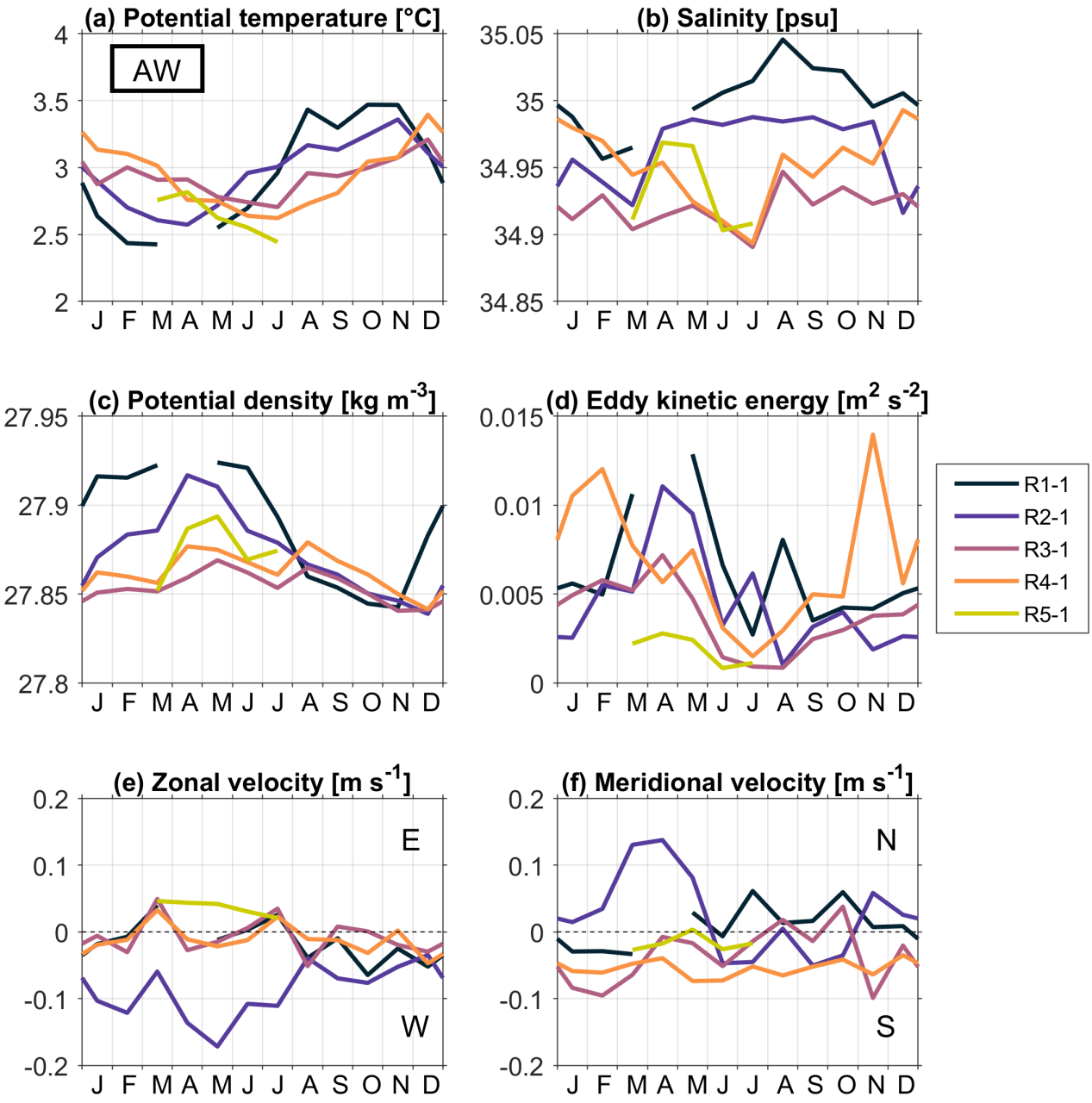

Figure 3.10: Same as Figure 3.9, but only for gridded measurements that fit the AW definition. Note that axis limits for potential temperature, salinity, and potential density are different to the ones in Figure 3.9. In months, during which less than 10% of the gridded measurements fall into the definition of AW, no monthly mean is calculated.

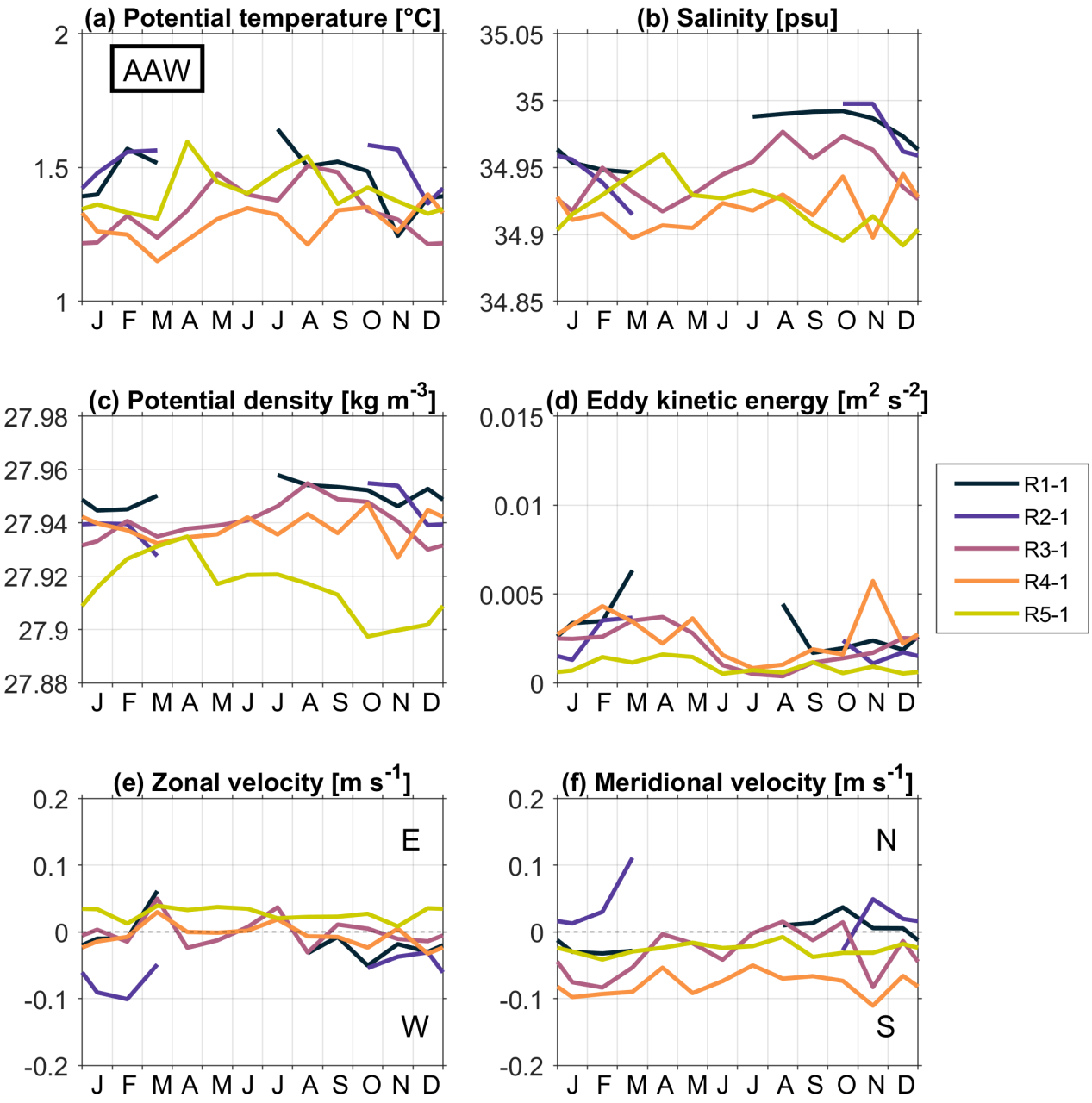

Figure 3.11: Same as Figure 3.9, but only for gridded measurements that fit the AAW definition. Note that axis limits for potential temperature, salinity, and potential density are different to the ones in Figure 3.9. In months, during which less than 10% of the gridded measurements fall into the definition of AAW, no monthly mean is calculated.

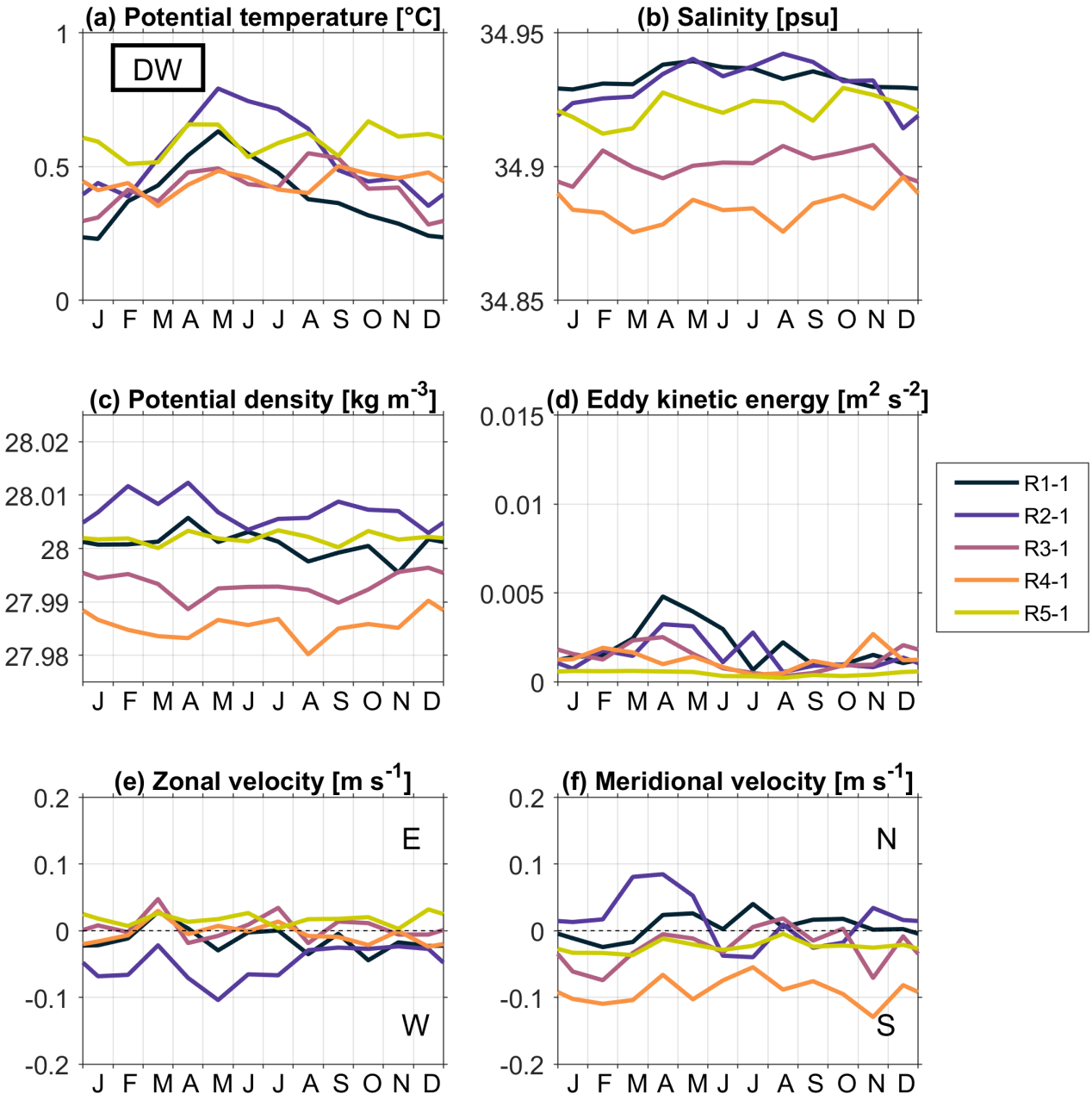

Figure 3.12: Same as Figure 3.9, but only for gridded measurements that fit the DW definition. Note that axis limits for potential temperature, salinity, and potential density are different to the ones in Figure 3.9.

3.2 Greenland Sea domain

It is apparent from the Hovmöller diagram (Figure 3.2) that R1-1 goes through a seasonal cycle largely affected by the atmosphere with maximum potential temperature in late summer/autumn. Low stratification is present early in the year in the upper water column, then during spring/summer in the lower water column. In the Greenland Sea the upper part of the water column is largely dominated by the seasonal cycle of the atmosphere and wintertime convection (Brakstad et al., 2019), so R1-1 is likely strongly influenced by the hydrography of the Greenland Sea.

3.2.1 Seasonal variability

There is very little PW present and only in the months of August to November, as well as in March and April 2017 (Figure 2.4a). In none of the months does the PW make up more than 10% of the gridded measurements, so there is no seasonal cycle calculated for this water mass (see Chapter 2.4 for more information). AW layer thickness is maximal in August to November and minimal in March to June (with a layer thickness of 200 m still, but no AW at all in April, Figure 3.8a). AAW layer thickness is, however, maximal in April, and minimal in May and June, possibly indicating that the water that fits the AAW definition in April (and potentially also other months) is AW that has simply cooled below the 2°C threshold and not necessarily reached the Arctic Ocean. The DW layer is also thickest in April and thinnest in November/December, further suggesting that the cooled AW has become so dense that it fits the DW definition, i.e. deep convection occurs.
Potential temperature displays a clear seasonal cycle with a maximum in August to November and a minimum in April (mainly reflecting the amount of AW at R1-1, Figure 3.9a). The AW itself also has a strong seasonal cycle with a maximum in October/November and a minimum in February/March (Figure 3.10a), which illustrates the influence of the atmosphere on the ocean at this latitude. The DW at R1-1 has the strongest seasonal cycle in potential temperature of all moorings with a minimum in January and a maximum in August, opposing the seasonal cycle of AW with a slight lag of 1–2 months (Figure 3.12a). Together with the seasonal cycle of water mass layer thickness, this implies the water mass transformation from AW to denser DW. Salinity generally varies very little and is largest at R1-1, with the clearest seasonality in the AW with a maximum in September and a minimum in February, though this is a small variation compared to the other moorings (Figure 3.10b). During months, when there is AAW present, the same seasonal cycle is indicated in the AAW as well (Figure 3.11b). Consequently, variations in potential density reflect the seasonal cycle of potential temperature (Figure 3.9c). Due to the high salinity at this mooring, the highest densities are recorded here throughout the year, with a minimum of 27.92 kg m^{-3} in November and a maximum of 28.00 kg m^{-3} in April on average in the upper 800 m of the water column. This fits well into the definition of DSOW ($\sigma > 27.8$ kg m^{-3} and $\theta \leq 2°C$, Tanhua et al., 2005), which means this water could ultimately contribute to the overflow across the Greenland-Scotland-Ridge, though the same applies to the water at the other moorings as well. It appears to be a bit lighter than what was found in the central Greenland Sea the preceding years, but slightly denser than what was found at the outer rim of the Boreas Abyssal Plain (Figure 3b in Brakstad et al., 2019). The variability in

potential temperature, salinity, and potential density is much smaller compared to the other moorings (Figure C.1a,b,c). R1-1 has the weakest stratification out of all the moorings, with a minimum in AW during January to May (not shown).
Both zonal velocity and meridional velocity are weak, variable in direction, and fairly barotropic (as the same signal can be seen in all water masses, Figures 3.9e,f, 3.10e,f, 3.11e,f, 3.12e,f). EKE peaks in April/May at R1-1 and has the highest values of all moorings except R4-1 (Figure 3.9d). In the AW it compares well with what has been measured at the latitude of R2-1 (von Appen et al., 2016), but EKE also peaks in the DW portion of the upper 800 m, with a stronger peak than any of the other moorings. Present eddies may be subjected to atmospheric forcing, or subsequent convection may cause baroclinic instability and produce new eddies (Akitomo, 2010).

3.2.2 Interannual variability

The seasonal cycle of potential temperature at R1-1 is very similar in 2016 and 2017 from January to July, but 2017 was generally warmer in August to December compared to 2016 (Figure 3.13a). The discrepancy is largest in December with almost 1°C. This is a signal most obvious in the DW portion of the upper 800 m of the water column, though of much smaller magnitude (not shown). Salinity and potential density on the other hand are fairly similar in both years in all water masses (not shown).
Velocities vary between the two years as they do throughout the year (not shown). One peak in southeastward velocity in March 2017 sticks out (but is averaged with weak velocities in March 2018). Maximum EKE occurs in April 2017, while EKE peaks in the second year in March and May 2018, only with an amplitude of about half of that in April 2017 (Figure 3.13b).

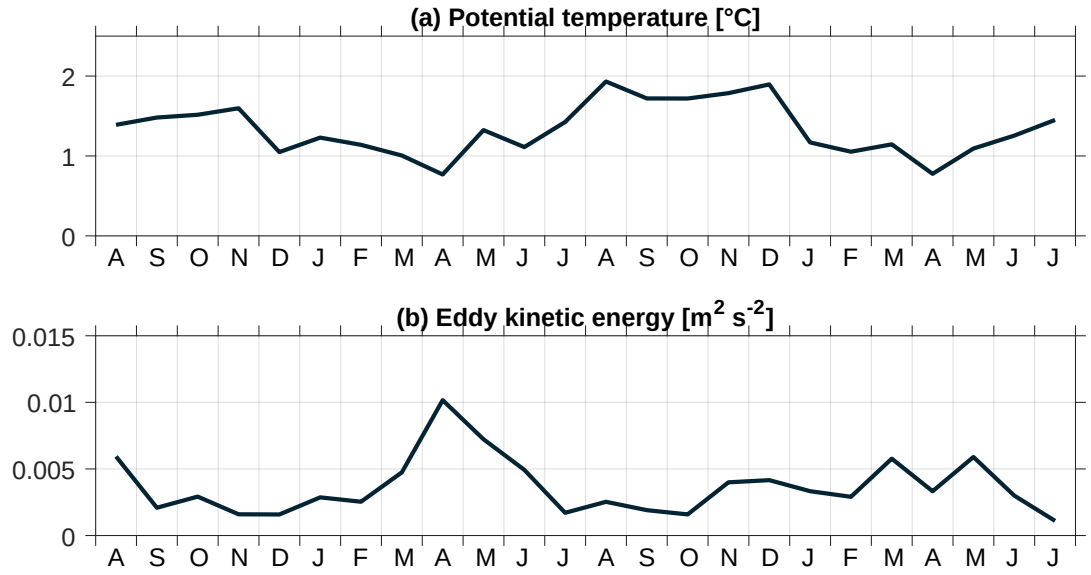

Figure 3.13: Monthly averages of (a) potential temperature (°C), and (b) eddy kinetic energy (m^2 s^{-2}) from August 2016 to July 2018 at R1-1, averaged over the upper 800 m of the water column. Note that there are no data available in the upper 40 m for potential temperature, and in the upper 20 m for eddy kinetic energy.

That means a colder summer/autumn with slightly weaker salinities and less AW

was followed by a spring of high EKE, and some deep convection, as indicated by the water mass distribution. Then comes a warmer summer/autumn with slightly higher salinities and more AW, followed by a steep drop in AW layer thickness, and a large peak in DW layer thickness, indicating strong deep convection. This is also visible in the stratification, which is lowest at R1-1 in March/April 2018. A hypothesis would be that in spring 2017 EKE is advected from the WSC towards R1-1, i.e. it is influenced by the southern recirculation, likely much more so than in 2016. In 2018 strong deep convection occurs, either because R1-1 is less affected by the southern recirculation, or because the comparatively large amount of AW present acts as a precondition for the dense water formation (as more saline water is cooled), or a combination of both.

3.3 Arctic Ocean outflow

R5-1 displays the lowest temperature and salinity throughout the year (Figures 3.7a,b), with a steady PW layer close to the surface. Velocities are generally weak and southeastward, suggesting R5-1 to be located in the Arctic Ocean outflow region, mostly unaffected by the recirculation.

3.3.1 Seasonal variability

At R5-1, the PW layer is the thickest in comparison to the other moorings, with little variation throughout the year due to the continuous ice cover. R5-1 is also the only mooring at which PW is present with more than 10% of the gridded measurements during all monthly means (see Chapter 2.4 for more information). The PW layer thickness is of comparable magnitude to the AAW layer thickness, which are the two dominant water masses in the Arctic Ocean outflow in the upper water column. At the same time, the AW layer thickness is smallest at R5-1 of all the moorings. The most notable feature is a maximum in AW layer thickness and a minimum in AAW layer thickness in April (Figure 3.8e). By our definition, on average (over the entire time series) some AAW is situated above the AW layer, and most is situated below (not shown). This may only be AW that has mixed with the PW above.
Potential temperature, salinity, and potential density are all smallest in the upper 800 m of the water column at R5-1, compared to the other moorings, which is largely due to the sizable fraction of PW (Figures 3.9a,b,c). Potential temperature is larger in February to April, with a maximum in April. This is a feature that is clearest in the AAW (Figure 3.11a). The same can be seen in salinity, meaning that in April there is not only more AW present, but also the AAW is warmer and more saline. Unless the Arctic Ocean outflow has different characteristics during this time of the year, this may be the fraction of water falling into the AAW definition that is just a local mixture between the PW and AW. Potential temperature and salinity display little variability (of similar magnitude to that of R1-1 and R2-1), with a small peak in March to April in potential temperature (Figure C.1a). Of all the water masses at R5-1, the PW generally has the largest variability in potential temperature, salinity, and potential density, with a maximum in potential temperature in March, and a maximum in salinity in October, though this is still small compared to PW variability at R3-1 and R4-1 (not shown). Only in the AAW is the variability of salinity largest at R5-1, with a maximum in October (Figure 3.11). R5-1 has the strongest

stratification of the moorings (not shown), with the only seasonality in the AAW with a maximum in October to December and a minimum in February to August. Zonal velocities are generally eastward and meridional velocities are generally southward. Both are weak and fairly barotropic (Figures 3.9e,f). This fits well with the Arctic Ocean outflow modelled by Wekerle et al. (2017), and the observations of a broad, barotropic outflow at higher latitudes by Richter et al. (2018). EKE is smallest compared to other moorings in all water masses, with no obvious seasonality (Figures 3.9d, 3.10d, 3.11d, 3.12d), further supporting that there is little to no influence of the recirculation at R5-1.

3.3.2 Interannual variability

Potential temperature and salinity peak in April of both years, with an additional peak in February during the second year (Figures 3.14a,b). The first year is colder and fresher in December to February, during which the northern recirculation is more dominant. In addition, AW is present during most months of the second year, unlike the first year, where there is only AW present in more than 10% of the measurements during March to July (Figure 2.4e). Indeed we will show below (Chapter 3.5) that the northern recirculation is much stronger during the second year, but if it were impacting R5-1, we would expect a signal in the EKE as well, which is similarly small in both years (not shown). The velocities are also very similar in the two years (not shown), supporting the idea that R5-1 is not affected by the recirculation much, but rather only by the Arctic Ocean outflow.
PW potential temperature is minimal in the first winter, but maximal in the second one (not shown). A hypothesis would be that the northern recirculation blocks the southward transport of PW at this longitude, enabling PW accumulation (see Chapter 3.6).

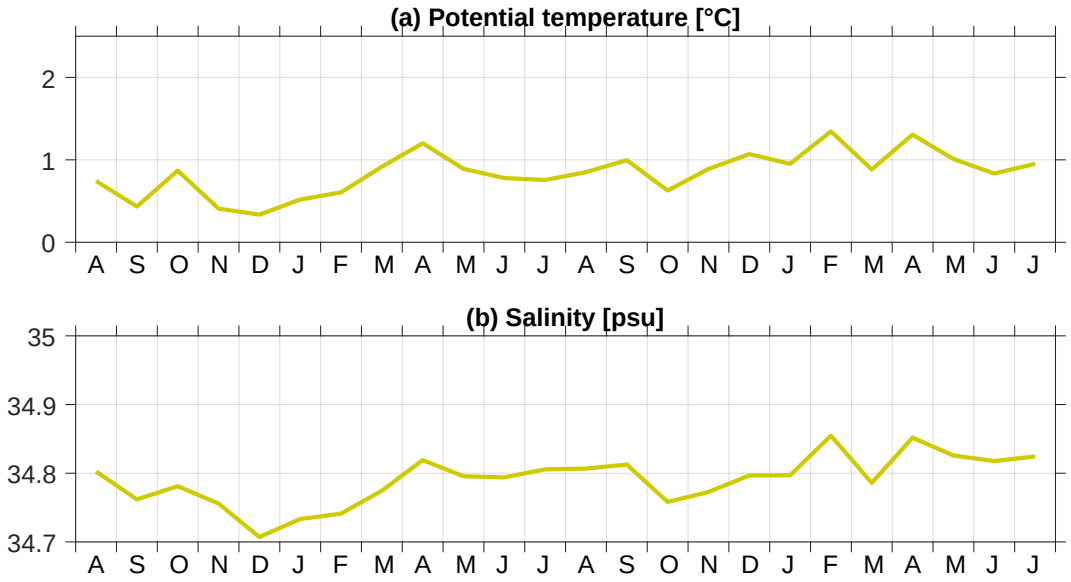

Figure 3.14: Monthly averages of (a) potential temperature (°C), and (b) salinity (psu) from August 2016 to July 2018 at R5-1, averaged over the upper 800 m of the water column. Note that there are no data available in the upper 40 m for potential temperature and salinity.

3.4 Continuous recirculation branch

At R2-1, velocities are mostly westward, at times northwestward (Figures 3.3e,f). On average, it displays the maximum potential temperature and salinity in the AW layer, which is also thickest of all the moorings (Figure 3.1). This confirms, what has been observed through the zonal array at this latitude already (Schauer et al., 2004; Beszczynska-Möller et al., 2012): there is a continuous recirculation branch present at 78°50'N.

3.4.1 Seasonal variability

PW is present in most months, though it makes up a small fraction of measurements and is, on average, only above the 10% mark from August to December (Figure 2.4b). AW layer thickness is maximal in June/July, but also peaks in January. During these months, AW makes up the largest fraction of the upper 800 m out of the four water masses considered here (Figure 3.8b). R2-1 is also the mooring that has the thickest AW layer throughout the year, and the thinnest AAW layer. Similar to R1-1, AAW layer thickness is maximal in December and minimal in May/June, while DW layer thickness peaks in April. As at R1-1, this speaks for the AAW not actually being AW that has circulated through the Arctic Ocean, but rather cooled AW that continues to become denser, though this happens less than it does at R1-1 due to the sustained influence by the AW recirculation.
The seasonal cycle of potential temperature at R2-1 is also similar to that of R1-1, with maximum values in June to November and minimum values in February to April, yet the temperatures are generally higher (Figure 3.9a). The same signal can be seen in the AW portion of the water column, though its seasonal cycle of potential temperature is slightly weaker than at R1-1 (Figure 3.10a), and reversed with a small lag in the DW (Figure 3.12a). Salinity, on the other hand, varies little throughout the year and, averaged over the entire 800 m or any water mass, is smaller than at R1-1 (Figure 3.9b), even though on average, the salinity maximum of all moorings and all depths is located at one point in the water column at R2-1. The salinity of the AW has a minimum in December to March (Figure 3.10b). Just like R1-1, the potential density mostly reflects the seasonal cycle of potential temperature and is second highest of the moorings (Figure 3.9c), like salinity. There is also little variability in potential temperature, though a slight peak in its standard deviation in April/May is visible (Figure C.1a), and there is some considerable variability in the salinity of the AW, which is largest in February (Figure C.2b). Stratification at R2-1 is weaker than at the moorings further north (not shown), with the weakest stratification in the AW layer in the first half of the year, similar to R1-1.
Zonal velocities are westward throughout the year, the strongest of all the moorings, in all water masses. They are strongest in January to July, reaching their maximum in May (Figure 3.9e). This seasonal cycle is even clearer in the AW (Figure 3.10e). This confirms, what has been observed at this latitude at the zonal mooring array since 1997 (Schauer et al., 2004; Beszczynska-Möller et al., 2012). Velocities at the zonal mooring array close to the prime meridian were generally westward, and stronger with a slight northward component in winter (Figures 3.15a,b). Our observations indicate that meridional velocities are small, southward in June to October and indeed northward in November to February. The northward velocities increase

substantially in March to May, giving the flow at R2-1 a northwestward direction (Figure 3.9f), which is also clearest in the AW (Figure 3.10f). This means, AW layer thickness is largest at R2-1 during times, when the westward velocities are strongest, but do not have the additional northward component. EKE peaks in April/May, like it does at R1-1 (Figures 3.9d, 3.17a,b). This compares very well, both in timing and magnitude, with observations made by von Appen et al. (2016) at this latitude (Figures 3.18a,b).

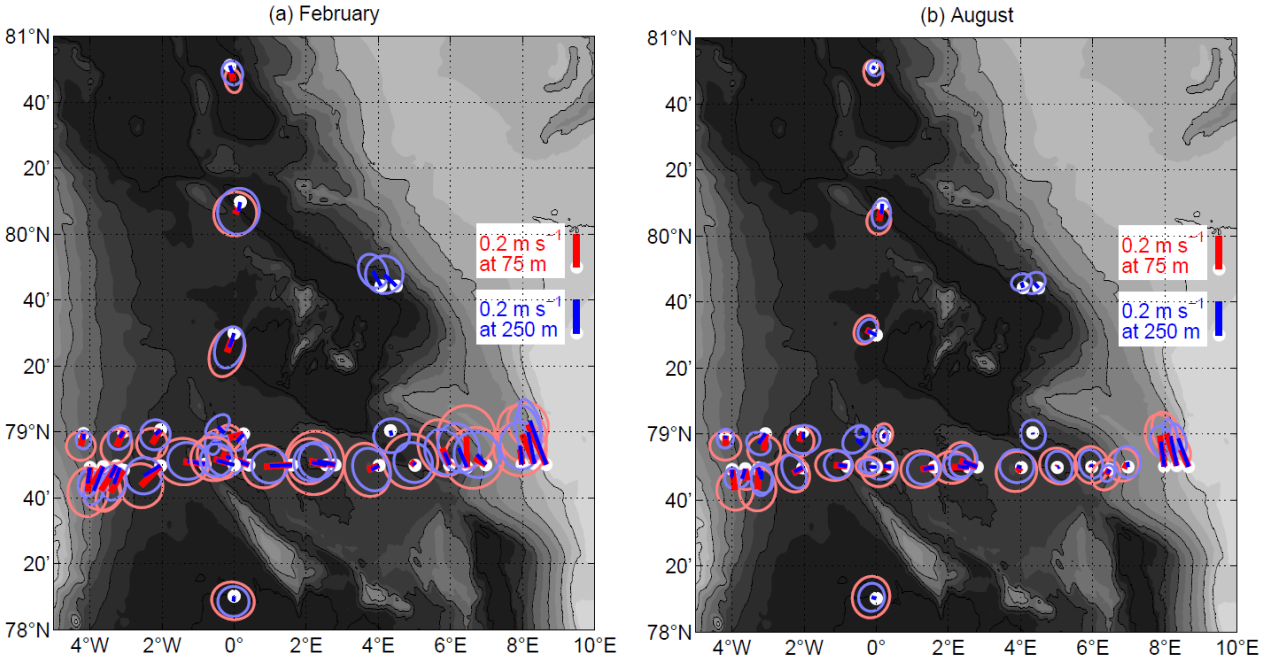

Figure 3.15: Mean velocity (m s^{-1}) and standard deviation ellipses from moored instruments in the upper water column. (a) The February mean and (b) August mean. The mooring positions are shown as thick white dots. The monthly mean currents at 75 m depth are shown as thick red lines pointing away from the mooring location. At 250 m, the lines are thinner and blue. The standard deviation ellipses around the mean are shown in light red (75 m) and light blue (250 m). Figure modified from von Appen et al. (2016).

3.4.2 Interannual variability

The seasonal cycle of potential temperature at R2-1 reaches its minimum and maximum later in 2016/17 (in May/April and October, respectively) compared to 2017/18 (February and August, respectively; not shown). Salinity and potential density, as at R1-1, are fairly similar in both years (not shown).
Unlike in the seasonal cycle of both years, the westward velocities cease in the monthly averages in August 2016, March 2017, and November 2017 (Figure 3.16a), more precisely for periods of 16–24 days. This may suggest some meandering, filamentation, or broadening/narrowing of the southern recirculation branch. The strong northward flow in March to May is clearly present in both years, but the meridional velocities vary more and are strongly southward at times during the rest of the year in 2017/18, while they are mostly weak or northward during the rest of the year in 2016/17 (Figure 3.16b). The southward velocities in October 2017 and July 2018 may suggest that at times R2-1 is located in the part of the recirculation

that joins the EGC on its southward path, i.e. the outer EGC (Håvik et al., 2017). EKE peaks a little earlier and stronger in 2016/17 (in April) compared to 2017/18 (in May), similar to EKE at R1-1, though without the peak in March 2018 (not shown). DW layer thickness peaks in April 2017, while AW layer thickness has a minimum (Figure 2.4b), very much like what happens at R1-1, though there the effect is much stronger in 2018. This might indicate that there is also convection occurring to a certain degree at R1-1.

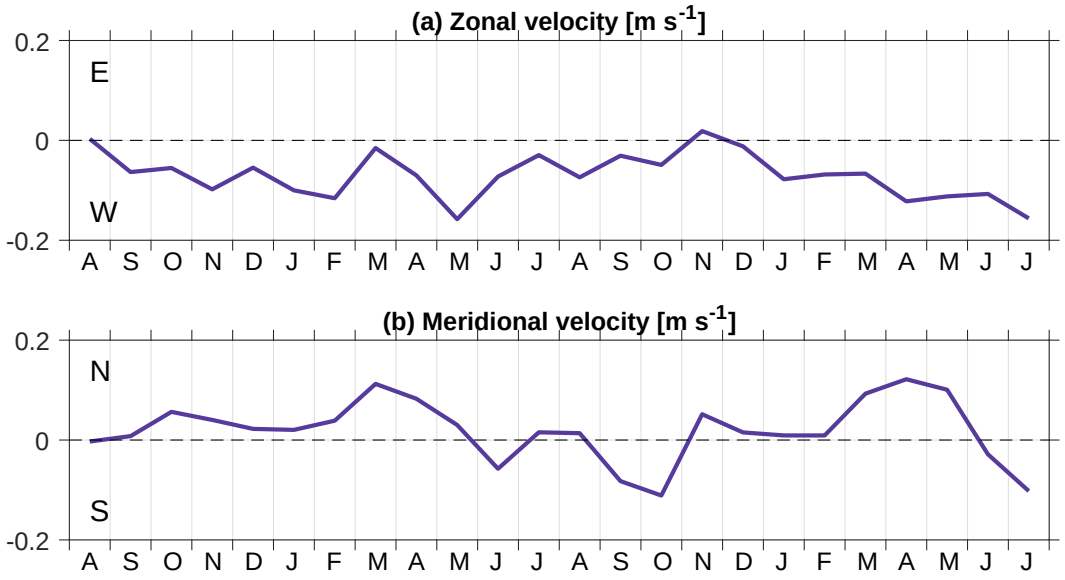

Figure 3.16: Monthly averages of (a) zonal velocity (m s^{-1}), and (b) meridional velocity (m s^{-1}) from August 2016 to July 2018 at R2-1, averaged over the upper 800 m of the water column. Note that there are no data available in the upper 20 m for zonal and meridional velocity.

3.4.3 Mesoscale variability

Eddies clearly play a role, but EKE has a seasonality that does not fully coincide with the seasonal cycle of potential temperature and salinity. Its maximum in April/May is followed by an increase in potential temperature, though this is likely influence from the warming atmosphere at this time of the year, also to be observed at R1-1. It coincides with a slight peak in salinity, the only months, during which salinity is larger at R2-1 than at R1-1. The salinity of AW actually plateaus from April to November. At the same time, zonal and meridional velocities are largest, particularly in the AW.

The question arises, how continuous the southern recirculation branch really is. It is possible that it is a separate branch of the WSC altogether that advects eddies or is even subject to instabilities itself. Such a current could meander, generate filaments, or broaden/narrow, and even though the westward velocities at R2-1 are observed most of the time, there are a few weeks during which they cease. The alternative is that the recirculation consists only of eddies that self-propagate westwards, so that on average, we observe westward velocities. The propagation speed of eddies is limited by the maximum phase speed of Rossby waves, which depends on the variation of the Coriolis parameter β and is very small at this latitude (Johannessen et al., 1983). The topographic β quantifies a similar effect of changing the background potential vorticity (PV = relative vorticity + f/H, where f

is the Coriolis parameter and H the water depth), but due to changes in topography instead of planetary vorticity, and is of several orders of magnitude larger in Fram Strait, particularly at the continental slope of Svalbard (von Appen et al., 2016). It is not clear from our observations, whether self-propagation or advection of eddies by a background flow is more likely. This may be more easily analysed in the eddy generation regions.

3.5 Eddying recirculation branch

While R4-1 has a strong PW layer during part of the year, in late autumn/winter the upper part of the water column is dominated by short periods of high temperature and salinity (Figures 3.6a,b). This, as well as the subsurface EKE maximum in the time-averaged section (Figure 3.1d) suggest this location to be impacted by a more eddying AW recirculation.

3.5.1 Seasonal variability

At R4-1 the PW layer thickness is fairly constant throughout the year, with the exception of December to February. Particularly in December the PW layer diminishes, when the AW layer thickness reaches its maximum. AW layer thickness has one of the largest seasonal cycles of all the moorings, with highest values in December to February, and a minimum in July (Figure 3.8d). AAW and DW layer thickness vary much less throughout the year, though AAW layer thickness also displays a minimum in April (like PW layer thickness).
This seasonality is well reflected in potential temperature and salinity. Potential temperature of the upper 800 m of the water column is, in fact, highest of all moorings and all months in December at R4-1 (Figure 3.9a). Between the maximum in December and the minimum in July lies a difference of about 1°C. R1-1 is the only mooring that displays a seasonal cycle of similar strength, but with a maximum in August to November and a minimum in April, which is more what would be expected from direct contact with the atmosphere. The seasonality at R4-1 is likely an advected signal, as a maximum in potential temperature and salinity would not be caused by influence from the atmosphere or sea ice in December. When salinity peaks in December, it reaches values similar to that of R1-1 and R2-1, while during the rest of the year, R4-1 is much more like R3-1 or even R5-1 (Figure 3.9b). The peak in December is also notable in potential density, right after a minimum in November (Figure 3.9c). This is a signal most noticeable in the AW portion of the water column (Figure 3.10c). Potential temperature is most variable at R4-1 out of the five moorings with several peaks in September, November, and January to March, the same goes for the variability of salinity (Figures 3.9a,b). In particular, the peak in November stands out in the AW (Figures 3.10a,b) and the PW part of the water column. As this is roughly the time of the year, when the ice edge reaches the location of R4-1 (see sea ice concentration maps from `https://www.meereisportal.de`, for data acquisition see Spreen et al., 2008), it seems likely that this variability is related either to the process of ice formation itself, or the interaction of WSC eddies with the ice edge. Stratification at R4-1 is similar to that at R3-1, stronger than at R1-1 and R2-1, but weaker than at R5-1. It has a minimum in December and is strongest in June to November (not shown), which is clearest in the AW, likely

linked to the presence of PW close to the surface.
Zonal velocity is weak, of variable direction, and barotropic (Figure 3.9e). Meridional velocity, however, is southward throughout the year and strongest of the five moorings (∼0.08 m s^{-1} on average), with the exception of the northward peak during March to May at R2-1 (Figure 3.9f). The southward velocities are weakest in the AW (Figure 3.10f), in particular during October to April, and strongest in the DW (Figure 3.12f). This seems to suggest that the recirculation contradicts the southward motion somehow, but it appears unlikely that the eddies are propagating northward against the background flow. This may be related to the northern recirculation blocking the Arctic Ocean outflow at this longitude (see Chapter 3.6).

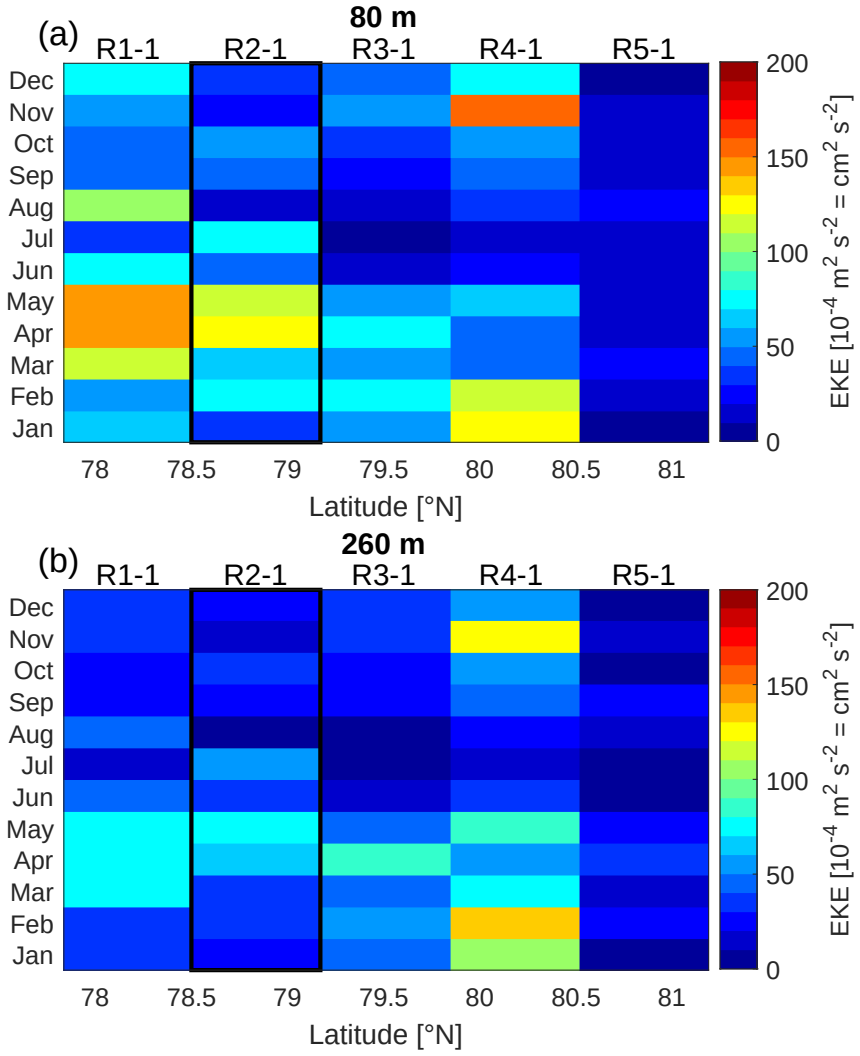

Figure 3.17: Seasonal cycle of eddy kinetic energy (10^4 m^2 s^{-2} = 1 cm^2 s^{-2}) at all five moorings, at (a) 80 m, and (b) 260 m depth for better comparison with von Appen et al. (2016). R2-1, marked with a black box, is the mooring located at the same latitude as the zonal mooring array, on which Figure 3.18 from von Appen et al. (2016) is based on.

The seasonal cycle of EKE is very unique at R4-1. While EKE at all other moorings except R5-1 (where EKE is small and displays almost no seasonal variability) peaks in April/May, it peaks in November and in January/February at R4-1 (Figure 3.9d). Both peaks are stronger than at any other moorings of the recirculation (Figures 3.17a,b). A third peak in May is slightly smaller than that of the other moorings.

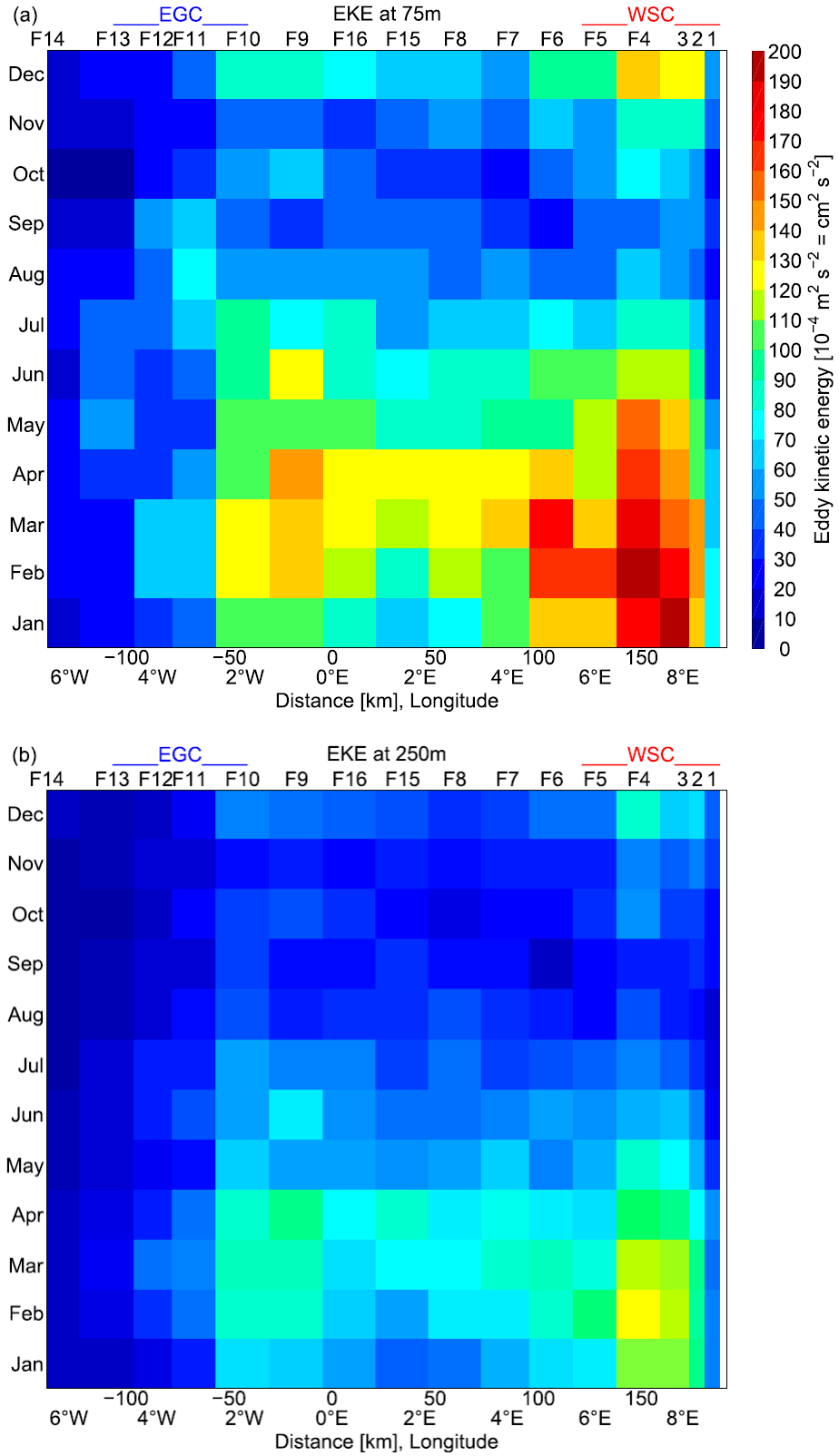

Figure 3.18: Seasonal cycle of the eddy kinetic energy (10^4 m^2 s^{-2} = 1 cm^2 s^{-2}) at (a) 75 m depth and (b) 250 m depth as a function of zonal distance across Fram Strait. The approximate locations of the WSC and the EGC are marked at the top. The EKE is defined as in this thesis. Figure from von Appen et al. (2016).

This is clearest in the AW (Figure 3.10d), but also noticeable in the AAW (Figure 3.11d). The peak in November, just as the variability in temperature and salinity, may be linked to the ice cover, as will be further discussed below with regard to mesoscale variability. The peak in January/February may be explained by the fact that R4-1 is located much closer to the WSC than the moorings further south. However, when comparing the EKE at R4-1 with a mooring at 78°50'N in similar proximity to the WSC, the maximum is still occurs earlier, essentially it occurs at the same time as it does in the WSC (Figures 3.18a,b). Since we do not know, if the WSC behaves the same way at 80°10'N and 78°50'N, we may hypothesise that further north different dynamics are at play in the formation of eddies.

3.5.2 Interannual variability

There is little difference in potential temperature between the two years, but salinity and potential density are smaller during the first year in January to May (Figure 3.19a). Also the EKE maxima are about three times larger (in November and February) during the second year (Figure 3.19b). During the first year there is less AW present that barely varies in salinity, whereas during the second year more AW with a strong seasonality in potential temperature and salinity is present (not shown). During the latter PW almost vanishes. This means, during the second year the northern recirculation is much stronger.
There is one exception: in October 2016 both potential temperature and salinity peak (Figure 3.19a), reaching values almost as large as the maximum in December. At the same time, the southward velocity almost vanishes and there is some westward motion (not shown). It may be possible that this is the only time in our observations, during which R4-1 is not located in the southward Arctic Ocean outflow, but captures some of the direct recirculation.

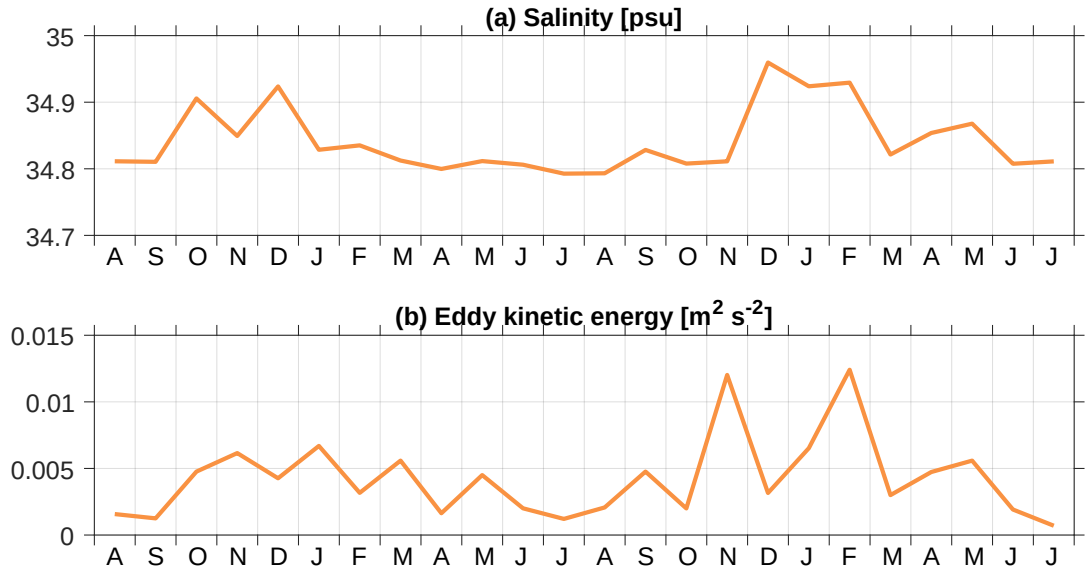

Figure 3.19: Monthly averages of (a) salinity (psu), and (b) eddy kinetic energy (m^2 s^{-2}) from August 2016 to July 2018 at R4-1, averaged over the upper 800 m of the water column. Note that there are no data available in the upper 40 m for salinity, and in the upper 20 m for eddy kinetic energy.

3.5.3 Mesoscale variability

Ideally, we would like to not only be able to observe that mesoscale variability plays a role, which we can do by calculating EKE from velocity observations, but quantify eddies in some way. Our data set is limited in that regard, since the moorings have a distance of ∼75 km in between them, yet the internal Rossby radius of deformation governing the horizontal scale of eddies at this latitude is only ∼2–6 km (von Appen et al., 2016; Zhao et al., 2014). Hence there are very little options, in which we could directly observe an eddy and know that we are looking at one. Under certain circumstance this has been done (Lilly et al., 2003), which do not seem to be applicable in our case. But we do observe a lot of variability in the velocities and if we assume it is caused by eddies, strong velocities on mesoscale time scales in any direction can be an indicator for eddies, depending on which side of the eddy we observe. Hence we define eastward and westward spells in the zonal velocity (how this was done can be found in Chapter 2.6). Meridional velocity is dominated by southward flow, likely of the Arctic Ocean outflow, and is not analysed in this way for the time being, which means we certainly missed eddies. But analysing the zonal velocity for spells can give us an idea about the length, frequency, and strength of these spells nonetheless.

An example of both an eastward spell (Figures 3.20a,c) and a westward spell (Figures 3.20b,d) illustrates their subsurface zonal velocity and EKE maximum. Maximum velocities in some spells can reach up to 0.5 m s^{-1}, maximum EKE up to 0.13 m^2 s^{-2}. 48 westward spells and 55 eastward spells were identified. Only spells that exceed an average westward/eastward velocity of 0.05 m s^{-1} are used in the analysis, and since westward spells are generally stronger (with an average westward velocity of -0.09 m s^{-1}) than eastward spells (with an average eastward velocity of 0.06 m s^{-1}), this leaves 44 westward spells and 34 eastward spells (Figure 3.20e). Both westward and eastward spells last on average about 3 days. Most spells occur in December 2017 to February 2018, and most of them are westward (Figure 3.20e). Whether we capture the southern or northern end of the eddies more often is impossible to determine, since they could be either cyclonic or anticyclonic. One possibility would be to analyse the spells' temperature and salinity anomalies, which could reveal cold or warm cores potentially associated with (anti-)cyclones. The spells' EKE is largest from November to February in both years (Figure 3.20e).

R4-1 is located directly on the Molloy FZ, as one hypothesis is that the eddying recirculation is topographically guided along fracture zones (Quadfasel et al., 1987). During the 1983 and 1984 Marginal Ice Zone Experiments, several mesoscale eddies were studied in the Fram Strait between 78° and 81°, which had a (mostly subsurface) maximum velocity of up to 0.4 m s^{-1} (Johannessen et al., 1987). This compares well with maximum velocities of our velocity spells. The eddies observed by Johannessen et al. (1987) had typical scales of 20–40 km and were mainly cyclonic. They propose different generation mechanisms for these eddies — some are formed by a mixture of these mechanisms, or by one single mechanism. Barotropic and baroclinic instability in the WSC likely play a role, and the WSC has since been found to be barotropically and baroclinically unstable at least sometimes (Teigen et al., 2010, 2011). More specifically, baroclinic instability plays a larger role in generating eddies, especially during winter, while barotropic instability plays some role during winter in regions, where the topography supports it (von Appen et al., 2016). Topographically controlled eddies are formed by conservation of PV, when

barotropic flow interacts with bathymetry (Johannessen et al., 1987, i.e. when flow crosses f/H contours, and relative vorticity has to increase/decrease). Since the WSC responds very strongly to f/H contours, this is more likely in regions, were the topography is very complicated, for example when fracture zones hit the continental slope (Gascard et al., 1988). Another factor that can affect eddy generation and strength is the PW and sea ice in the western part of Fram Strait. In regions, where the AW has to subduct underneath the lighter PW and the ice, a deepening of the AW core may enhance potential vorticity of the upper water layer, i.e. the isopycnal bounding the AW on the lower end of the water layer has a larger distance to the surface, and relative vorticity must increase for PV conservation (Johannessen et al., 1987).

While our findings of EKE at R1-1, R2-1, and R3-1 compare favourably with the findings of von Appen et al. (2016) at the zonal array, it seems likely that, as suggested in their analysis, barotropic and mostly baroclinic instability cause the EKE maximum in April/May (Figures 3.17a,b). The situation at R4-1 seems more complicated and is probably affected by the close proximity of the ice edge during most of the year (Figure 3.4), as well as a more complex topography due to the Molloy Hole.

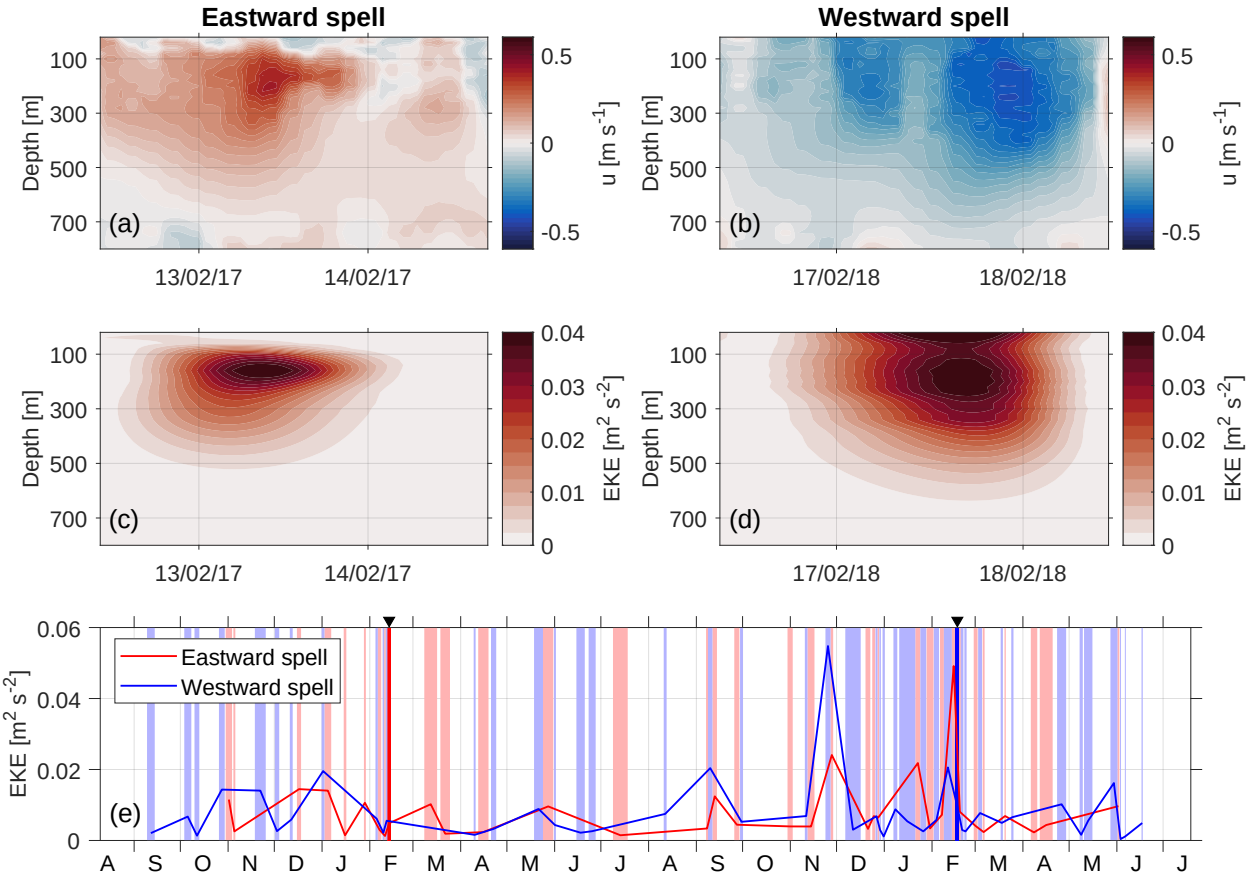

Figure 3.20: Zonal velocity (m s^{-1}) section of an example of (a) an eastward spell, and (b) a westward spell, as well as eddy kinetic energy (m^2 s^{-2}) during the same time ((c) and (d), respectively). (e) Time series of depth-averaged eddy kinetic energy (m^2 s^{-2}) of all eastward (red) and westward (blue) spells. Each spell is marked in its full duration in light shading; the example spells from (a) and (b) are marked in darker shading. For the definition of eastward/westward spells see Chapter 2.

3.6 Influence by southern/northern recirculation

From the Hovmöller diagram (Figure 3.5) it is not quite clear, whether R3-1 is more influenced by the southern or the northern recirculation branch. It is likely not directly affected by the WSC due to its location west of the Molloy Hole.

3.6.1 Seasonal variability

The PW layer thickness is maximal in July to November and minimal in December and April. AW layer thickness opposes these minima with peaks in December and April, the latter being the larger one. AAW and DW layer thickness does not vary much throughout the year (Figure 3.8c).
Unlike further south, potential temperature does not display a strong seasonal cycle in the upper 800 m of the water column, except for a peak in April that is also visible in salinity (Figures 3.9a,b). Salinity additionally peaks in December to February, just like at R4-1. It seems likely that R3-1 is affected by the southern recirculation, when it gains its northward component, and by the northern recirculation, when it takes maximal effect. The AW at R3-1 has the lowest salinity of the moorings, maybe because it takes the longest route towards the prime meridian. It has a similar potential temperature as at R4-1, and almost no seasonal cycle (Figures 3.10a,b) — the seasonal cycle in the upper 800 m of the water column stems from the amount of AW present, not the variability within the water mass. This indicates that the two recirculation branches are not so different, if they do indeed impact R3-1 at different times, but with no discernible difference in the AW properties. It is possible, however, that the signal from the northern recirculation branch is diluted by the Arctic Ocean outflow. The potential density is very similar to that at R4-1, with a peak in December, right after a minimum in November (Figure 3.9c). The standard deviation of potential temperature and salinity is higher than at R1-1, R2-1, and R5-1, but smaller than that at R4-1, with less variation in between months (Figures C.1a,b). The standard deviation of salinity in the AW is even larger than that at R4-1 at times (Figure C.2b). R3-1 displays the strongest stratification in November and the weakest right afterwards in December, very similar to R4-1 (not shown).
Zonal velocities are weak, of variable direction, and barotropic, also similar to R4-1 (Figure 3.9e). Meridional velocities are stronger and southward in November and January to March, but otherwise also weak and of variable direction (Figure 3.9f). The signal is slightly stronger in the AW layer, in contrast to R4-1 (Figure 3.10f). EKE is maximal in April/May, similar to R1-1 and R2-1, but of smaller magnitude (Figure 3.9d). This varies much less in the different water masses than at the other moorings, where in particular in the AW the EKE is much larger than on average in the upper 800 m of the water column (Figure 3.10d).

3.6.2 Interannual variability

Potential temperature and EKE clearly peak in April 2017, but not in April 2018 (Figures 3.21a,b). This peak is also very notable in AW salinity (not shown). At first, southward velocities dominate the flow, which then cease in April 2017 (not shown). It seems, R3-1 is reached by the Arctic Ocean outflow in the beginning of

the observational period, which is then suppressed by the influence from the southern recirculation. This is not the case in 2018, meaning the northward meridional velocities at R2-1 may not be the cause for the southern recirculation impacting R3-1, because these are observed in both years.
During March 2018, there are strong eastward velocities at R3-1, a signal visible in all water masses, though it is not clear as to why these occur. In the first year, there are more months, during which there were more than 10% of observations that fall into the PW definition, similar to R4-1. This is when there is less eddy activity (i.e. less recirculation) at R4-1, so that the PW layer is much more continuous from north to south.
One possible conclusion is that R3-1 is located in the Arctic Ocean outflow unless it is influenced by the southern or northern recirculation. The former seems to be the case only in the first year (which is also the case at R1-1, which would mean the southern recirculation must have become very broad, or the signal from the WSC was very strong in that year). The effect of the northern recirculation may actually be one of simply impeding PW transport from the north rather than directly influencing R3-1.

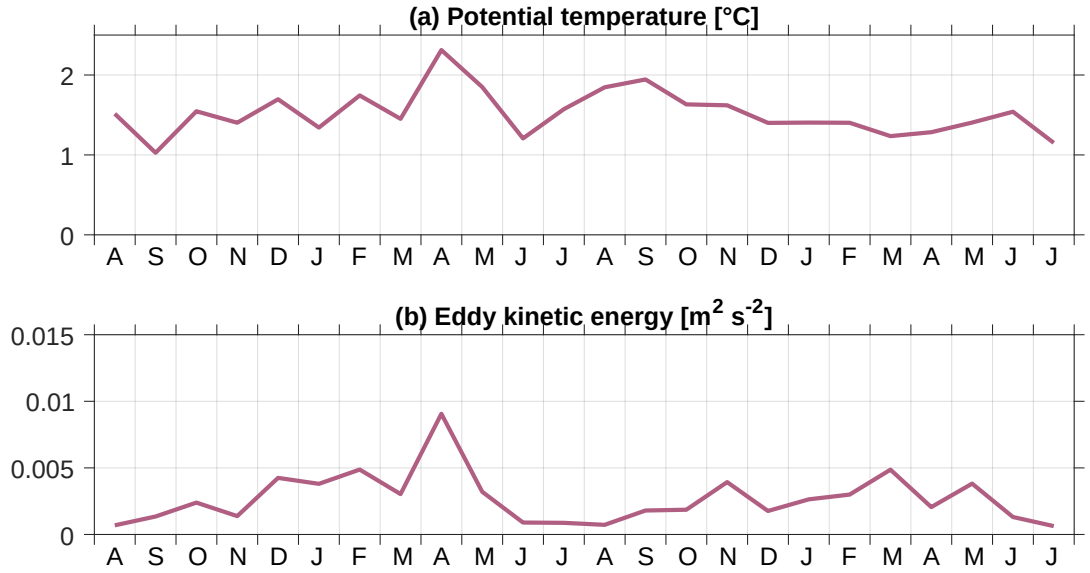

Figure 3.21: Monthly averages of (a) potential temperature (°C), and (b) eddy kinetic energy (m^2 s^{-2}) from August 2016 to July 2018 at R3-1, averaged over the upper 800 m of the water column. Note that there are no data available in the upper 40 m for potential temperature, and in the upper 20 m for eddy kinetic energy.

3.6.3 Mesoscale variability

The impact of mesoscale variability at R4-1 becomes visible in the first empirical orthogonal function (EOF) of potential temperature. There are times, during which maximum potential temperature is located at R4-1 and the high temperatures reach up high in the water column (Figure 3.22b), and times, during which there is much less warm AW at R4-1 and the cold surface PW layer is well established (Figure 3.22c). This also leads to a stronger surface PW layer at R3-1, though it is not as thick as it is at R4-1 and R5-1. These two situations represent the northern recirculation branch being present (Figure 3.22b) or absent (Figure 3.22c). The first

principal component (PC) indicates that it is present from September/October until March, with high frequency variability in the first PC, highlighting the importance of mesoscale variability (Figure 3.22d). The first PC is mostly positive in December 2017 to February 2018, which is when the northern recirculation branch is strongest. During this time it seems that the northern recirculation has a 'blocking' effect on the PW transport from the north. This is not to be confused with the recirculation blocking the flow, but rather affecting the properties of the Arctic Ocean outflow.

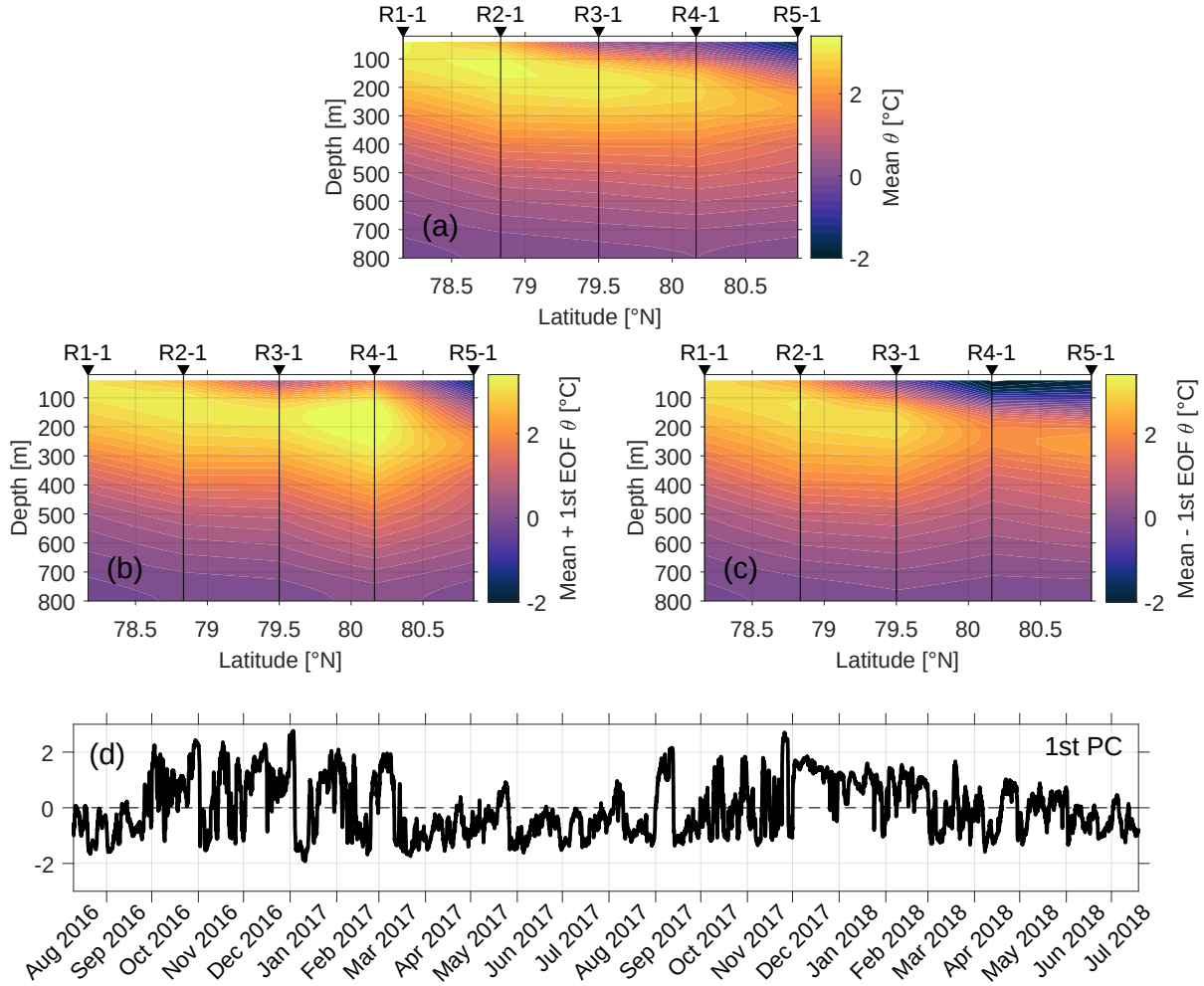

Figure 3.22: (a) Gridded potential temperature (°C) section, averaged over the entire time series. (b) As in (a), plus the first empirical orthogonal function (EOF) of potential temperature, and (c) as in (a), minus the first EOF. The first EOF explains 27.17% of the variance. (d) Time series of the first principal component (PC) of potential temperature.

Model output from Wekerle et al. (2017) suggests that during winter, when the northern recirculation branch is present, the Arctic Ocean outflow is broader and only narrows significantly at ∼78°30'N (Figures 3.23a,c), whereas during summer it meanders between 79°50'N and 81°40'N and narrows immediately further south (Figures 3.23b,d). With regard to the R moorings' positions, this means R3-1 is affected by the southward velocities of the Arctic Ocean outflow much more strongly in winter. It seems likely that more AW is advected from the north to the south between the locations of R5-1 and R3-1, both due to the effect of the northern recirculation on the flow pattern and the distribution of water masses.

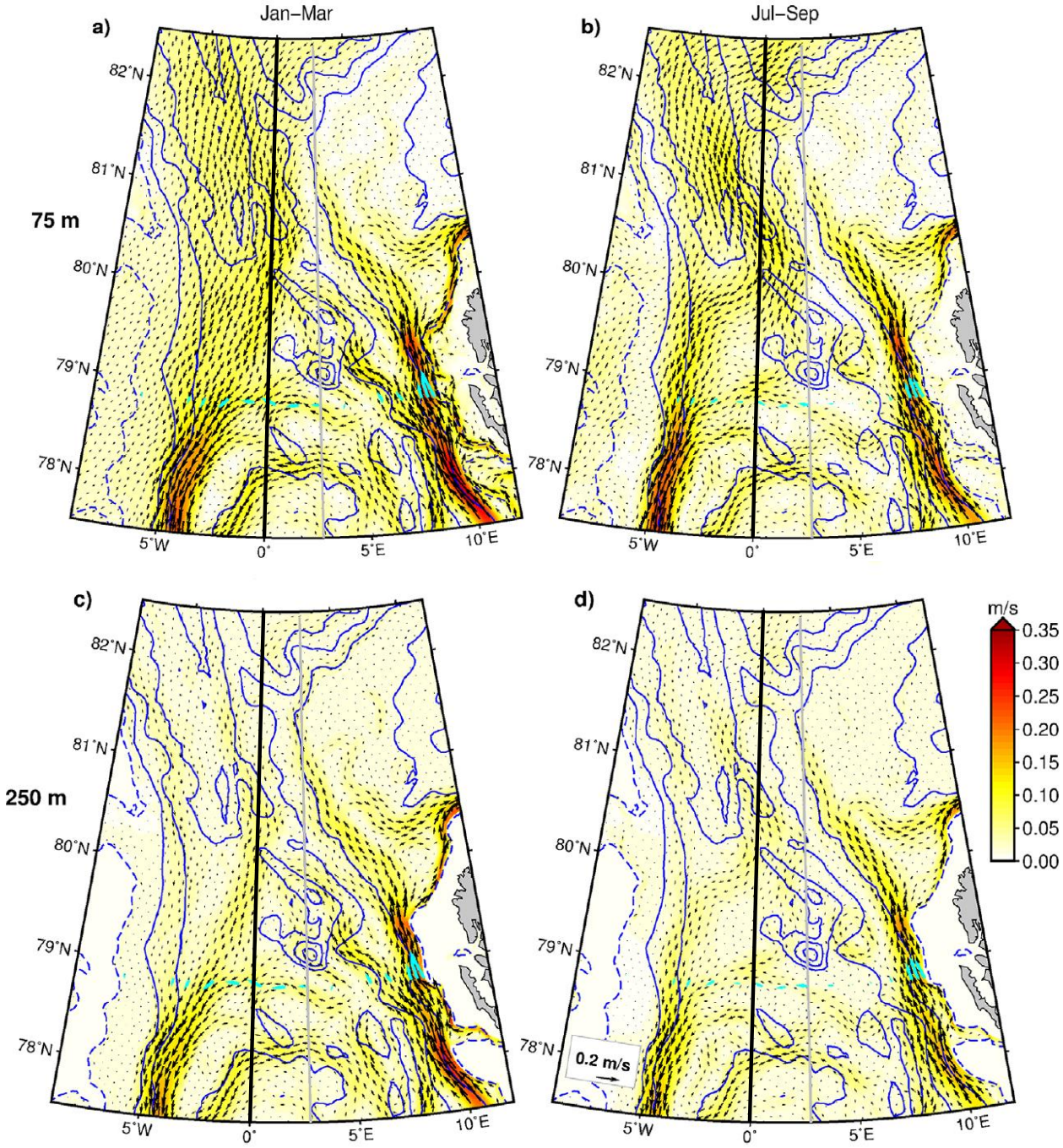

Figure 3.23: Velocity from simulation FESOM_1km during January to March in (a) 75 m and (b) 250 m depth, and during July to September in (c) 75 m and (d) 250 m depth. Cyan vectors show mean currents from mooring measurements for the same time periods (von Appen et al., 2016). Blue solid lines show the bathymetry at 1000 m intervals, and the blue dashed line shows the 250 m isobath. The black line marks the 0° line, on which the R moorings are located, the grey line indicates a cross-section not shown here. Figure modified from Wekerle et al. (2017).

Indeed, southward velocities are measured at R3-1 in November and January to March (Figure 3.9f). The difference between winter and summer is also obvious, when comparing the February and August average velocities at 75 and 250 m depth (Figures 3.15a,b). However, when looking at the two years individually, southward velocities are only present in January to March during the first year and in November during the second year, even though we would expect the impact of the northern recirculation on the flow pattern to be more obvious in the second year, when the northern recirculation is stronger.

Chapter 4

Summary and Conclusions

With the present analysis, our aim was to answer the following questions:

1. Where does the recirculation occur?

2. How variable is the recirculation in terms of location, strength, and properties?

We can identify two recirculation branches that display variability on different time scales.
We observe westward motion and a strong AW signal at the location of R2-1 (78°50'N, in between the Hovgaard Ridge and the Spitsbergen Fracture Zone). This confirms previous observations of a southern recirculation branch at this latitude (Schauer et al., 2004; Beszczynska-Möller et al., 2012). The flow does seem to meander or broaden/narrow to a certain degree around the location of R2-1, as it affects both the locations of R1-1 further south (78°10'N) and R3-1 further north (79°30'N) at times. Our analysis strongly indicates that this is a continuous phenomenon that likely never completely disappears.
We also observe a strong AW signal at R4-1 (80°10'N, on the Molloy Fracture Zone), though measurements of velocity at this location are, on average, southward and indicate the mooring to be located in the Arctic Ocean outflow, but largely affected by a northern recirculation branch.
We observe no recirculation at the northernmost mooring R5-1 (80°50'N, west of the Yermak Plateau), and very little AW, which probably means, the bulk of the recirculation occurs south of this location.
The southern recirculation branch displays little variability in its potential temperature, salinity, and amount of AW present. The flow instead varies seasonally in strength, with stronger westward flow from January to July and a maximum in May. The flow gains a strong, additional northward component during March to May. Like von Appen et al. (2016), we observe an EKE maximum in the central Fram Strait at 78°50'N in April/May. It is not clear, whether this is related to a current advecting eddies from the WSC or self-propagating eddies with an average westward direction.
The northern recirculation branch, on the other hand, is characterised not by its flow direction, but by its high variability in potential temperature, salinity, and velocities. It has a strong seasonality in the sense that it is only present during wintertime, with a maximum in potential temperature and salinity in December to February. Its seasonality of EKE is very different to that of the other moorings,

with the largest maxima in November and January/February. Mesoscale variability seems to play an important role and may be affected not only by dynamics related to the WSC, but also the ice edge.
On average, there is a PW layer present close to the surface at the prime meridian that gradually becomes thicker from south to north. However, during the part of the year when the northern recirculation branch is present, this PW layer diminishes and the upper part of the water column is almost completely occupied by AW at the location of R4-1, also significantly impacting the amount of PW further south. Since R4-1 is affected by the southward velocities of the Arctic Ocean outflow, recirculated AW is likely also transported southward at the prime meridian at times. Hence, R3-1 is affected both by the northern and southern recirculation. While the amount of AW at R3-1 varies, AW properties display very little variability, indicating that the two recirculation branches are not very different in their AW properties. It is possible though that the northern recirculation at this longitude has already mixed with the Arctic Ocean outflow.
In addition to both displaying seasonal and mesoscale variability, the two recirculation branches also vary from the first to the second year of observations. While the southern recirculation seems to affect the locations north and south of it more strongly during the first year, the northern recirculation is much stronger during the second year. Our observational period is unfortunately too short, to make further observations on interannual variability. The existence of two recirculation branches, one north and one south of the Molloy Hole, that largely follow topographic fracture zones, has been suggested by synoptic observations numerous times (Quadfasel et al., 1987; Bourke et al., 1988; Gascard et al., 1988, 1995; Rudels et al., 2005; Richter et al., 2018). Now we can confirm their existence with long-term measurements, quantify their location and discuss their properties and variability. Our findings compare reasonably well with recent modelling studies on the recirculation. Both the northern and southern recirculation branch, as we observe them, were modelled by Wekerle et al. (2017). It seems, their model picks up on the seasonality in strength of the southern recirculation, and they also find the northern recirculation to be much stronger during winter and more eddying. They find two more recirculation branches, one north of our study area, and one close to the location of our southernmost mooring R1-1. We do not observe the latter, which may rather be part of the Greenland Sea circulation than a recirculation branch originating from the WSC. Hattermann et al. (2016) also find two recirculation branches in their model. While the northern recirculation compares well with our observations, their southern recirculation occurs further south and carries colder, fresher water. It could be related to the Greenland Sea circulation, similar as the southernmost recirculation branch in Wekerle et al. (2017).
The R moorings were placed with the hypothesis to definitively delineate the location of the recirculation (Kanzow, 2017), so it is no coincidence that we were able to observe the two recirculation branches, as well as the situation outside/at the borders of the recirculation domain. With the knowledge we have now, it would be pertinent to place future moorings such that we could narrow down the location and width of the recirculation branches, i.e. further south than R5-1, and further north than R1-1. Leaving R2-1 and R4-1 in place would be beneficial for the evaluation of interannual variability and better comparison with previous observations at these locations, since we know that we can observe the recirculation with these moorings.

With regard to the southern recirculation, it would be interesting to place moorings north and south of it, with a smaller distance than previously, to further quantify the width of the recirculation and the amount of meandering or broadening/narrowing it is subjected to. At the northern recirculation, on the other hand, moorings located in close proximity (ideally smaller than the Rossby radius of deformation) east or west of R4-1 could give a better idea of eddy dynamics. Knowing the situation in the WSC at a similar latitude as R4-1 or slightly further south could also contribute to a better understanding of eddy generation processes (basically conducting a study similar to von Appen et al. (2016), but further north). As there is data available from the zonal array during the same time, the R moorings were in the water, it would be possible to analyse, whether variability at R1-1, R2-1, and R3-1 originates from the WSC. Data from the moorings in central Fram Strait from the zonal array could also be used to get a better idea of seasonal and especially interannual variability.
There is more potential in the data presented in this thesis itself: CTDs on the R moorings measured oxygen as well, analysis of which could help differentiating between AW and AAW better. Averaging over shorter time periods (than monthly means) could reveal more insight to mesoscale variability. If there is the indication of the situation at one mooring affecting the situation at another, lead-lag correlation may be a helpful tool.
To get a broader view, one could utilise models such as the FESOM model. It can provide the information that is missing from our limited mooring array: what happens in between the moorings and in the boundary currents during the same time. It gives us the ability to identify phenomena on much smaller spatial scales such as mesoscale eddies. In return, our observations can help to validate and improve the modelling of the recirculation in Fram Strait.
In conclusion, at the prime meridian we observe a more continuous recirculation branch south of the Molloy Hole and a more eddying recirculation branch north of the Molloy Hole, both with distinct seasonal and mesoscale variability. These observations can help to provide context for past and future synoptic observations, modelling representation, and dynamical understanding of the AW recirculation in Fram Strait.

Acknowledgements

Support for this study was provided by the Helmholtz Infrastructure Initiative FRAM. Ship time was provided under Grant No. AWI_PS100_01 and AWI_PS114_01. Data are available on PANGAEA (see von Appen, 2019a).
I would like to thank Dr. Wilken-Jon von Appen for the mindful and thorough supervision — I learned a lot. Thank you for your support.

References

Aagaard, K., and L. K. Coachman, 1968a: The East Greenland Current North of Denmark Strait: Part I. *Arctic*, **21**, 181–199.

Aagaard, K., and L. K. Coachman, 1968b: The East Greenland Current North of Denmark Strait: Part II. *Arctic*, **21**, 267–290.

Aagaard, K., L. K. Coachman, and E. Carmack, 1981: On the halocline of the Arctic Ocean. *Deep-Sea Research*, **28A (6)**, 529–545, doi:10.1016/0198-0149(81)90115-1.

Aagaard, K., C. Darnall, and P. Greisman, 1973: Year-long current measurements in the Greenland-Spitsbergen passage. *Deep-Sea Research*, **20**, 743–746, doi:10.1016/0011-7471(73)90090-9.

Aagaard, K., E. Fahrbach, J. Meincke, and J. H. Swift, 1991: Saline Outflow From the Arctic Ocean: Its Contribution to the Deep Waters of the Greenland, Norwegian, and Iceland Seas. *Journal of Geophysical Research*, **96 (C11)**, 20 433–20 441, doi:10.1029/91jc02013.

Aagaard, K., A. Foldvik, and S. R. Hillman, 1987: The West Spitsbergen Current: Disposition and Water Mass Transformation. *Journal of Geophysical Research: Oceans*, **92 (C4)**, 3778–3784, doi:10.1029/JC092iC04p03778.

Aagaard, K., J. H. Swift, and E. C. Carmack, 1985: Thermohaline Circulation in the Arctic Mediterranean Seas. *Journal of Geophysical Research*, **90 (C3)**, 4833, doi:10.1029/jc090ic03p04833.

Akimova, A., U. Schauer, S. Danilov, and I. Núñez-Riboni, 2011: The role of the deep mixing in the Storfjorden shelf water plume. *Deep-Sea Research Part I*, **58**, 403–414, doi:10.1016/j.dsr.2011.02.001.

Akitomo, K., 2010: Baroclinic instability and submesoscale eddy formation in weakly stratified oceans under cooling. *Journal of Geophysical Research: Oceans*, **115**, doi:10.1029/2010JC006125.

Aksenov, Y., S. Bacon, A. C. Coward, and N. P. Holliday, 2010: Polar outflow from the Arctic Ocean: A high resolution model study. *Journal of Marine Systems*, **83**, 14–37, doi:10.1016/j.jmarsys.2010.06.007.

Beszczynska-Möller, A., E. Fahrbach, U. Schauer, and E. Hansen, 2012: Variability in Atlantic water temperature and transport at the entrance to the Arctic Ocean, 1997 - 2010. *ICES Journal of Marine Science*, **69 (5)**, 852–863, doi:10.1038/278097a0.

Bourke, R. H., J. L. Newton, R. G. Paquette, and M. D. Tunnicliffe, 1987: Circulation and Water Masses of the East Greenland Shelf. *Journal of Geophysical Research*, **92 (C7)**, 6729–6740, doi:10.1029/JC092iC07p06729.

Bourke, R. H., A. M. Weigel, and R. G. Paquette, 1988: The Westward Turning Branch of the West Spitsbergen Current. *Journal of Geophysical Research*, **93 (C11)**, 14 065–14 077, doi:10.1029/jc093ic11p14065.

Brakstad, A., K. Våge, L. Håvik, and G. W. MOORE, 2019: Water Mass Transformation in the Greenland Sea during the Period 1986-2016. *Journal of Physical Oceanography*, **49**, 121–140, doi:10.1175/JPO-D-17-0273.1.

Caesar, L., S. Rahmstorf, A. Robinson, G. Feulner, and V. Saba, 2018: Observed fingerprint of a weakening Atlantic Ocean overturning circulation. *Nature*, **556**, 191–196, doi:10.1038/s41586-018-0006-5.

Cheng, W., J. C. H. Chiang, and D. Zhang, 2013: Atlantic Meridional Overturning Circulation (AMOC) in CMIP5 Models: RCP and Historical Simulations. *Journal of Climate*, **26**, 7187–7197, doi:10.1175/JCLI-D-12-00496.1.

Crews, L., A. Sundfjord, and T. Hattermann, 2019: How the Yermak Pass Branch Regulates Atlantic Water Inflow to the Arctic Ocean. *Journal of Geophysical Research: Oceans*, **124**, 267–280, doi:10.1029/2018JC014476.

de Steur, L., E. Hansen, C. Mauritzen, A. Beszczynska-Möller, and E. Fahrbach, 2014: Impact of recirculation on the East Greenland Current in Fram Strait: Results from moored current meter measurements between 1997 and 2009. *Deep-Sea Research Part I*, **92**, 26–40, doi:10.1016/j.dsr.2014.05.018.

Fahrbach, E., J. Meincke, S. Østerhus, G. Rohardt, U. Schauer, V. Tverberg, and J. Verduin, 2001: Direct measurements of volume transports through Fram Strait. *Polar Research*, **20 (2)**, 217–224, doi:10.1111/j.1751-8369.2001.tb00059.x.

Falck, E., G. Kattner, and G. Budéus, 2005: Disappearance of Pacific Water in the northwestern Fram Strait. *Geophysical Research Letters*, **32 (14)**, doi:10.1029/2005GL023400.

Fer, I., M. Müller, and A. K. Peterson, 2015: Tidal forcing, energetics, and mixing near the Yermak Plateau. *Ocean Science*, **11**, 287–304, doi:10.5194/os-11-287-2015.

Fieg, K., R. Gerdes, E. Fahrbach, A. Beszczynska-Möller, and U. Schauer, 2010: Simulation of oceanic volume transports through Fram Strait 1995-2005. *Ocean Dynamics*, **60**, 491–502, doi:10.1007/s10236-010-0263-9.

Foldvik, A., K. Aagaard, and T. Tørrese, 1988: On the velocity field of the East Greenland Current. *Deep-Sea Research*, **35 (8)**, 1335–1354, doi:10.1016/0198-0149(88)90086-6.

Gascard, J.-C., C. Kergomard, P.-F. Jeannin, and M. Fily, 1988: Diagnostic Study of the Fram Strait Marginal Ice Zone During Summer From 1983 and 1984 Marginal Ice Zone Experiment Lagrangian Observations. *Journal of Geophysical Research*, **93 (C4)**, 3613–3641, doi:10.1029/jc093ic04p03613.

Gascard, J.-C., C. Richez, and C. Rouault, 1995: New Insights on Large-Scale Oceanography in Fram Strait: The West Spitsbergen Current. *Coastal and Estuarine Studies*, **49**, 131–182.

Hansen, B., and S. Østerhus, 2000: North Atlantic – Nordic Seas exchanges. *Progress in Oceanography*, **45**, 109–208, doi:10.1111/j.1751-8369.2001.tb00053.x.

Hanzlick, D. J., 1983: The West Spitsbergen Current: Transport, Forcing, and Variability. Phd thesis, University of Washington.

Harden, B. E., and Coauthors, 2016: Upstream sources of the Denmark Strait Over flow : Observations from a high-resolution mooring array. *Deep-Sea Research Part I*, **112**, 94–112, doi:10.1016/j.dsr.2016.02.007, URL http://dx.doi.org/10.1016/j.dsr.2016.02.007.

Hattermann, T., P. E. Isachsen, W.-J. von Appen, J. Albretsen, and A. Sundfjord, 2016: Eddy-driven recirculation of Atlantic Water in Fram Strait. *Geophysical Research Letters*, **43 (7)**, 3406–3414, doi:10.1002/2016GL068323.

Håvik, L., R. S. Pickart, K. Våge, D. J. Torres, A. M. Thurnherr, A. Beszczynska-Möller, W. Walczowski, and W.-J. von Appen, 2017: Evolution of the East Greenland Current from Fram Strait to Denmark Strait: Synoptic measurements from summer 2012. *Journal of Geophysical Research: Oceans*, **122**, 1974–1994, doi:10.1002/2017JC012961.

Ilicak, M., and Coauthors, 2016: An assessment of the Arctic Ocean in a suite of interannual CORE-II simulations. Part III: Hydrography and fluxes. *Ocean Modelling*, **100**, 141–161, doi:10.1016/j.ocemod.2016.02.004.

Johannessen, J. A., and Coauthors, 1987: Mesoscale Eddies in the Fram Strait Marginal Ice Zone During the 1983 and 1984 Marginal Ice Zone Experiments. *Journal of Geophysical Research: Oceans*, **92 (C7)**, 6754–6772, doi:10.1029/JC092iC07p06754.

Johannessen, O. M., 1987: Introduction: Summer Marginal Ice Zone Experiments During 1983 and 1984 in Fram Strait and the Greenland Sea. *Journal of Geophysical Research: Oceans*, **92 (C7)**, 6716–6718, doi:10.1029/JC092iC07p06716.

Johannessen, O. M., J. A. Johannessen, J. Morison, B. A. Farrelly, and E. Svendsen, 1983: Oceanographic Conditions in the Marginal Ice Zone North of Svalbard in Early Fall 1979 With an Emphasis on Mesoscale Processes. *Journal of Geophysical Research*, **88 (C5)**, 2755–2769, doi:10.1029/jc088ic05p02755.

Jones, E. P., 2001: Circulation in the Arctic Ocean. *Polar Research*, **20 (2)**, 139–146, doi:10.1111/j.1751-8369.2001.tb00049.x.

Kanzow, T., 2017: The Expeditions PS100 of the Research Vessel POLARSTERN to the Fram Strait in 2016. *Reports on Polar and Marine Research*, **705**, doi:10.2312/BzPM_0702_2016.

Kawasaki, T., and H. Hasumi, 2016: The inflow of Atlantic water at the Fram Strait and its interannual variability. *Journal of Geophysical Research: Oceans*, **121**, 502–519, doi:10.1002/jgrc.20224.

Koenig, Z., C. Provost, N. Sennéchael, G. Garric, and J.-C. Gascard, 2017a: The Yermak Pass Branch: A Major Pathway for the Atlantic Water North of Svalbard. *Journal of Geophysical Research: Oceans*, **122**, 9332–9349, doi: 10.1002/2017JC013271.

Koenig, Z., C. Provost, N. Villacieros-Robineau, N. Sennéchael, A. Meyer, J.-M. Lellouche, and G. Garric, 2017b: Atlantic waters inflow north of Svalbard: Insights from IAOOS observations and Mercator Ocean global operational system during N-ICE2015. *Journal of Geophysical Research: Oceans*, **122**, 1254–1273, doi:10.1002/2016JC012264.

Lilly, J. M., P. B. Rhines, F. Schott, K. Lavender, J. Lazier, U. Send, and E. D'Asaro, 2003: Observations of the Labrador Sea eddy field. *Progress in Oceanography*, **59**, 75–176, doi:10.1016/j.pocean.2003.08.013.

Losch, M., D. Sidorenko, and A. Beszczynska-Möller, 2005: FEMSECT: An inverse section model based on the finite element method. *Journal of Geophysical Research: Oceans*, **110**, doi:10.1029/2005JC002910.

Lozier, M. S., and Coauthors, 2019: A sea change in our view of overturning in the subpolar North Atlantic. *Science*, **363**, 516–521, doi:10.1126/science.aau6592.

Manley, T. O., 1995: Branching of Atlantic water within the Greenland-Spitsbergen Passage: An estimate of recirculation. *Journal of Geophysical Research: Oceans*, **100 (C10)**, 20 627–20 634, doi:10.1029/95JC01251.

Manley, T. O., R. H. Bourke, and K. L. Hunkins, 1992: Near-surface circulation over the Yermak Plateau in northern Fram Strait. *Journal of Marine Systems*, **3**, 107–125, doi:10.1016/0924-7963(92)90033-5.

Marnela, M., B. Rudels, M.-N. Houssais, A. Beszczynska-Möller, and P. B. Eriksson, 2013: Recirculation in the Fram Strait and transports of water in and north of the Fram Strait derived from CTD data. *Ocean Science*, **9 (3)**, 499–519, doi: 10.5194/os-9-499-2013.

Maslowski, W., D. Marble, W. Walczowski, U. Schauer, J. L. Clement, and A. J. Semtner, 2004: On climatological mass, heat, and salt transports through the Barents Sea and Fram Strait from a pan-Arctic coupled ice-ocean model simulation. *Journal of Geophysical Research*, **109**, doi:10.1029/2001JC001039.

Mauritzen, C., 1996: Production of dense overflow waters feeding the North Atlantic across the Greenland-Scotland Ridge. Part 1: Evidence for a revised circulation scheme. *Deep-Sea Research*, **43 (6)**, 769–806, doi:10.1016/0967-0637(96)00037-4.

Notz, D., and J. Stroeve, 2016: Observed Arctic sea-ice loss directly follows anthropogenic CO2 emission. *Science*, **354 (6313)**, 747–750, doi:10.1126/science.aag2345.

Onarheim, I. H., L. H. Smedsrud, R. B. Ingvaldsen, and F. Nilsen, 2014: Loss of sea ice during winter north of Svalbard. *Tellus A: Dynamic Meteorology and Oceanography*, **66 (1)**, doi:10.3402/tellusa.v66.23933.

Orvik, K. A., and P. Niiler, 2002: Major pathways of Atlantic water in the northern North Atlantic and Nordic Seas toward Arctic. *Geophysical Research Letters*, **29 (19)**, doi:10.1029/2002GL015002.

Padman, L., A. J. Plueddemann, R. D. Muench, and R. Pinkel, 1992: Diurnal tides Near the Yermak Plateau. *Journal of Geophysical Research*, **97 (C8)**, 12 639–12 652.

Paquette, R. G., R. H. Bourke, J. F. Newton, and W. F. Perdue, 1985: The East Greenland Polar Front in Autumn. *Journal of Geophysical Research*, **90 (C3)**, 4866–4882, doi:10.1029/jc090ic03p04866.

Perkin, R. G., and E. L. Lewis, 1984: Mixing in the West Spitsbergen Current. *Journal of Physical Oceanography*, **14**, 1315–1325.

Piechura, J., Beszczynska-Möller, and R. Osiński, 2001: Volume, heat and salt transport by the West Spitsbergen Current. *Polar Research*, **20 (2)**, 233–240, doi:10.1111/j.1751-8369.2001.tb00061.x.

Polyakov, I. V., and Coauthors, 2017: Greater role for Atlantic inflows on sea-ice loss in the Eurasian Basin of the Arctic Ocean. *Science*, **356**, 285–291, doi:10.1126/science.aai8204.

Quadfasel, D., J.-C. Gascard, and K.-P. Koltermann, 1987: Large-Scale Oceanography in Fram Strait During the 1984 Marginal Ice Zone Experiment. *Journal of Geophysical Research*, **92 (C7)**, 6719–6728, doi:10.1029/jc092ic07p06719.

Rahmstorf, S., J. E. Box, G. Feulner, M. E. Mann, A. Robinson, S. Rutherford, and E. J. Schaffernicht, 2015: Exceptional twentieth-century slowdown in Atlantic Ocean overturning circulation. *Nature Climate Change*, **5**, 475–480, doi:10.1038/nclimate2554.

Richter, M. E., W.-J. von Appen, and C. Wekerle, 2018: Does the East Greenland Current exist in the northern Fram Strait? *Ocean Science*, **14 (5)**, 1147–1165, doi:10.5194/os-14-1147-2018.

Rudels, B., 1986: The θ-S relations in the northern seas: Implications for the deep circulation. *Polar Research*, **4 (2)**, 133–159, doi:10.1111/j.1751-8369.1986.tb00527.x.

Rudels, B., 1987: On the mass balance of the Polar Ocean, with special emphasis on the Fram Strait. *Skrifter*, **188**.

Rudels, B., 2016: Arctic Ocean stability: The effects of local cooling, oceanic heat transport, freshwater input, and sea ice melt with special emphasis on the Nansen Basin. *Journal of Geophysical Research: Oceans*, **121**, 4450–4473, doi:10.1002/2015JC011421.

Rudels, B., G. Björk, J. Nilsson, P. Winsor, I. Lake, and C. Nohr, 2005: The interaction between waters from the Arctic Ocean and the Nordic Seas north of Fram Strait and along the East Greenland Current: Results from the Arctic Ocean-02 Oden expedition. *Journal of Marine Systems*, **55**, 1–30, doi:10.1016/j.jmarsys.2004.06.008.

Rudels, B., E. Fahrbach, J. Meincke, G. Budéus, and P. Eriksson, 2002: The East Greenland Current and its contribution to the Denmark Strait overflow. *ICES Journal of Marine Science*, **59**, 1133–1154, doi:10.1006/jmsc.2002.1284.

Rudels, B., H. J. Friedrich, and D. Quadfasel, 1999: The Arctic Circumpolar Boundary Current. *Deep-Sea Research Part II*, **46**, 1023–1062, doi:10.1016/S0967-0645(99)00015-6.

Rudels, B., and D. Quadfasel, 1991: Convection and deep water formation in the Arctic Ocean - Greenland Sea System. *Journal of Marine Systems*, **2**, 435–450, doi:10.1016/0924-7963(91)90045-V.

Schaffer, J., T. Kanzow, W.-J. von Appen, L. von Albedyll, J. E. Arndt, and D. H. Roberts, 2020: Bathymetry constrains ocean heat supply to Greenland's largest glacier tongue. *Nature Geoscience*, doi:10.1038/s41561-019-0529-x.

Schaffer, J., W.-J. von Appen, P. A. Dodd, C. Hofstede, C. Mayer, L. de Steur, and T. Kanzow, 2017: Warm water pathways toward Nioghalvfjerdsfjorden Glacier, Northeast Greenland. *Journal of Geophysical Research: Oceans*, **122**, 4004–4020, doi:10.1002/2017JC012961.

Schaffer, J., and Coauthors, 2019: An update to Greenland and Antarctic ice sheet topography, cavity geometry, and global bathymetry (RTopo-2.0.4). PANGAEA, doi:10.1594/PANGAEA.905295.

Schauer, U., E. Fahrbach, S. Osterhus, and G. Rohardt, 2004: Arctic warming through the Fram Strait: Oceanic heat transport from 3 years of measurements. *Journal of Geophysical Research: Oceans*, **109 (6)**, 1–14, doi:10.1029/2003JC001823.

Schlichtholz, P., and M. N. Houssais, 1999a: An inverse modeling study in Fram Strait. Part I: dynamics and circulation. *Deep-Sea Research Part II*, **46**, 1083–1135, doi:10.1016/S0967-0645(99)00018-1.

Schlichtholz, P., and M. N. Houssais, 1999b: An inverse modeling study in Fram Strait. Part II: water mass distribution and transports. *Deep-Sea Research Part II*, **46**, 1137–1168, doi:10.1016/S0967-0645(99)00017-X.

Screen, J. A., and I. Simmonds, 2010: The central role of diminishing sea ice in recent Arctic temperature amplification. *Nature*, **464**, 1334–1337, doi:10.1038/nature09051.

Serreze, M. C., and J. Stroeve, 2015: Arctic sea ice trends, variability and implications for seasonal ice forecasting. *Philosophical Transactions of the Royal Society A*, **373**, doi:10.1098/rsta.2014.0159.

Smedsrud, L. H., R. Ingvaldsen, J. E. Ø. Nilsen, and Ø. Skagseth, 2010: Heat in the Barents Sea: transport, storage, and surface fluxes. *Ocean Science*, **6**, 219–234, doi:10.5194/os-6-219-2010.

Smeed, D. A., and Coauthors, 2018: The North Atlantic Ocean Is in a State of Reduced Overturning. *Geophysical Research Letters*, **45**, 1527–1533, doi:10.1002/2017GL076350.

Smith, W. H., and P. Wessel, 1990: Gridding with continuous curvature splines in tension. *Geophysics*, **55 (3)**, 293–305, doi:10.1190/1.1442837.

Spreen, G., L. Kaleschke, and G. Heygster, 2008: Sea ice remote sensing using AMSR-E 89-GHz channels. *Journal of Geophysical Research: Oceans*, **113**, doi:10.1029/2005JC003384.

Stroeve, J. C., V. Kattsov, A. Barrett, M. Serreze, T. Pavlova, M. Holland, and W. N. Meier, 2012: Trends in Arctic sea ice extent from CMIP5, CMIP3 and observations. *Geophysical Research Letters*, **39**, doi:10.1029/2012GL052676.

Swift, J. H., K. Aagaard, and S. A. Malmberg, 1980: The contribution of the Denmark Strait overflow to the deep North Atlantic. *Deep-Sea Research*, **27A**, 29–42, doi:10.1016/0198-0149(80)90070-9.

Tanhua, T., K. A. Olsson, and E. Jeansson, 2005: Formation of Denmark Strait overflow water and its hydro-chemical composition. *Journal of Marine Systems*, **57**, 264–288, doi:10.1016/j.jmarsys.2005.05.003.

Teigen, S. H., F. Nilsen, R. Skogseth, B. Gjevik, and A. Beszczynska-Möller, 2010: Baroclinic instability in the West Spitsbergen Current. *Journal of Geophysical Research: Oceans*, **115**, 35–52, doi:10.1029/2011JC006974.

Teigen, S. H., F. Nilsen, R. Skogseth, B. Gjevik, and A. Beszczynska-Möller, 2011: Baroclinic instability in the West Spitsbergen Current. *Journal of Geophysical Research: Oceans*, **116 (C7)**, doi:10.1029/2011JC006974.

University of Bremen, 2015: Institute of Environmental Physics, University of Bremen: Daily AMSR-2 sea ice maps. URL https://seaice.uni-bremen.de/sea-ice-concentration-amsr-eamsr2/.

Våge, K., R. S. Pickart, M. A. Spall, G. W. Moore, H. Valdimarsson, D. J. Torres, S. Y. Erofeeva, and J. E. Ø. Nilsen, 2013: Revised circulation scheme north of the Denmark Strait. *Deep-Sea Research Part I*, **79**, 20–39, doi:10.1016/j.dsr.2013.05.007.

von Appen, W.-J., 2017: Report on Mooring Processing of PS99.2/PS100/PS101 Recoveries. URL https://epic.awi.de/id/eprint/43137/.

von Appen, W.-J., 2018: The Expedition PS114 of the Research Vessel POLARSTERN to the Fram Strait 2018. *Reports on Polar and Marine Research*, **723**, URL https://epic.awi.de/id/eprint/48386/.

von Appen, W.-J., 2019a: Physical oceanography and current meter data (including raw data) from FRAM moorings in the Fram Strait, 2016-2018. PANGAEA, doi:10.1594/PANGAEA.904565.

von Appen, W.-J., 2019b: Raw data including physical oceanography from mooring R1-1 recovered during POLARSTERN cruise PS114. PANGAEA, doi:10.1594/PANGAEA.904548.

von Appen, W.-J., 2019c: Raw data including physical oceanography from mooring R2-1 recovered during POLARSTERN cruise PS114. doi:10.1594/PANGAEA.904550.

von Appen, W.-J., 2019d: Raw data including physical oceanography from mooring R3-1 recovered during POLARSTERN cruise PS114. PANGAEA, doi:10.1594/PANGAEA.904551.

von Appen, W.-J., 2019e: Raw data including physical oceanography from mooring R4-1 recovered during POLARSTERN cruise PS114. PANGAEA, doi:10.1594/PANGAEA.904549.

von Appen, W.-J., 2019f: Raw data including physical oceanography from mooring R5-1 recovered during POLARSTERN cruise PS114. PANGAEA, doi:10.1594/PANGAEA.904552.

von Appen, W.-J., U. Schauer, T. Hattermann, and A. Beszczynska-Möller, 2016: Seasonal Cycle of Mesoscale Instability of the West Spitsbergen Current. *Journal of Physical Oceanography*, **46 (4)**, 1231–1254, doi:10.1175/jpo-d-15-0184.1.

von Appen, W.-J., U. Schauer, R. Somavilla, and E. Bauerfeind, 2015: Exchange of warming deep waters across Fram Strait. *Deep-Sea Research Part I*, **103**, 86–100, doi:10.1016/j.dsr.2015.06.003.

von Appen, W.-J., C. Wekerle, L. Hehemann, V. Schourup-Kristensen, C. Konrad, and M. H. Iversen, 2018: Observations of a Submesoscale Cyclonic Filament in the Marginal Ice Zone. *Geophysical Research Letters*, **45**, 6141–6149, doi:10.1029/2018GL077897.

Walczowski, W., A. Beszczynska-Möller, P. Wieczorek, M. Merchel, and A. Grynczel, 2017: Oceanographic observations in the Nordic Sea and Fram Strait in 2016 under the IO PAN long-term monitoring program AREX. *Oceanologia*, **59**, 187–194, doi:10.1016/j.oceano.2016.12.003.

Walczowski, W., J. Piechura, R. Osinski, and P. Wieczorek, 2005: The West Spitsbergen Current volume and heat transport from synoptic observations in summer. *Deep-Sea Research*, doi:10.1016/j.dsr.2005.03.009.

Wekerle, C., Q. Wang, W.-J. von Appen, S. Danilov, V. Schourup-Kristensen, and T. Jung, 2017: Eddy-Resolving Simulation of the Atlantic Water Circulation in the Fram Strait With Focus on the Seasonal Cycle. *Journal of Geophysical Research: Oceans*, **122 (11)**, 8385–8405, doi:10.1002/2017JC012974.

Woodgate, R. A., 2018: Increases in the Pacific inflow to the Arctic from 1990 to 2015, and insights into seasonal trends and driving mechanisms from year-round Bering Strait mooring data. *Progress in Oceanography*, **160**, 124–154, doi:10.1016/j.pocean.2017.12.007.

Woodgate, R. A., E. Fahrbach, and G. Rohardt, 1999: Structure and transports of the East Greenland Current at 75°N from moored current meters. *Journal of Geophysical Research: Oceans*, **104 (C8)**, 18 059–18 072, doi:10.1029/1999jc900146.

Zhao, M., M.-L. Timmermans, S. Cole, R. Krishfield, A. Proshutinsky, and J. Toole, 2014: Characterizing the eddy field in the Arctic Ocean halocline. *Journal of Geophysical Research: Oceans*, **119**, 8800–8817, doi:10.1002/2014JC010488.

Appendix A

Meta data of moorings and instruments

In the following, detailed information is given on where the moorings were located, to which depth they extended to, when exactly they were deployed and recovered, as well as under which station number.
All instruments on the moorings relevant to this thesis are listed with their serial number, their planned depth in the water column, plus the depth offset that was used to determine the instrument's depth, if it didn't record pressure.

Table A.1: Meta data of moorings R1-1, R2-1, R3-1, R4-1, and R5-1, including longitude, latitude, depth, date/time and station name of deployment and recovery.

Mooring	**Lon**	**Lat**	**Depth [m]**	**Deployment date/time**	**Deployment station**	**Recovery date/time**	**Recovery station**
R1-1	0.0007°E	78.1702°N	3013	09-Aug-2016 13:54	PS100/106-1	20-Jul-2018 05:39	PS114/023-2
R2-1	0.0015°E	78.8335°N	2596	27-Jul-2016 13:48	PS100/039-2	20-Jul-2018 13:15	PS114/025-1
R3-1	0.0005°W	79.5000°N	2778	29-Jul-2016 23:25	PS100/045-1	21-Jul-2018 07:01	PS114/029-2
R4-1	0.1698°E	80.1625°N	3034	29-Jul-2016 18:14	PS100/047-1	25-Jul-2018 12:49	PS114/040-2
R5-1	0.1205°W	80.8530°N	3140	31-Jul-2016 12:34	PS100/053-1	24-Jul-2018 09:55	PS114/036-1

Table A.2: Meta data of the instruments on R1-1, R2-1, R3-1, R4-1, and R5-1 that were used in this thesis, including the type of instrument, the serial number (SN), the target depth, and, if an instrument didn't record pressure, the serial number of the instrument whose pressure record was used + the depth offset between the instruments. If there is no serial number, the depth offset was added to the instrument's own pressure record.

Mooring	Type	SN	Target depth [m]	(SN) + Depth offset [m]
R1-1	SBE37	13973	49	
	SBE56	6363	77	13973 + 28
	SBE56	6364	127	13973 + 78
	QMADCP	24069	228	
	SBE37	13974	231	
	SBE56	6365	330	13974 + 99
	SBE56	6366	480	13973 + 249
	AQD	12685	728	+ 28
	SBE37	13985	729	
R2-1	SBE37	13979	41	
	SBE56	6367	90	13979 + 49
	SBE56	6368	138	13979 + 97
	QMADCP	23806	242	+ 2
	SBE37	13980	244	
	SBE56	6369	344	13980 + 100
	SBE56	6370	494	13980 + 250
	AQD	12718	742	+ 18
	SBE37	13981	743	
R3-1	SBE37	13982	49	
	SBE56	6371	107	13982 + 58
	SBE56	6372	156	13982 + 107
	QMADCP	24673	260	
	SBE37	13986	268	
	SBE56	6394	367	13986 + 99
	SBE56	6395	517	13986 + 249
	AQD	12745	765	+ 15
	SBE37	13984	766	
R4-1	SBE37	13978	43	
	SBE56	6396	82	13978 + 39
	SBE56	6397	130	13978 + 87
	QMADCP	23976	232	- 1
	SBE37	13907	235	
	SBE56	6398	334	23976 + 102
	SBE56	6399	484	13973 + 252
	AQD	12680	732	+ 22
	SBE37	13987	733	
R5-1	SBE37	14015	49	
	SBE56	6400	97	14015 + 48
	SBE56	6401	177	14015 + 128
	QMADCP	24071	248	+ 3
	SBE37	14005	251	
	SBE56	6402	350	14005 + 99
	SBE56	6403	500	14005 + 249
	AQD	12667	748	+ 15
	SBE37	14006	749	

Appendix B

Extension of data set

We attempted to extend the salinity dataset in the vertical by calculating salinity values from temperature measurements of the temperature loggers. We explain the attempted procedure here and argue, why we did not end up using the resulting calculated salinity data. The relationship between temperature and salinity is determined by a linear regression of both the measurements of the CTDs at $\sim$ 265 m and $\sim$ 760 m, assuming the decrease in temperature between the two depths is related to a similar decrease in salinity.
However, in this case the residuals of the linear regression are only randomly distributed at R1-1 and R2-1 (not shown). This may in part be due to the missing data at R3-1 and R4-1, leading to the regression being skewed, which could be avoided by only using the part of the time series, where there is data available at both depths. It may also be due to the fact that at the moorings further north, the PW layer sometimes reaches below 265 m so that the CTD at $\sim$ 265 m depth is located in a salinity-stratified regime rather than a temperature-stratified one, making it much more difficult to assess without actual salinity measurements, what the transition of salinity looks like between the two CTDs. This may not always be the case and one possible solution could be to somehow differentiate between time periods of different stratification regimes, only using the times where the stratification is determined by temperature for the linear regression. Another solution may be to visually fit a regression line to the data in order to accommodate for a better T-S relationship related to a temperature-stratified regime. Of course, this assumes that temperature is more important for stratification between the two CTDs, which may not be true for the entirety of this part of the water column. While it seems to be a good assumption for R1-1 and R2-1, analysis of potential density and buyoancy frequency reveals that inferring salinity data from the temperature logger measurements causes significant instability in the water column, in particular at R1-1, which is why we choose not to use any of the inferred salinity data.

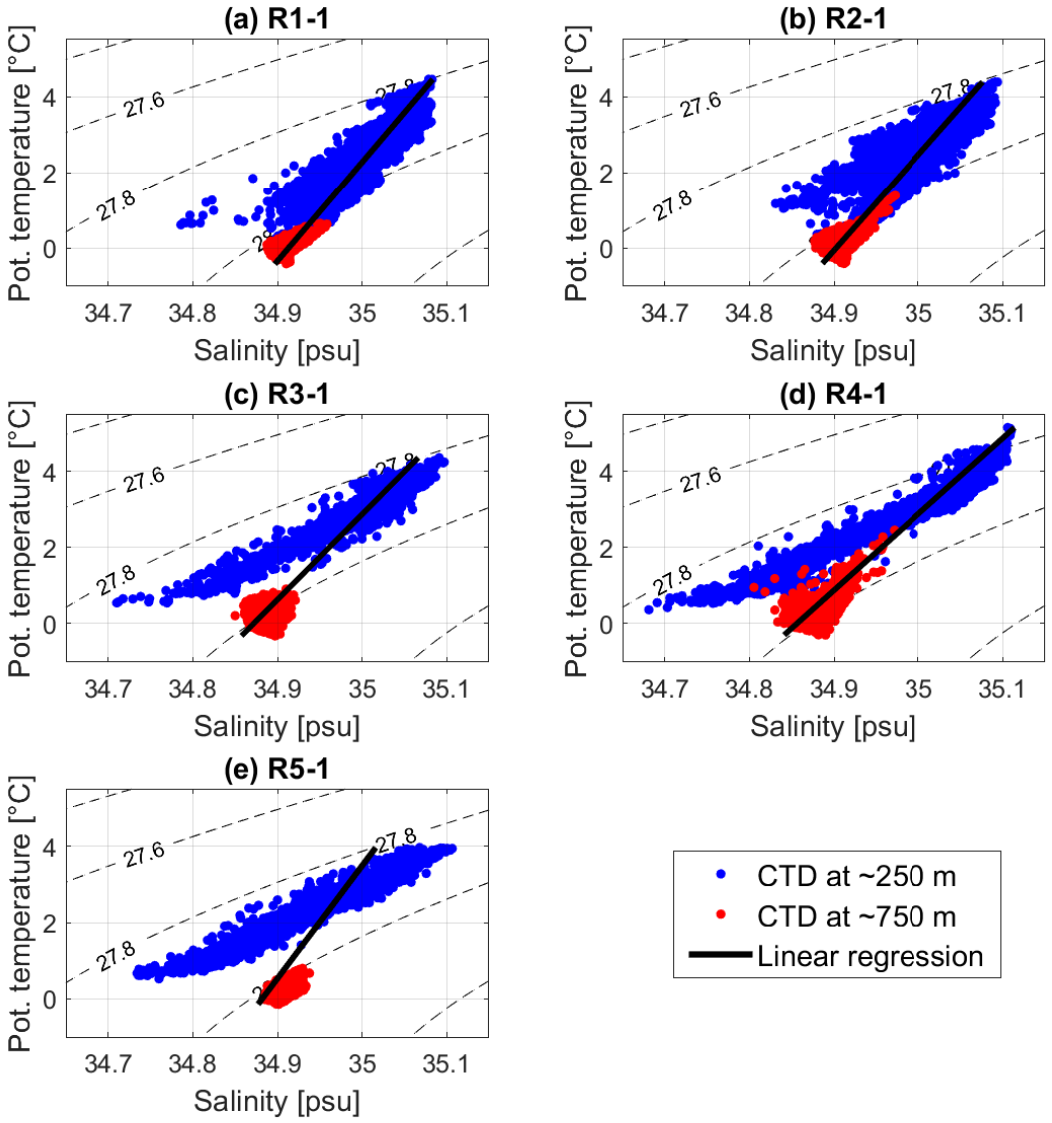

Figure B.1: ΘS plot with linear regression (black line) of potential temperature [°C] and salinity [psu] of the CTD measurements at ∼ 250 m (blue dots) and ∼ 750 m (red dots) depth at (a) R1-1, (b) R2-1, (c) R3-1, (d) R4-1, and (e) R5-1.

Appendix C

Seasonal cycle of standard deviation

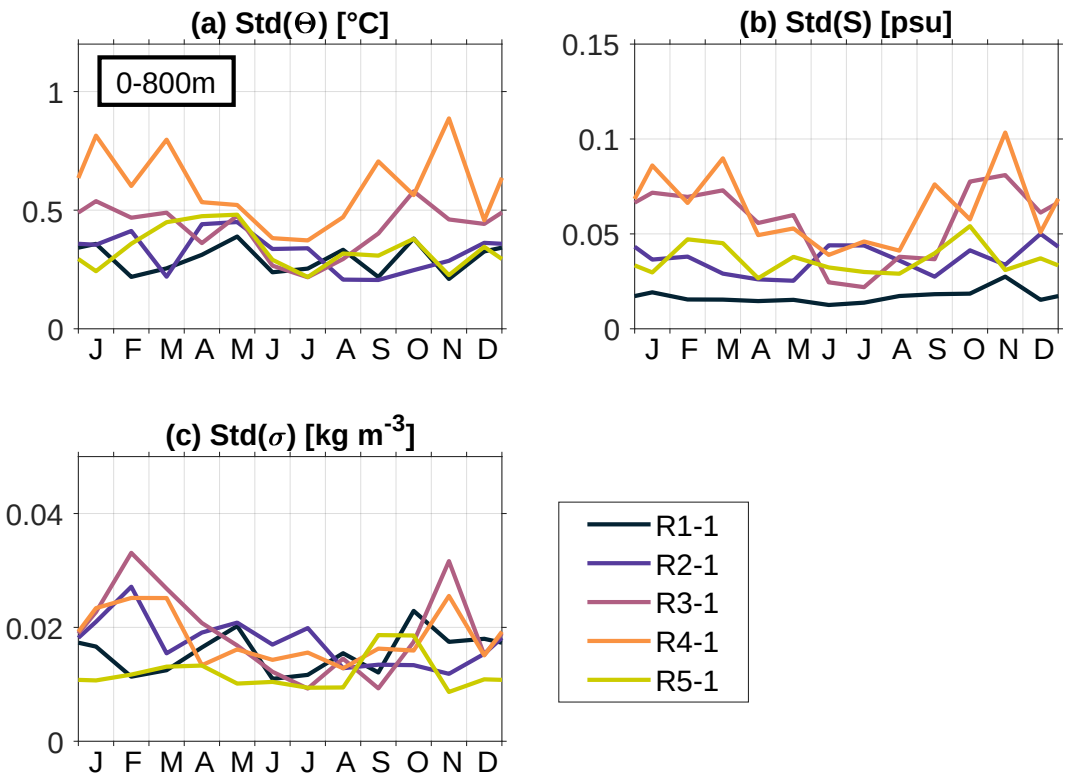

Figure C.1: Seasonal cycle of standard deviation of (a) potential temperature (°), (b) salinity (psu), and (c) potential density (kg m^{-3}) from all gridded measurements at R1-1 (dark blue), R2-1 (violet), R3-1 (dark pink), R4-1 (orange), and R5-1 (green). Note that there are no data available in the upper 40 m for potential temperature, salinity, and potential density, and in the upper 20 m for eddy kinetic energy, zonal and meridional velocity.

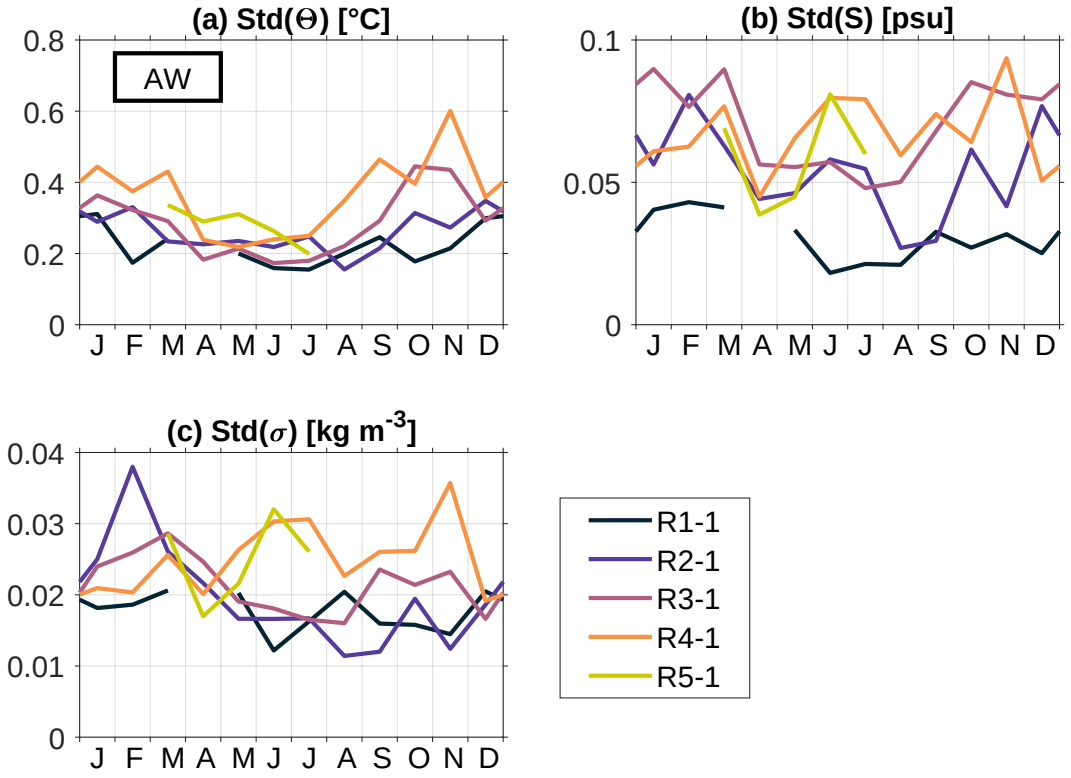

Figure C.2: Same as Figure C.1, but only for gridded measurements that fit the AW definition. Note that axis limits for the standard deviation of potential temperature, salinity, and potential density are different to the ones in Figure C.1. In months, during which less than 10% of the gridded measurements fall into the definition of AW, no monthly standard deviation is calculated.

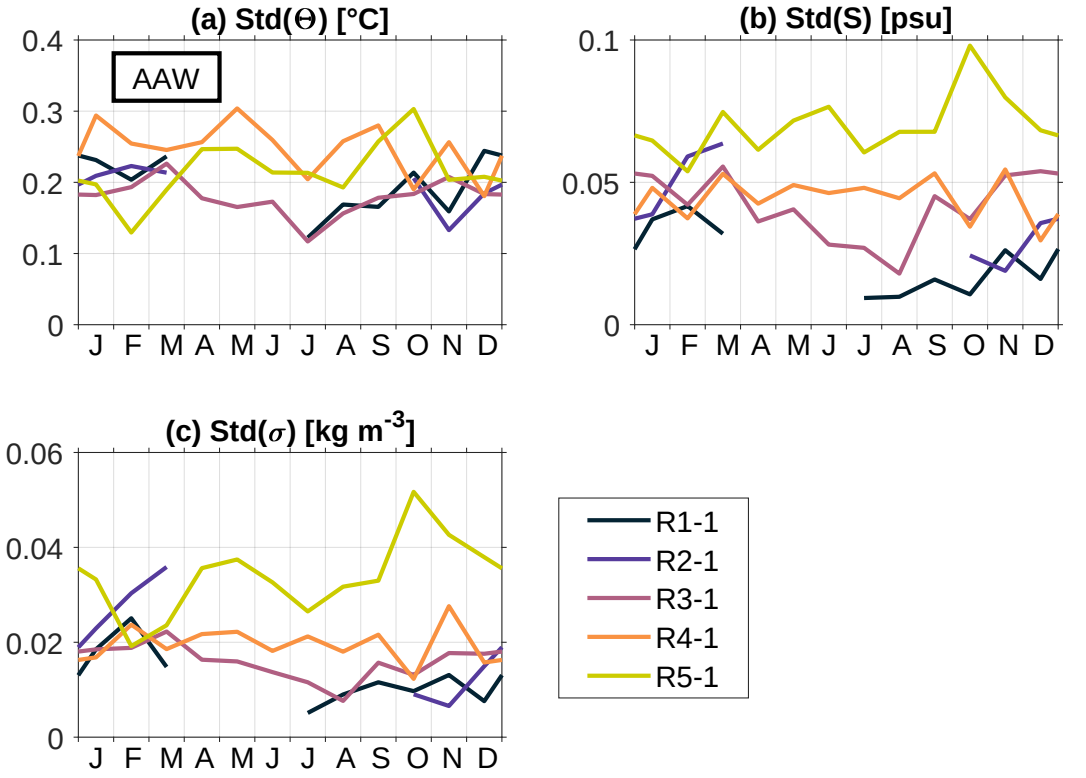

Figure C.3: Same as Figure C.1, but only for gridded measurements that fit the AAW definition. Note that axis limits for the standard deviation of potential temperature, salinity, and potential density are different to the ones in Figure C.1. In months, during which less than 10% of the gridded measurements fall into the definition of AAW, no monthly standard deviation is calculated.

Erklärung

Hiermit erkläre ich, dass ich die vorliegende Arbeit selbständig und ohne fremde Hilfe angefertigt und keine anderen als die angegebenen Quellen und Hilfsmittel verwendet habe. Die eingereichte schriftliche Fassung der Arbeit entspricht der auf dem elektronischen Speichermedium.

(Name der Datei: Hofmann_1010110.pdf)

Weiterhin versichere ich, dass diese Arbeit noch nicht als Abschlussarbeit an anderer Stelle vorgelegen hat.

24.02.2020, Zerlina Hofmann